Dipl.-Ing. Harald Brandstätter

Aspects of Ionic Transport in Materials for Lithium-Ion Batteries

DISSERTATION

zur Erlangung des akademischen Grades

Doktor der technischen Wissenschaften

eingereicht an der

Technischen Universität Graz

Betreuer

Univ.-Prof. Dipl.-Chem. Dr. rer. nat. Martin Wilkening

Institut für Chemische Technologie von Materialien

Graz, Juli 2016

EIDESSTATTLICHE ERKLÄRUNG

Ich erkläre an Eides statt, dass ich die vorliegende Arbeit selbstständig verfasst, andere als die angegebenen Quellen/Hilfsmittel nicht benutzt, und die den benutzten Quellen wörtlich und inhaltlich entnommenen Stellen als solche kenntlich gemacht habe. Das in TUGRAZonline hochgeladene Textdokument ist mit der vorliegenden Dissertation identisch.

Datum

Unterschrift

Abstract

The main limiting factor in electrification of road transport is the insufficient storage capacity of current batteries. The importance of developing better batteries for road transportation has been emphasised over the past few years.

Here, the field of materials science plays a major part in the research for new and better solid ion conductors as components in future battery systems with regard to performance and safety. It does not only supply the much-needed materials, it also provides a wide range of methods for their thorough characterisation.

The present work approaches this problem from the perspective of two such methods: Electrochemical impedance spectroscopy (EIS) and X-ray diffraction (XRD) are used to characterise Li-ion conductors and electrodes, providing a means to identify potential candidates to be used as solid electrolytes, liquid electrolytes and electrode materials in safe and high-performing batteries. The results are presented cumulatively in the form of published and peer-reviewed papers and unpublished manuscripts.

The monoclinic polymorph of Li_2TiO_3 (β-form) is known to be a relatively poor Li-ion conductor. Up to now, there is no information available on how the ion transport properties change when going from well-ordered crystalline Li_2TiO_3 to a structurally disordered form with the same chemical composition. Here, high-energy ball milling is used to prepare nanocrystalline, defect-rich Li_2TiO_3. It turns out that ball milling offers the possibility to enhance long-range ion transport in the oxide by approximately 3 orders of magnitude. Structural disorder in nanocrystalline as well as amorphous Li_2TiO_3 is found to play the capital role in governing Li-ion dynamics of the sample finally obtained.

One of the best solid Li-ion conductors known is Li_3PS_4. Up to now, it has not been investigated on *short-range* ion conducting paths. The pure crystalline γ-phase is synthesised by ball milling followed by heat treatment. It turns out that the γ-Li_3PS_4 synthesised within this work pertains the highest *long-range* conductivity ever observed. The NMR experiments show fast local jump movements that do not necessarily cause high conductivities and low activation energies of the ionic transport on longer time scales.

The present study on Li-ion half cells with the liquid electrolyte *lithiumhexafluorophosphate* ($LiPF_6$) is aimed at answering the question whether solid electrolyte interphase (SEI) formation or other origins such as cell design ought to be considered as sources for inductive loop formation. Four different sources of (i) *inductive* and (ii) *negative capacitance* loop formation are identified: springs, reference electrodes, drift and corrosion. In conclusion, any interrelationship between inductive loops and SEI formation can be ruled out. This finding disproves an earlier, commonly known attempt that traced the presence of inductive loops back to the formation of passivating surface layers because of electrolyte decomposition.

Si-based negative-electrode materials could significantly increase the energy density of commercial lithium-ion batteries. Compared to conventional Li-ion battery materials, Si has the largest theoretical gravimetric capacity. The findings show that the ionic mobility is very restricted at low temperatures which leads to a very high internal resistance of the microcell. However, the cell does not suffer significantly from heating and cooling. Thus, cell damage due to thermal volume expansion can be excluded.

Keywords: impedance spectroscopy, nuclear magnetic resonance, lithium diffusion, solid electrolytes, nano-structured materials, solid electrolyte interphase, silicon

Contents

1 Introduction

The electrification of road transport is a societal goal of utmost importance. There are several key factors driving this change: (i) a move to shift away from oil, which has often been a major source of political instability, (ii) an effort to curb CO_2 emissions, one third of which originates from vehicular transportation and (iii) an attempt to improve air quality, especially in densely populated cities. Air quality concerns in major cities around the world are so alarming that it has led to a major push in emerging economies towards electric vehicle adoption in an effort to improve purity of breathable air and curb levels of particulate matter, especially the PM_{10} and $PM_{2.5}$ levels.

The major hurdle for widespread adoption of electric vehicles (EVs) was highlighted in a quote in the Washington Post, "*Prices on electric cars will continue to drop until they're within reach of the average family*". This quote was actually featured in the newspaper in 1915, and a century later, we are still facing the same issue. The main culprit here is the insufficient storage capacity of current batteries, severely limiting the range of practical EVs. The importance of developing better batteries for road transportation has been emphasised over the past few years, with several leading research programs emerging in the last 5 years. [1]

In comparison to other technologies, which are discussed for automotive applications such as nickel-metal hydride, nickel-cadmium, lead-acid, or supercapacitors, the major advantage of the Li-ion technology is the higher energy density with reasonable power density. Only supercapacitors can deliver higher power densities but they offer a short range due to limited energy density. Considering the combined lifetime performance of cycling and calendar ageing, the Li-ion technology outplays the other technologies. [2]

Modern Li-ion batteries hold more than twice as much energy by mass as the first commercial versions sold by Sony in 1991 - and are ten times cheaper. But they are close to their development limit. [3] The two key aspects to consider in this regard are (i) performance and (ii) safety. [4–6]

Most researchers think that improvements to Li-ion cells can squeeze in, at most, 30 % more energy by mass. That means that Li-ion cells will never give electric cars the 800-kilometre range of a petrol tank, or supply power-hungry smartphones with many days of operation. [3]

One strategy of enhancing the security is to find alternatives to carbon based materials with good safety and cycling stability. Ti-based oxides such as $Li_4Ti_5O_{12}$ have been considered as potential alternative materials to traditional carbon-based anodes, since they exhibit excellent Li-ion insertion/extraction reversibility with small structural change and a much higher operating voltage ranging from 3 to 1 V (vs. Li/Li^+) ensuring a better safety of the battery by avoiding the problem of lithium dendrites. [7–9]

The second strategy of enhancing the safety is the development of all-solid-state lithium-ion batteries based on solid electrolytes. They have attracted attention in recent years due to increased concerns on the safety problems of commercial lithium-ion batteries employing liquid electrolyte. [10–12]

As for the performance improvement, this relies ether on the research on new energy materials, or on the improvement of already known ones. Here, the last point is not to be underrated, as it can be as effective as the synthesis of wholly new materials. Particularly, the introduction of structural disorder as well as different kinds of interfaces *via* high-energy ball milling can lead to a dramatic enhancement of the transport properties of a given compound. [13–16] In this regard, layer-structured materials into which Li can be reversibly inserted are not only interesting as electrode materials in rechargeable batteries. Considering the relative scarcity of experimental studies from an atomic-scale point of view, many examples can be found also showing enhanced transport properties in such compounds.[17–23]

A powerful method of characterising transport properties of materials and their interfaces with electronically conducting electrodes in electrochemical systems is *electrochemical impedance spectroscopy* (EIS). It may be used to investigate the dynamics of bound or mobile charge in the bulk or interfacial regions of any kind of solid or liquid material: ionic, semiconducting, mixed electronic–ionic, and even insulators (dielectrics). [24]

The atomic and molecular structure of solids is identified *via X-ray crystallography* (XRD). X-rays with wavelengths in the dimension of the crystal are interacting with the electrons of the crystalline atoms and cause a beam of incident X-rays to diffract into many specific directions. By measuring the angles and intensities of these diffracted beams, a three-dimensional picture of the density of electrons within the crystal can be produced. From this electron density, the mean positions of the atoms in the crystal can be determined, as well as their chemical bonds, their disorder and various other information. [25]

This dissertation will begin with an introductory theoretical chapter, where the reader is familiarised with the concept of ionic transport in electrolytes (Sec. 2). It is followed by a brief overview of the techniques used to acquire the data presented here in Sec. 3 (EIS) and 4 (XRD). In chapter 5 the results obtained in the course of this dissertation will be presented cumulatively in the form of published (and peer-reviewed) papers and unpublished manuscripts. This thesis will conclude with a short summary and an outlook on possible future work. Additionally, in the appendices the experimental information will be found.

2 Ionic Transport in Electrolytes

2.1 Introduction

Mass transport to or from an electrode can, in absence of fluid turbulence,[26] occur by three processes:[27] (i) *advection* as the movement of some quantity via the bulk flow of a fluid,[28] (ii) *electrical migration* in an electric potential gradient, and (iii) *diffusion* in a concentration gradient. The first of these processes can be handled mathematically with the advection equation. In Cartesian coordinates the advection operator is

$$\boldsymbol{u} \cdot \nabla = u_x \frac{\partial}{\partial x} + u_y \frac{\partial}{\partial y} + u_z \frac{\partial}{\partial z}\,, \tag{2.1}$$

where $\boldsymbol{u} = (u_x, u_y, u_z)$ is the velocity field, and ∇ is the nabla operator.
The second process was described mathematically by Nernst [29,30] and Planck [31]:

$$\boldsymbol{j} = cU\nabla\phi\,, \tag{2.2}$$

with the flux $\boldsymbol{j}$, the mobility U and the electric potential ϕ.

The third process, diffusion in a concentration gradient, is the most important of the three processes and is the one which typically is dominant in mass transport in batteries. In the continuum approach, the analysis of diffusion uses the basic equation due to Fick [32] which defines the flux of material crossing a plane at distance x and time t. The flux $\boldsymbol{j}$ is proportional to the concentration gradient ∇c and is in the simplest case represented by the expression:

$$\boldsymbol{j} = -D\nabla c\,. \tag{2.3}$$

The minus sign signifies the fact that a concentration gradient will always result in a particle flux leading to the equalisation of the concentration. The constant of proportionality D is the *diffusion coefficient* (also known as the *diffusivity*). Only in an isotropic medium the diffusion coefficient in Eq. (2.3) is a constant. This is a special case; generally, D is dependent on the direction of the concentration gradient and denoted by a tensor $\hat{\boldsymbol{D}}$.

The three transport phenomena can be joint in a single equation:

$$\boldsymbol{j} = cU\nabla\phi - D\nabla c + \boldsymbol{u}c\,. \tag{2.4}$$

For application directly to battery technology, the three modes of mass transport have meaningful significance. Convective and stirring processes can be employed to provide a flow of electroactive species to reaction sites. Examples of the utilisation of stirring and flow processes in batteries are the circulating zinc/air system, the vibrating zinc electrode, and the zinc-chlorine hydrate battery. In some types of large lead-acid batteries, circulation of acid is provided to improve utilisation of the active materials in the battery plates. Migration effects are in some cases detrimental to battery performance, in particular those caused by enhanced electric fields (potential gradients) around sites of convex curvature. Increased migration at these sites tends to produce dendrite formations which eventually lead to a short-circuit and battery failure.

2.2 Ionic Transport in Liquids and Gels

Following Nyman,[33] for electrolytes in batteries, a steady state can be assumed, that is the absence of velocity gradients. In this case, only diffusion and migration are taken into account and advection is neglected. We are dealing with a multicomponent system. A deviation from equilibrium between the molecular friction and thermodynamic interactions leads to the diffusion flux.[34] The equations that describe transport processes in multicomponent systems have been developed independently and in parallel by James Clerk Maxwell[35] for dilute gases and Josef Stefan[36] for fluids. The Maxwell-Stefan equation is:[37]

$$\frac{\nabla \mu_i}{R\,T} = \nabla \ln a_i \quad = \sum_{\substack{j=1 \\ j \neq i}}^{n} \frac{\chi_i \chi_j}{D_{ij}} (\boldsymbol{v}_j - \boldsymbol{v}_i) = \sum_{\substack{j=1 \\ j \neq i}}^{n} \frac{c_i c_j}{c^2 D_{ij}} \left(\frac{\boldsymbol{J}_j}{c_j} - \frac{\boldsymbol{J}_i}{c_i} \right), \tag{2.5}$$

with the nabla operator ∇, mole fraction χ, chemical potential μ, activity a, indexes for component i and j, number of components n, Maxwell-Stefan-diffusion coefficient D_{ij}, diffusion velocity of component i $\boldsymbol{v}_i$, molar concentration of component i c_i, total molar concentration c, flux of component i $\boldsymbol{J}_i$.

For complex systems, such as electrolytic solutions, and other drivers, such as a pressure gradient, the equation must be expanded to include additional terms for interactions. Furthermore, the diffusion coefficients, with the exception of the diffusion of dilute gases, do not correspond to the Fick's diffusion coefficients and are therefore not tabulated. Nyman[33] used the Maxwell-Stefan equation in his thesis as basis for the characterisation, formulated models of the transport from the equation and identified the apparent transport properties for liquid and gel electrolytes.

2.3 Ionic Transport in Solids

In a solid, due to the low drift velocity of ions, the effects of advection can be neglected. The significant transport phenomena are migration and diffusion. Following Mehrer,[38] a solid

can be treated as an isotropic medium. Thus, the diffusion coefficient is a constant and the continuum model based on Fick's law [32] remains valid. Cancelling advection out of Eq. (2.4)

$$\boldsymbol{j} = cU\nabla\phi - D\nabla c + \boldsymbol{\mu c}\,, \tag{2.6}$$

leads to a differential equation for three-dimensional migration and diffusion in solids:

$$\boldsymbol{j} = cU\nabla\phi - D\nabla c\,. \tag{2.7}$$

Until now (2016), Eq. (2.7) has not been solved analytically; the approaches in the literature only consider diffusion and advection under certain boundary conditions. [38–40]

2.3.1 Mechanism of One-Dimensional Ion Transfer

An electrode reaction proceeding at a finite rate involves movement of reacting materials between the electrode and the solution surrounding it. Following Tobias, [26] this reaction can be approximated as one-dimensional process. Eq. 2.7 can be simplified to express the rate of transfer for a given species in the x direction per unit area perpendicular to x at any point in the fluid:

$$N_\mathrm{t} = cU\frac{\partial\phi}{\partial x} - D\frac{\partial c}{\partial x} + Vc\,, \tag{2.8}$$

where N_t denotes the total rate of transfer, c the concentration of the given species, U the mobility, ϕ the electric potential, x the distance in direction of transfer, D the diffusion coefficient, and V the velocity of bulk fluid movement in direction of transfer.

The Nernst–Planck equation (2.8) is a conservation of mass equation used to describe the motion of a charged chemical species in a fluid medium. It describes the flux of ions under the influence of both an ionic concentration gradient and an electric field. For unsteady state processes, changes of concentration with time must be considered. [26] Applying the law of conservation

$$\frac{\partial\rho}{\partial t} + \operatorname{div}\boldsymbol{j} = 0\,, \tag{2.9}$$

with the mass density ρ and the flow density $\boldsymbol{j}$ the general transfer equation (2.8) becomes:

$$\frac{\partial c}{\partial t} = -\operatorname{div}(Uc\operatorname{grad}\phi) + \operatorname{div}(D\operatorname{grad}c) - \boldsymbol{V}\operatorname{grad}c\,, \tag{2.10}$$

where t is the time. While Tobias[26] is presenting a discrete layer-model for liquid fluids, we are pursuing a continuous solid-electrolyte-model. In advection, a fluid transports some conserved quantity or material via bulk motion. The fluid's motion is described mathematically as a vector field, and the transported material is described by a scalar field showing its distribution over space. Advection requires currents in the fluid, and so cannot happen in rigid solids. It does not include transport of substances by molecular diffusion, so the effect of advection can be neglected:

$$\frac{\partial c}{\partial t} = -\mathrm{div}(Uc\,\mathrm{grad}\,\phi) + \mathrm{div}(D\,\mathrm{grad}\,c) \cancel{-\boldsymbol{V}\mathrm{grad}\,c}\,. \tag{2.11}$$

Assuming a one-dimensional flow in x-direction we can set

$$\mathrm{grad} = \mathrm{div} = \frac{\partial}{\partial x} \tag{2.12}$$

and calculate

$$\mathrm{grad}\phi = \boldsymbol{E} = E\,, \tag{2.13}$$

with E the electric field in flow-direction x. It is the driving force for migration. At this stage, we assume the electric field constant and uniform between the two electrodes. We will return to this restriction in section 2.3.4. Furthermore, we are dealing with only one type of ions, no mixture between positive and negative charge is allowed. Since we are neglecting its time-dependence, E can be treated as a constant and our differential equation remains linear. This assumption allows us to simplify (2.11) further to

$$\frac{\partial c}{\partial t} = -UE\frac{\partial c}{\partial x} + D\frac{\partial^2 c}{\partial x^2}\,. \tag{2.14}$$

This is a second order homogeneous parabolic partial differential equation. In his book[40] first published in 1956, Crank delivers mathematical models for describing diffusion only, but in the present case migration has to be taken into account as well.

2.3.2 Analytical Solution of the One-Dimensional Nernst-Planck-Equation

The last simplification step to equation (2.14) makes the variables separable. The partial differential equation may be transformed to an ordinary differential equation:

$$c(x,t) = A(x)B(t)\,. \tag{2.15}$$

Inserting (2.15) into (2.14) and dividing by (2.15) leads to

$$A(x)\dot{B}(t) = -UEA'(x)B(t) + DA''(x)B(t) \,|:(A(x)B(t)) \tag{2.16}$$

$$\frac{\dot{B}(t)}{B(t)} = -UE\frac{A'(x)}{A(x)} + D\frac{A''(x)}{A(x)} \equiv K\,, \tag{2.17}$$

with dot denoting derivative with respect to time and apostrophe to space. As both sides of the equation must be the same for all values of t and x, they must be equivalent to the so-called *separation constant* K. We can now rewrite (2.16) to:

$$DA''(x) - UEA'(x) - KA(x) = 0 \tag{2.18}$$

$$\dot{B}(t) - KB(t) = 0\,. \tag{2.19}$$

These are ordinary, homogeneous, linear differential equations with constant coefficients. To find a general solution, we substitute $A(x)$, $B(x)$ and its derivatives with the following base functions:

$$A = e^{\lambda x}\,,\ A' = \lambda e^{\lambda x}\,, A'' = \lambda^2 e^{\lambda x}\,,\ B = e^{\lambda t}\,,\ \dot{B} = \lambda e^{\lambda t}\,. \tag{2.20}$$

The characteristic equation for $A(x)$ is:

$$D\lambda^2 - UE\lambda - K = 0\,. \tag{2.21}$$

It is a square equation with 2 real roots:

$${}_1\lambda_2 = \frac{1}{2D}\left(UE \pm \sqrt{(-UE)^2 + 4DK}\right)\,, \tag{2.22}$$

thus the solution for $A(x)$ is a linear combination:

$$A(x) = e^{\lambda_1 x} + e^{\lambda_2 x}\,. \tag{2.23}$$

The characteristic equation for $B(t)$ is:

$$\lambda_3 = K\,, \tag{2.24}$$

which leads to

$$B = e^{\lambda_3 t} = e^{Kt}\,. \tag{2.25}$$

Putting (2.15), (2.22), (2.23) and (2.25) together gives the following equation for $c(x,t)$:

$$c(x,t) = \left[e^{\frac{1}{2D}\left(UE+\sqrt{(-UE)^2+4DK}\right)x} + e^{\frac{1}{2D}\left(UE-\sqrt{(-UE)^2+4DK}\right)x} \right] e^{Kt}\,, \tag{2.26}$$

where the separation constant K is still unknown.

2.3.3 Boundary Conditions

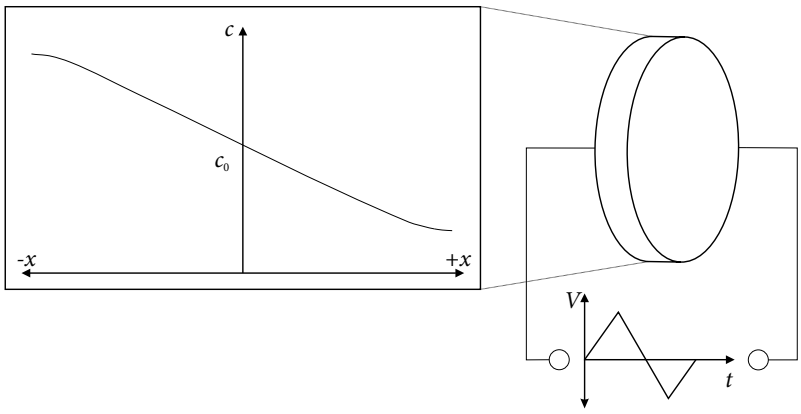

Figure 2.1: Expected concentration profile in a polarised solid sample. c denotes the concentration of the given species, c_0 the initial concentration, x the one-dimensional space coordinate, V the externally applied voltage and t the time.

As seen in figure 2.1, we are moving the origin of our space-coordinate x to the centre of our pellet. We assume the concentration c to remain constant in this point. This lets us define a Dirichlet boundary condition:

$$c(0,t) = c_0\,, \tag{2.27}$$

which is the initial concentration of the material, a given material constant. Inserting (2.27) into (2.26) gives:

$$\left[e^0 + e^0\right] e^{Kt} = c_0 \tag{2.28}$$

$$2e^{Kt} = c_0 \tag{2.29}$$

$$K = \frac{\ln\left(\frac{c_0}{2}\right)}{t}\,. \tag{2.30}$$

Inserting (2.28) into (2.26) gives the final solution for $c(x,t)$:

$$c(x,t) = \left[e^{\frac{1}{2D}\left(UE+\sqrt{(-UE)^2+4D\frac{\ln\left(\frac{c_0}{2}\right)}{t}}\right)x} + e^{\frac{1}{2D}\left(UE-\sqrt{(-UE)^2+4D\frac{\ln\left(\frac{c_0}{2}\right)}{t}}\right)x} \right] \frac{c_0}{2}\,. \tag{2.31}$$

2.3.4 Concentration Polarisation

In equation (2.31) the electric field is assumed as constant, as mentioned in section 2.3.1. To take into account the effects of concentration polarisation, we use one of Maxwell's equations to calculate the electric field E from a given charge carrier density ρ:

$$\nabla \cdot \boldsymbol{E} = \frac{\rho}{\varepsilon_\mathrm{r} \cdot \varepsilon_0}\,, \tag{2.32}$$

which is the so-called Gauss's law, with the relative (r) and vacuum (0) permittivities ε. By integration we receive an equation for the electric field in x-direction:

$$E_x = \frac{1}{\varepsilon_\mathrm{r} \cdot \varepsilon_0} \int_0^x \rho dx\,. \tag{2.33}$$

Replacing ρ with c and inserting (2.31) into (2.33), the electric field caused by concentration polarisation E_cp is

$$E_\mathrm{cp}(x,t) = \frac{1}{\varepsilon_\mathrm{r} \cdot \varepsilon_0} \left[\frac{e^{\frac{1}{2D}\left(UE+\sqrt{(-UE)^2+4D\frac{\ln\left(\frac{c_0}{2}\right)}{t}}\right)x}}{\frac{1}{2D}\left(UE+\sqrt{(-UE)^2+4D\frac{\ln\left(\frac{c_0}{2}\right)}{t}}\right)} + \frac{e^{\frac{1}{2D}\left(UE-\sqrt{(-UE)^2+4D\frac{\ln\left(\frac{c_0}{2}\right)}{t}}\right)x}}{\frac{1}{2D}\left(UE-\sqrt{(-UE)^2+4D\frac{\ln\left(\frac{c_0}{2}\right)}{t}}\right)} \right] \frac{c_0}{2}\,. \tag{2.34}$$

While Greeuw[41] completely ignores concentration polarisation, with equations (2.31) and (2.34), the problem can be solved iteratively.

2.3.5 Further Considerations

To get rid of one constant and add temperature dependency, charge carrier mobility U can be expressed by Einstein's relation:[42]

$$U = \frac{D}{kT}, \tag{2.35}$$

with the diffusion coefficient D, the thermodynamic temperature T and Boltzmann's constant k.

2.4 Diffusion and Defects

In a perfect crystal all atoms would be on their correct lattice positions in the structure. This situation can only exist at the absolute zero of temperature, 0 K.[43] Above 0 K, defects occur in the structure. They fall into two main categories: (i) *intrinsic* defects which are integral to the crystal in question, and (ii) *extrinsic* defects which are created when a foreign atom is inserted into the lattice.

The defects of the first category can have zero to three dimensions;[43] the most significant are zero-dimensional or *point defects*. They fall under two categories: Schottky defects, which consist of vacancies in the lattice and Frenkel defects where a vacancy is created by an atom or ion moving into an interstitial position. Both are thermally activated.[38,44,45] Since point defects are able to move through the crystal they often play a key role in the mediation of atomic diffusion. Frenkel disorder describes a defect pair where an atom occupying a regular site on the crystal lattice is moved to an interstitial site forming an interstitial and leaving behind a vacancy on the regular site. In ionic crystals, Schottky disorder applies to a situation in which vacancies are formed on both the anion and the cation sub-lattice in stoichiometric amounts so as to preserve charge neutrality. If cation sites are occupied by anions (and *vice versa*) this is known as *anti-site defects*. Obviously, if the number of such sites on both sub-lattices is not equal then the stoichiometry of the compound will shift.[45]

Extrinsic defects may be homovalent or heterovalent and occupy interstitial or regular lattice sites. In the case of heterovalent doping, charge neutrality dictates the formation of additional vacancies on the sub-lattice of opposite valency. Homovalent doping will usually result in a distortion in the crystal lattice, thus exerting an influence on the diffusion of atoms in the vicinity of the dopant.

Depending on the nature of the defects present in a solid, the motion of the atomic particles can be facilitated by various mechanisms. Considered the most important diffusion mechanism, the *vacancy mechanism* is the dominant one in metals and alloys for the diffusion of both the matrix atoms and the solute atoms. Here, the atoms move by simply exchanging

places with a vacancy; *cf.* Fig. 2.2 (b). The diffusivity thus strongly depends on the availability and the mobility of vacancies. Furthermore, in the case of substitutional solutes attractive or repulsive interactions with the vacancy can be the source of correlation effects.[39]

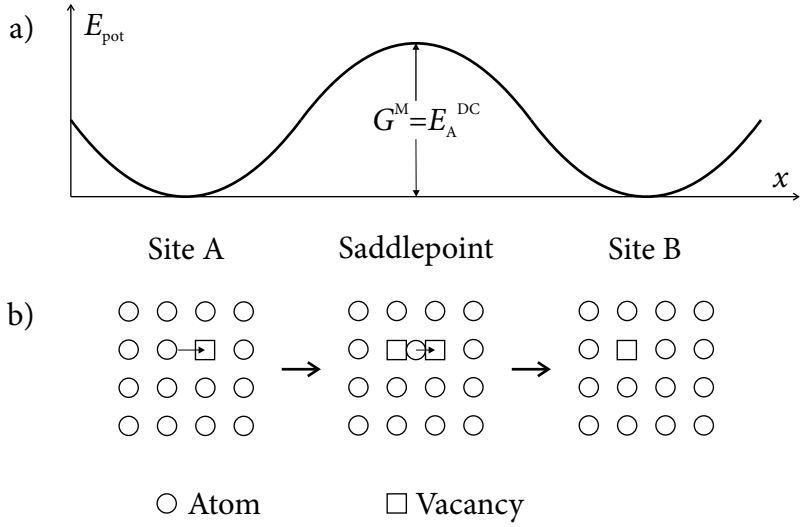

Figure 2.2: Schematic representation of the atomic jump process in the vacancy mechanism. The atom has to overcome an energy barrier (a) to change places with the vacancy (b). Notice that the potential energy of the atom is the same at the beginning and end of the jump. Adopted from [43] and [38].

The theory of the rate at which atoms move from one site to a neighbouring one was proposed by Wert [46] and has been refined by Vineyard [47]. Vineyard's approach is based upon the canonical ensemble of statistical mechanics for the distribution of atomic positions and velocities. The jump process can be viewed as occurring in an energy landscape characterised by the difference in Gibbs free energy G^M between the saddle-point barrier and the equilibrium position, see Fig. 2.2 (a). G^M is denoted as the Gibbs free energy of migration (superscript M) of the atom. It can be separated according to

$$G^M = H^M - TS^M , \tag{2.36}$$

where H^M denotes the enthalpy of migration and S^M the entropy of migration. Using statistical thermodynamics, Vineyard [47] has shown that the jump rate ω (number of jumps per unit time to a particular neighbouring site) and consequently the *activation energy* E_A^{DC} shows Arrhenius behaviour. Its temperature dependence can be expressed by an Arrhenius equation: [48,49]

$$\mu = \mu_0 \exp\left(\frac{-E_A^{DC}}{k_B T}\right), \tag{2.37}$$

with Boltzmann's constant k_B and the thermodynamic temperature T. μ_0 is a proportionality constant depending on several factors *e.g.*, the attempt frequency, the distance moved by the ion and the external electric field.

The theory of the rates at which atoms move from one lattice site to another covers one of the fundamental aspects of diffusion. For most practical purposes, a few general conclusions are important:

(*i.*) Atomic migration in a solid is the result of a sequence of localised jumps from one site to another.

(*ii.*) Atomic jumps in crystals usually occur from one site to a nearest-neighbour site. Molecular dynamic simulations mostly confirm this view. Multiple hops are rare, although their occurrence is indicated in some model substances. Jumps with magnitudes larger than the nearest-neighbour distance are more common on surfaces or in grain boundaries.

(*iii.*) The jump rate ω and the activation energy E_A^{DC} have an Arrhenius-type dependence on temperature.

(*iv.*) The concept of an atomic jump developed above applies to all possible diffusion mechanisms discussed; the values of G^M, H^M and S^M depend on the diffusion mechanism and on the material under consideration.

(*v.*) There are cases – mostly motion of hydrogen in solids at low temperatures - where a classical treatment is not adequate.[50] However, the end result of different theories including quantum effects is still a movement in a series of distinct jumps from one site to another.[51] For atoms heavier than hydrogen and its isotopes, quantum effects can usually be disregarded.

For more detailed discussions about defects and diffusion mechanisms in solids and the problem of thermally activated jumps, the interested reader is referenced to the works of Mehrer [38], Murch [39], Nowick and Burton [50] and Flynn and Stoneham [51].

3 Basics of Impedance Spectroscopy

3.1 Introduction

On its way through the circuit, electric energy may be (i) converted to other forms of energy *e. g.*, heat, phonones, light, electromagnetic waves, chemical energy or (ii) be stored in electric or (iii) magnetic fields.

In the first case, the potential energy W of the charge carrier with charge Q suffers from a decrease that leads to path-depending voltage drop ΔV:

$$\Delta V = \frac{\Delta W}{Q}\,. \tag{3.1}$$

If the energy loss ΔW is caused by *e. g.*, statistically equivalently distributed collisions in a homogeneous electric flow field, the resulting voltage drop ΔV is linearly depending on the electric current I and can be expressed by Ohm's law:

$$R = \frac{V}{I}\,, \tag{3.2}$$

with the resistance R. This condition is fulfilled, following the awareness of Georg Simon Ohm,[52] by many materials *e. g.*, metals at constant temperature.

In case (ii), the current influences an electrostatic field between two electrically insulated surfaces by displacement of charges. The ability of the body to store an electric charge is called *capacitance* C. It is a function of the area of the surfaces, the distance between them and the permittivity ε of the dielectric material enclosed. For many dielectric materials, the permittivity and thus the capacitance, is independent of the potential difference between the conductors and the total charge on them and can be expressed as:

$$C = \frac{Q}{V}\,. \tag{3.3}$$

A passive two-terminal electric component used to store electric energy temporarily in an electric field is called *capacitor*. The capacitance of a plate capacitor with large plates with

area A, a small distance d between them and a homogeneous electric field in its dielectric, can be estimated by:

$$C = \frac{A\varepsilon_r\varepsilon_0}{d}, \tag{3.4}$$

with the permittivity of vacuum ε_0 and the relative permittivity of the dielectric ε_r.

Thirdly, every arbitrarily shaped electric flow field is surrounded by a magnetic field, consequently a magnetic flux Φ occurs. It is especially intense when the conductor is shaped to a loop. The ratio between the magnetic flux passing through an area enclosed by an electric current to the current I around the border is called the *inductance* L of the arrangement:

$$L(I) = \frac{\Phi(I)}{I}. \tag{3.5}$$

In the case of linear dependence between Φ and I, L is independent of I. Thus, the inductance only depends on material properties and the geometry of the loop. By changing the magnetic flux through a conducting loop a voltage v_i is induced. It follows the *law of induction*:[53]

$$v_i = -\frac{d\Phi}{dt}. \tag{3.6}$$

Time-depending electric quantities will be denoted as lower-case letters by convention. A passive two-terminal electric component used to store electric energy temporarily in a magnetic field is called *inductor*. The inductance of a long and slim cylindrical coil can be estimated by:

$$L = \frac{\mu_0\mu_r N^2 A}{l}, \tag{3.7}$$

with the permeability of the vacuum μ_0, the relative magnetic permeability μ_r of the core material, the number of turns N, the cross section area A and the length l.

By joining Eqs. (3.5) and (3.6), we can calculate the induced voltage for an inductor with:

$$v_i = -L\frac{di}{dt}. \tag{3.8}$$

The *alternating current* (AC) impedance z of the three basic circuit elements resistor, capacitor, and inductor can now be derived. It is the measure of the opposition that a circuit presents to a current when a voltage is applied:

$$z = \frac{v}{i}\,, \tag{3.9}$$

with the time-depending values of voltage v and current i. Although the idea can be extended to define the relationship between the voltage and current of any arbitrary signal, these derivations will assume *sinusoidal* signals, since any arbitrary signal can be approximated as a sum of sinusoids through Fourier analysis.[54]

We consider a sinusoidal AC voltage v

$$v = V_\mathrm{p} \sin(\omega t)\,, \tag{3.10}$$

with the peak voltage or amplitude V_p, the angular frequency ω and the time t. Inserting Eq. (3.10) into (3.2), we get the current-voltage-relation and thus the impedance for a resistor Z_R:

$$\frac{v}{i} = \frac{V_\mathrm{p} \sin(\omega t)}{I_\mathrm{p} \sin(\omega t)} \quad = Z_R = R\,, \tag{3.11}$$

that means, there is a constant ratio between voltage and current of a resistor and there is no phase shift between them. Thus, the impedance for a resistor Z_R is equivalent to the resistance R.

For a capacitor, by derivation with respect to time, rearrangement of Eq. (3.3)

$$i = C\frac{dv}{dt}\,, \tag{3.12}$$

and inserting the sinusoidal voltage perturbation from Eq. (3.10)

$$\frac{dv}{dt} = \omega V_\mathrm{p} \cos(\omega t) \quad = \omega V_\mathrm{p} \sin(\omega t + \frac{\pi}{2})\,, \tag{3.13}$$

we get the current-voltage-relation, *i.e.* the impedance of the ideal capacitor:

$$z = \frac{v}{i} = \frac{\sin(\omega t)}{\omega C \sin(\omega t + \frac{\pi}{2})} \,. \tag{3.14}$$

This says that the ratio of AC voltage amplitude to AC current amplitude across a capacitor is $1/\omega C$, and that the AC voltage lags the AC current across a capacitor by 90 degrees (or the AC current leads the AC voltage across a capacitor by 90 degrees, or the phase of the AC current is shifted by 90 degrees before the AC voltage).

This result can be expressed in polar form:

$$\tilde{Z}_C = \frac{1}{\omega C} \exp(j\frac{\pi}{2}) \,, \tag{3.15}$$

or in Euler's formula, as

$$\tilde{Z}_C = \frac{-j}{\omega C} = X_C \,, \tag{3.16}$$

also known as the *reactance* of the ideal capacitor X_C. In both cases the tilde is used to denote complex quantities by convention. In the case of the inductor, we start with the sinusoidal current i, for easier derivation,

$$i = I_\mathrm{p} \sin(\omega t) \,, \tag{3.17}$$

with the peak current I_p. Inserting in Eq. (3.8), we get

$$v = -L \frac{d(I_\mathrm{p} \sin(\omega t))}{dt} \,, \tag{3.18}$$

and thus

$$\frac{v}{i} = \frac{\omega I_\mathrm{p} L \cos(\omega t)}{I_\mathrm{p} \sin(\omega t)} \quad = \frac{\omega L \sin(\omega t + \frac{\pi}{2})}{\sin(\omega t)} \,. \tag{3.19}$$

This says that the ratio of AC voltage amplitude to AC current amplitude across an inductor is ωL, and that the AC voltage leads the AC current across an inductor by 90 degrees. Expressed in polar form we get

$$\tilde{Z}_L = \omega L \exp(j\frac{\pi}{2}) , \tag{3.20}$$

or in Euler's formula

$$\tilde{Z}_L = j\omega L = X_L , \tag{3.21}$$

also known as the *reactance* of the ideal inductor X_L.

The findings from above show that a sinusoidal current passing through the network elements R, L, C, produces a sinusoidal, possibly phase shifted voltage response with the same frequency. The correlation can be described by two quantities: (i) the *apparent impedance* Z_{app}

$$Z_{\text{app}} = \frac{V_{\text{p}}}{I_{\text{p}}} . \tag{3.22}$$

It has the dimension of an ohmic resistor, but should not be confused with a resistance, because the peak values in the fraction appear at different times. It is a calculation quantity supplying, by convention, a resistance term formally equal to *direct current* (DC) quantities. [55] It is also applicable for electric dipoles with more then one circuit element. (ii), the *phase shift* or *phase angle* ϕ between the peak values of voltage and current

$$\phi = \phi_v - \phi_i . \tag{3.23}$$

Using Eqs. (3.22) and (3.23), the time dependent voltage v for an electric dipole can be expressed as

$$v = V_{\text{p}} \sin(\omega t + \phi_v) \quad = Z_{\text{app}} I_{\text{p}} \sin(\omega t + \phi + \phi_i) . \tag{3.24}$$

Using Euler's formula this can be written as

$$\begin{aligned} \tilde{Z} &= |\tilde{Z}|(\cos(\phi) + i \sin(\phi)) \\ &\equiv Z' + iZ'', \end{aligned} \tag{3.25}$$

where the real part $Z' = |\tilde{Z}| \cos(\phi)$ and imaginary part $Z'' = |\tilde{Z}| \sin(\phi)$ are marked by primes and double primes, respectively. Z' is equivalent to the so-called *resistance* R, and Z'' the *reactance* X of the electric circuit. Only the resistance contributes to energy conversion; the reactive part makes the electric energy swing between generator and load. As the phase

angle ϕ between R and X is always either + 90 or - 90 degrees, Z_{app} can be calculated with Pythagoras' formula:

$$Z_{\text{app}} = \sqrt{R^2 + X^2}\,. \tag{3.26}$$

A graphical representation of the linear impedance of an arbitrary electric dipole is the so-called *phasor-diagram*, see Fig. 3.1. Eq. (3.26) can be solved graphically via linear combination of resistive and reactive circuit elements.

3.2 Linear Impedance Spectroscopy

By Barsoukov's definition,[24] impedance spectroscopy (IS) is *a general term that subsumes the small-signal measurement of the linear electrical response of a material of interest (including electrode effects) and the subsequent analysis of the response to yield useful information about the physicochemical properties of the system*. *Linear* in this context means, that the impedance is independent of the applied voltage amplitude and the current response does not contain any other frequencies than the excitation signal. This requires the working point to be set to a linear region of the transfer function, as shown in Fig. 3.2.

To create an impedance *spectrum*, several frequency points are recorded. The result can be illustrated in various forms, the most common are the (i) Bode and the (ii) Argand or Nyquist diagram. (i) is a double-logarithmic plot of apparent impedance Z_{app} (and accordingly $|Z|$) and phase angle ϕ vs. frequency f. It has its origins in control engineering where it is used to illustrate the transfer function of an electric quadrupole. It contains all

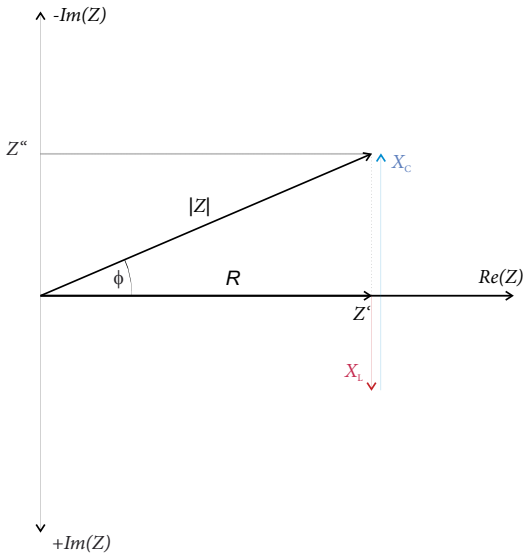

Figure 3.1: Complex plane plot of the impedance $\tilde{Z}$ illustrating the use of Cartesian (Z', Z'') and polar ($|\tilde{Z}|$, ϕ) coordinates. Graphical linear combination of the serially connected circuit elements R, L, C in the phasor diagram.

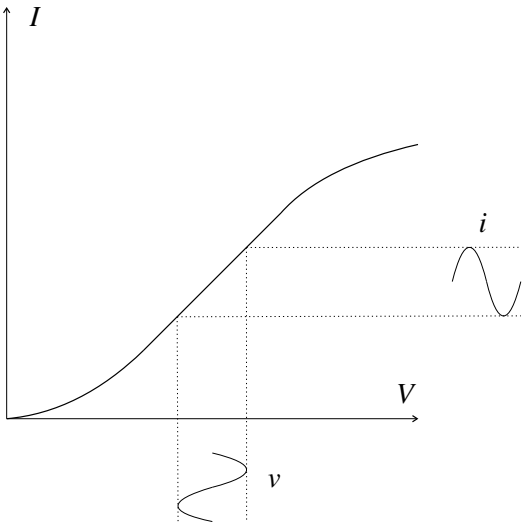

Figure 3.2: Voltage-current-diagram illustrating the selection of a linear working point for small-signal impedance measurement. Exciting sine voltage v and current response i are connected by a constant factor and thus show ohmic behaviour.

impedance information, corner frequencies and resonances can easily be identified. An example of a Bode diagram is shown in Fig. 3.3.

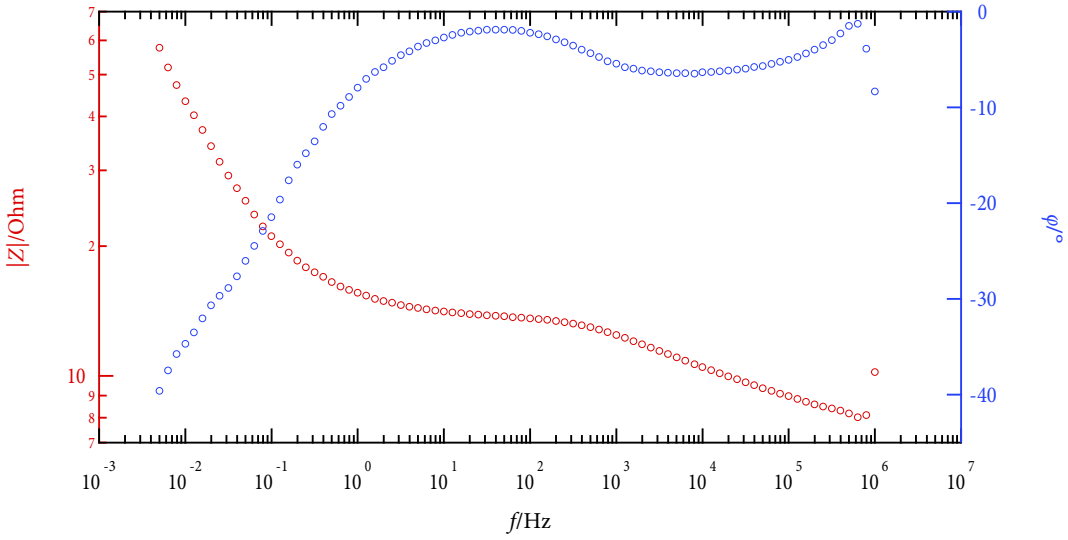

Figure 3.3: Bode diagram of the impedance of a Li-ion half cell with carbon electrode and liquid electrode. Apparent impedance $|Z|$, red markers, and phase angle ϕ, blue markers are plotted vs. frequency f.

(ii) is a linear plot of reactance Z'' vs. resistance Z'. It was originally designed to predict the stability of a control system and enables to illustrate impedance and phase information in a single plot. Nyquist diagrams graphically support the design of equivalent circuit models. The points shown in the plots can be imagined as the peaks of the phasors shown in the phasor

diagram in Fig. 3.1. Its disadvantage is the lack of any frequency information. In Fig. 3.4 the same data as in the Bode plot in Fig. 3.3 is shown as Nyquist plot.

3.3 Non-Linear Impedance Spectroscopy

If at the working point, amplitude and frequency are selected in a way that the current response cannot be scaled from the exciting voltage by a constant factor, the current response is *non-linear*, see Fig. 3.5.

That means, the signal includes not only the exciting frequency f_0, but also *higher harmonics*, that are multiples of the fundamental frequency. If the transfer function contains *e. g.*, a cubical term

$$i = v^2 \,, \tag{3.27}$$

the current response for sinusoidal voltage is

$$i = (v_0 \sin(\omega_0 t))^2 \quad = \frac{1}{2}(1 - \cos(2\omega_0 t)) \,. \tag{3.28}$$

The cubical term generates a second harmonic of the fundamental frequency f_0 (or the angular frequency ω_0, respectively). These distortions may occur (i) accidentally in electrochemical systems, because linearity can only be approached, or (ii) deliberately to analyse the shape of the transfer function.

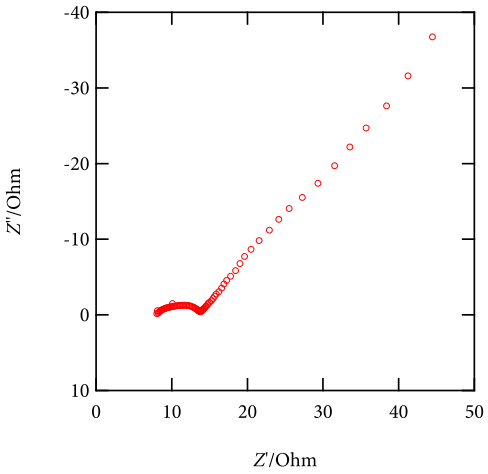

Figure 3.4: Nyquist diagram of the impedance of a Li-ion half cell with carbon electrode and liquid electrolyte. Reactance Z'' is plotted vs. resistance Z'. Note that the Nyquist plot does not show any frequency information.

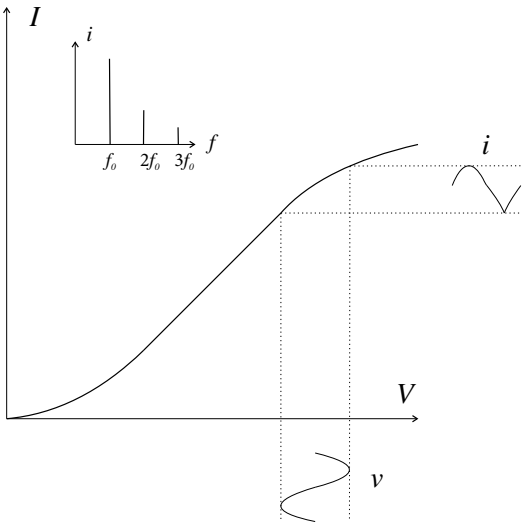

Figure 3.5: Voltage-current-diagram illustrating the selection of a non-linear working point. The exciting sine voltage v with frequency f_0 leads to a distorted current response i with higher harmonics (2 f_0, 3 f_0,...).

3.4 Impedance Spectroscopy for Lithium-Ion Batteries

The Li-ion battery is the most actively investigated battery of modern times. Its basic design consists of a cathode and anode with an open crystalline structure capable of repeatedly intercalating Li-ions, and a high-stability electrolyte and separator. In contrast to other battery types, a Li-ion battery uses an *aprotic* (no mobile hydrogen atoms) electrolyte. The need for such electrolyte arises because of the high cell voltage of the battery (4.2 V) which exceeds the water stability region both on the cathode and on the anode side. Impedance is typically measured in a two- electrode or three electrode (with reference) configuration. The electrolyte is compressed between two blocking (steel, platinum) or non-blocking Li electrodes.[56] Interpretation of impedance spectra for batteries can be traced back to Randles[57] (1947), and has proven to remain valid until the present. A typical impedance spectrum for a lithium-ion battery is shown in Fig. 3.6.

The contributions to a lithium-ion battery's impedance can be summed up following Barsoukov:[24]

(*i.*) Electrodes: Separate impedance investigation of electrodes is possible using a three electrode configuration, where the electrode of interest (anode or cathode) is typically paired with a Li-metal counter electrode and a Li-metal reference electrode. This configuration assumes that the kinetics of Li at the counter electrode is faster than at the working electrode. A situation that is true for most of the cases.

(*ii.*) Anode: The surface impedance of a carbon anode is determined by two factors: the resistance and capacitance of the passivating layer and the charge transfer resistance of the intercalation reaction, followed by solid state diffusion toward the centre of the particles.

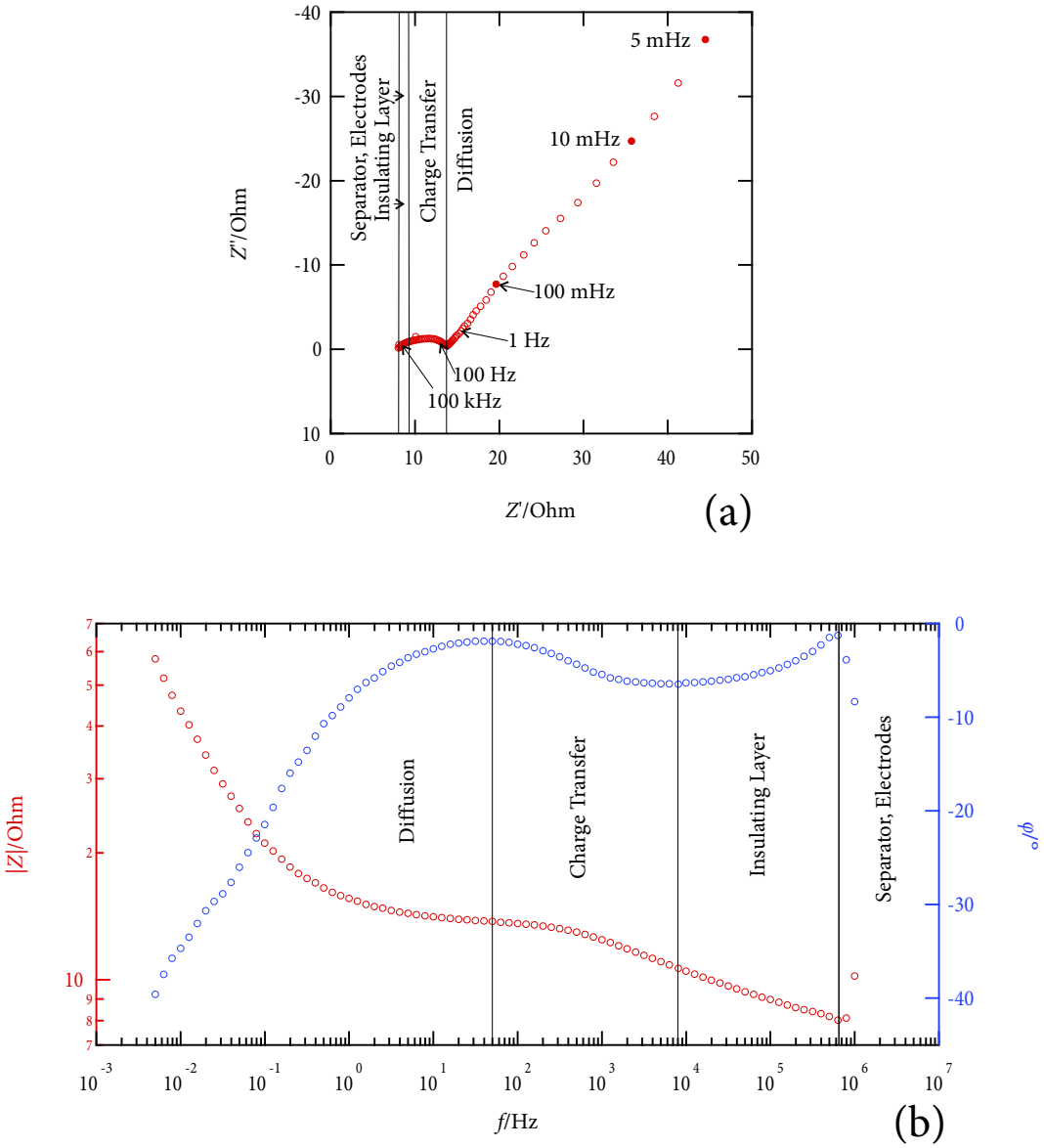

Figure 3.6: Nyquist (a) and Bode (b) diagram of a lithium-ion half cell with carbon electrode and liquid electrolyte. Contribution to impedance spectrum pointed out following [24].

(*iii.*) Cathode: The surface impedance of Li-intercalation cathode materials is similar to that of anodes and is dominated by surface film impedance and by charge transfer resistance. Capacity fading is also largely attributed to an increase of material resistance due to the growth of insulating layers on particle surfaces and the resulting particle disconnection.[58] Solid state diffusion in intercalation cathodes can only be analysed as part of an overall impedance model. The material resistance of the porous electrode can lead to an angle of 45 ° in the complex plot which is a diffusion effect in the pores in the liquid state. Non-linear fitting to a model which includes both diffusion and material resistance factors allows one to separate their effects because the diffusion effect is expressed only in the low-frequency area but material resistance influences all frequency regions.

(*iv.*) Solid electrolyte interphase: Impedance spectroscopy was first applied to the investigation of SEI on lithium-metal by Thevenin.[59] It can be seen that a high-frequency semicircle corresponding to the passivating layer grows noticeably at room temperature and is almost unchanged at low temperature, indicating a different character of the formed layer. Quantitative analysis of the surface characteristics is only possible by using a model that considers the porosity of the active layer because the influence of the ionic and electronic resistance of the active layer is important in all frequency ranges.

(*v.*) Electrolyte: In order to achieve high power, batteries always operate at a relatively high concentration of conductive salts in liquid electrolytes. In practice, this means that we have to consider only the diffusion contribution to electrolyte impedance, while conduction and relaxation effects of bulk electrolyte are shifted to the high-frequency region. However, because of the high concentration of the ions taking part in a charge/discharge reaction and the very thin electrolyte layer used in practical batteries, this impedance is negligible for most liquid electrolytes applied in practice, and its influence will only appear in the high-frequency region or, most commonly, as a series resistance contribution.

(*vi.*) Separator: The separator in a Li-ion battery is typically a thin microporous polypropylene film. It prevents the electrodes from shorting directly or through Li-microdendrite growth on overcharge, and it also serves as a thermal shut-down safety device. When heated above 150 °C (*e.g.*, due to an internal short in a cell) the separator melts and its pores close, thus preventing ionic current flow and thermal runaway. It is common to investigate the shut-down behaviour of separators by measurement of cell impedance at selected frequencies, such as 1 kHz, dependent on temperature.[60]

(*vii.*) Diffusion: Most battery electrodes comprise an open structure consisting of small particles compressed together. This structure does not have well-defined pores (such as cylindrical) but rather an irregular network of interconnected space between particles filled with electrolyte. The absence of well-defined pores of known tortuosity complicates ab initio deduction of electrolyte impedance; however, the frequency dependence

of the impedance of porous materials is well described by the ladder-network approach originally proposed by de Levie.[61] This transmission line model manifests in a 45 ° inclination of the impedance in complex plane in the low-frequency range.

(*viii.*) Charge transfer: It can be seen that changes in the charge transfer resistance (high-frequency depressed semicircle) and in the chemical diffusion coefficients defining the low-frequency dependence involve Li intercalation phase changes. The resistance and diffusion hindrance increase in areas where change from one phase to the next occurs. The value of impedance spectra for correlation with state of charge is problematic for the Li-ion battery because impedance increases and decreases in the course of discharge several times. Only multivariant correlation using information from multiple frequencies or multiple model parameters can allow confident estimation.[62]

(*ix.*) Wires and cell design. At frequencies above 100 kHz, the design of current collectors, wires, connectors, cell container and alignment of the reference electrode becomes a dominating factor. The measurement result is not only influenced by inductance, see Eq. (3.5), but also by the *skin effect*: It is the tendency of an alternating electric current to become distributed within a conductor such that the current density is largest near the surface of the conductor, and decreases with greater depths in the conductor.

3.5 Impedance Spectroscopy With Solid Electrolytes

Ionic conductivity σ is defined in the same way as electronic conductivity:[43]

$$\sigma = nZe\mu\,, \tag{3.29}$$

with the number of charge carriers per unit volume n, the formal electric charge of the mobile ion Z, the elementary charge e and their mobility μ, which is a measure of the drift velocity in a constant electric field. Conductivity σ is the inverse of the *resistivity* ρ and can be calculated from impedance data by normalising to the sample geometry:

$$\tilde{\sigma} = \sigma' + j\sigma'' \quad = \frac{d}{A(Z' + jZ'')}\,, \tag{3.30}$$

with the sample thickness d and the cross section area A. Fig. 3.7 shows the conductivity spectrum of an ion conductor with negligible electronic conductivity in the shape of a Bode diagram.

According to Funke,[63] the most important properties of conductivity spectra at frequencies up to the MHz range are:

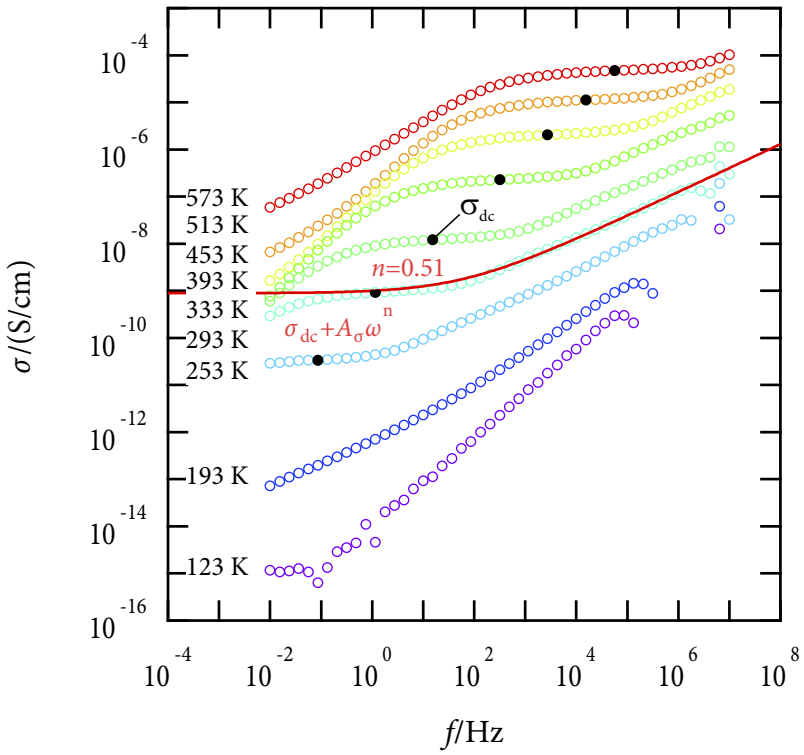

Figure 3.7: Selected conductivity spectra of nanocrystalline Li_2TiO_3 represented as Bode diagram. The Jonscher power exponent n is fitted to describe conductivity dispersion at higher frequencies.

(*i.*) As ionic conductivity in solids takes place as hopping process from one defect to another, an energy barrier must be overcome to enable a jump. This energy is known as the *activation energy* E_A^{DC}. Its temperature dependence can be expressed by an Arrhenius equation: [48,49]

$$\mu = \mu_0 \exp\left(\frac{-E_A^{DC}}{k_B T}\right), \tag{3.31}$$

with Boltzmann's constant k_B and the thermodynamic temperature T. μ_0 is a proportionality constant depending on several factors *e.g.*, the attempt frequency, the distance moved by the ion and the external electric field. At electric fields below 300 V/cm, a temperature dependence is introduced into the pre-exponential factor (see also Sec. 2.4). Combining this information with Eq. (3.31), we get an expression for the *direct current* (DC)-conductivity at low frequencies and intermediate temperatures:

$$\sigma_{DC} = \frac{\sigma_0}{T} \exp\left(\frac{-E_A^{DC}}{T}\right). \tag{3.32}$$

The term σ_0 now contains n, Ze and the information on attempt frequency and jump distance. This expression accounts for the fact that ionic conductivity increases with temperature. If we now take logs of Eq. (3.32) we get:

$$\ln \sigma_{DC} = \ln \sigma_0 - \frac{E_A^{DC}}{T}. \tag{3.33}$$

Plotting $\ln \sigma_{DC}$ vs. $1/T$ (and accordingly $1000/T$) should produce a straight line with a slope of $-E_A^{DC}$. This so-called Arrhenius plot for selected micro- and nano-crystalline solid state ionic conductors is shown in Fig. 3.8.

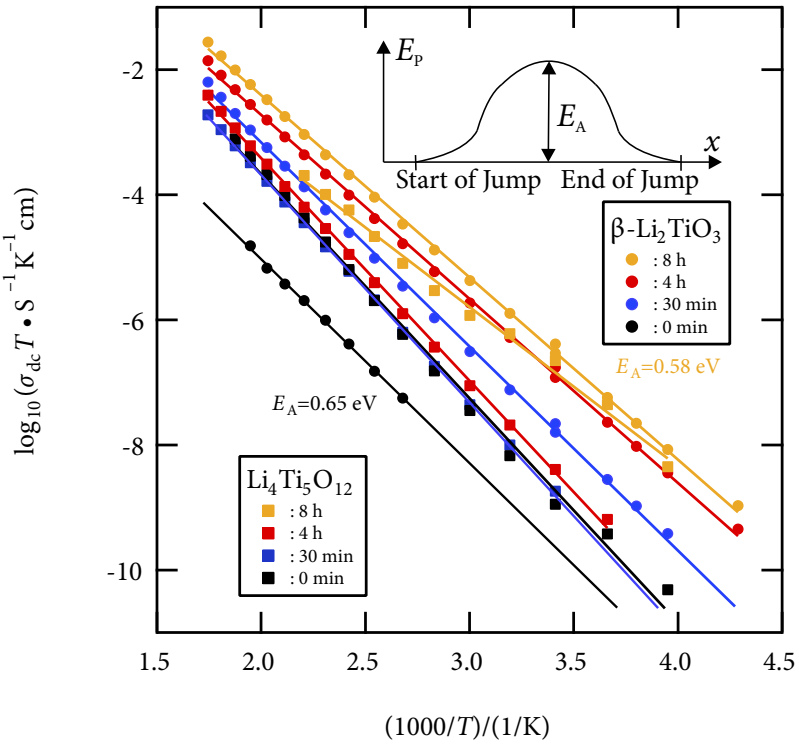

Figure 3.8: Arrhenius plot of selected micro- and nano-crystalline solid state ionic conductors as a function of milling time. E_A^{DC} pointed out as potential energy E_P barrier to be overcome between two lattice defects.

(*ii.*) At higher frequencies the conductivity $\sigma'(f)$ increases monotonically with f up to the order of phonon frequencies. This dispersive regime originates from non-ideal behaviour of real solids. Thus, various correlation effects introduced by interactions between the diffusing ions, lattice defects, the motion of a large number of charge carriers, and the response of the rigid lattice to ion jumps can contribute to the frequency dependence of the conductivity.[64]

(*iii.*) Taking both previous points together, the initial part of the spectra can be reasonably well described by the *Jonscher power law* $\sigma' = \sigma_{\mathrm{DC}} + A_\sigma \omega^n$. In the log-log plot, the exponent n—usually being between 0.6 and 0.7—corresponds to the slope of the dispersive part. This behaviour is observed in a wide range of solids (see Fig. 3.7) and is known as the *universal dielectric response*.[65]

(*iv.*) With decreasing temperatures the onset of the dispersive regime is shifted to lower frequencies and its slope approaches the value of 1. Also, the temperature dependence of the conductivity decreases, which amounts to $\sigma' \propto f$. This corresponds to a frequency independent dielectric loss $\varepsilon'' \neq f(f)$, a phenomenon commonly known as *nearly constant loss* (NCL). Although NCL behaviour is found for a wide range of ion conducting solids, [66–72] it is yet not fully understood. However, it is often associated with strictly localised motions and should not be mixed up with "real" translational jumps of the conducting ions.[63,73,74] Related to the dielectric permittivity $\tilde{\varepsilon} \equiv \varepsilon' - i\varepsilon''$ is the modulus function $\tilde{M} \equiv M' + iM'' = i\omega C_0 \tilde{Z}$. Here, $C_0 \equiv \varepsilon_0 A/d$ is the capacitance of the empty cell with electrode area A and electrode distance d. The high-frequency behaviour of M' and M'' is determined by the high-frequency limit of the permittivity $\varepsilon_\infty = \lim_{\omega\to\infty} \varepsilon'(\omega)$. The meaning of ε_∞ is discussed controversially in the literature [75] and should therefore be handled with care.

(*v.*) At elevated temperatures, the mobility of the migrating ions becomes significant enough to be observed in the form of polarisation effects at the ion blocking electrodes. This is reflected by a reduction of σ' for decreasing frequencies.

(*vi.*) While not displayed in Fig. 3.7, at very high frequencies—typically in the GHz range—the conductivity of ionic solids is governed by vibrational contributions, showing a f^2 frequency dependence on their low-frequency flank.[63,73,76]

It should be noted that $\sigma_{\mathrm{DC}} = \sum_i \sigma^i_{\mathrm{DC}}$ is generally a sum of conductivities of the ionic species i involved. In the materials presented in this thesis however, Li is the only species with significant diffusivity, so that σ_{DC} is assumed to have only one contribution.

4 X-ray Scattering Techniques

4.1 Introduction

Electromagnetic radiation with frequencies in the range from $3 \cdot 10^{16}$ Hz to $3 \cdot 10^{19}$ Hz is called *X-radiation* (composed of *X-rays*), corresponding to wavelengths ranging from 0.01 to 10 nanometres and energies in the range 100 eV to 100 keV. It was discovered in 1895 by Wilhelm Conrad Röntgen.[77] X-ray wavelengths are shorter than those of ultra violet (UV) light rays and typically longer than those of gamma rays. There is no consensus for a definition distinguishing between X-rays and gamma rays. One common practice is to distinguish between the two types of radiation based on their source: X-rays are emitted by electrons, while gamma rays are emitted by the atomic nucleus. [78–81] X-ray photons carry enough energy to ionise atoms and disrupt molecular bonds. X-radiation is therefore a kind of *ionising* radiation, and harmful to living tissue.

X-rays interact with matter in three main ways, through (i) photo-absorption, (ii) Compton scattering, and (iii) elastic scattering. The strength of these interactions depend on the energy of the X-rays and the elemental composition of the material, but not much on chemical properties since the X-ray photon energy is much higher than chemical binding energies. Photo-absorption or photoelectric absorption is the dominant interaction mechanism in the soft X-ray regime and for the lower hard X-ray energies. At higher energies, Compton scattering dominates.

(*i.*) The probability of a photoelectric absorption per unit mass is approximately proportional to Z^3/E^3, where Z is the atomic number and E is the energy of the incident photon.[82] This rule is not valid close to inner shell electron binding energies where there are abrupt changes in interaction probability, so called *absorption edges*, properties used in *X-ray absorption fine structure* (XAFS) and *X-ray absorption near edge structure* (XANES) techniques. However, the general trend of high absorption coefficients and thus short penetration depths for low photon energies and high atomic numbers is very strong. For soft tissue photo-absorption dominates up to about 26 keV photon energy where Compton scattering takes over. For higher atomic number substances this limit is higher. The high amount of calcium (Z=20) in bones together with their high density is what makes them show up so clearly on medical radiographs.

A photo-absorbed photon transfers all its energy to the electron with which it interacts, thus ionising the atom to which the electron was bound and producing a photo-electron that is likely to ionise more atoms in its path. An outer electron will fill the vacant

electron position and produce either a characteristic photon or an Auger electron. These effects can be used for elemental detection through X-ray spectroscopy or *Auger electron spectroscopy*.

(*ii.*) Compton scattering, discovered by Arthur Holly Compton,[83] is the predominant interaction between X-rays and soft tissue in medical imaging.[82] Compton scattering is an *inelastic* scattering of the X-ray photon by an outer shell electron. Part of the energy of the photon is transferred to the scattering electron, thereby ionising the atom and increasing the wavelength of the X-ray. The scattered photon can go in any direction, but a direction similar to the original direction is a bit more likely, especially for high-energy X-rays. The transferred energy can be directly obtained from the scattering angle from the conservation of energy and momentum.

(*iii.*) Elastic scattering of radiation may be described by the mechanical mass-spring-model.[84] We consider that electrons in matter behave as if they were bound by springs to their respective atoms. For present purposes, electromagnetic radiation (such as visible light or X-rays) consists of an oscillating electric field that, on reaching our electron-on-a-spring model of matter, drives the electric dipole at the frequency of the applied radiation. If the driving frequency ω is far from the natural frequency ω_0 of the driven oscillator, elastic scattering takes place. Two cases are distinguished:

a) Rayleigh scattering: If $\omega \ll \omega_0$ *e.g.*, the frequency of visible light corresponding to an electronic transition in an atom or molecule, the limit of the radiation intensity I_{scatt} is

$$\lim_{\omega \ll \omega_0} I_{\text{scatt}} = \text{constant} \cdot \frac{\omega^4}{\omega_0^4} \,. \tag{4.1}$$

This is the so-called *Rayleigh limit*, named after the British physicist Lord Rayleigh (John William Strutt).[85]

b) Thompson scattering: If $\omega \gg \omega_0$ *e.g.*, when X-rays or fast-moving electrons impinge on matter,

$$\lim_{\omega \gg \omega_0} I_{\text{scatt}} = \text{constant} \,. \tag{4.2}$$

This is the so-called *Thompson limit*, named after the British physicist Joseph John Thomson.[86] At the very high frequencies associated with X-rays or fast moving electrons the radiation wavelength has become small compared to the size of a typical molecule, and scattering from individual atoms or molecules can be detected.

In our days (2016), three different fundamental branches of technical X-ray application are distinguished:[25]

(*i.*) *X-ray crystallography* is a tool used for identifying the atomic and molecular structure of a crystal. X-rays with wavelengths in the dimension of the crystal are interacting with the electrons of the crystalline lattice and cause a beam of incident X-rays to diffract into many specific directions. By measuring the angles and intensities of these diffracted beams, a three-dimensional picture of the density of electrons within the crystal can be produced. From this electron density, the mean positions of the atoms in the crystal can be determined, as well as their chemical bonds, their disorder and various other information.

(*ii.*) *X-ray radiography* is an imaging technique that uses the penetration of X-rays, to view the internal structure of a non-uniformly composed and opaque object (*i.e.*, a non-transparent object of varying density and composition) such as the human body. To create the image, a heterogeneous beam of X-rays is projected toward the object. A certain amount of X-ray is absorbed by the object, which is dependent on the particular density and composition of that object *e.g.*, on the atomic number. The X-rays that pass through the object are captured behind the object and provide a superimposed 2D representation of all the object's internal structures.

(*iii.*) *X-ray fluorescence* (XRF) is the emission of characteristic *secondary* (or fluorescent) X-rays from a material that has been excited by bombarding with high-energy X-rays or gamma rays. The phenomenon is widely used for qualitative and quantitative elemental analysis and chemical analysis. A further application is the density measurement in multilayer systems.

4.2 X-ray Crystallography

Crystals are regular arrays of atoms whose electrons scatter X-rays. So an X-ray striking an electron produces secondary spherical waves emanating from the electron. This phenomenon is known as *elastic scattering*, and the electron is known as the scatterer. A regular array of scatterers produces a regular array of spherical waves. Although these waves cancel one another out in most directions through destructive interference, they add constructively in a few specific directions, determined by Bragg's law:[87]

$$2d \sin\theta = n\lambda \,. \tag{4.3}$$

Here d is the spacing between diffracting planes, θ is the incident angle, n is any integer, and λ is the wavelength of the beam. These specific directions appear as spots on the diffraction pattern called *reflections*. Thus, X-ray diffraction results from an electromagnetic wave (the X-ray) impinging on a regular array of scatterers (the repeating arrangement of atoms within

the crystal). Eq. (4.3) can be interpreted geometrically, as seen in Fig. 4.1.

For a perfect, infinity large crystal, a monochromatic incident beam would be refracted only in discrete angles. The refraction pattern would be composed of lines representing Dirac impulses.[25] In reality, the refraction pattern is influenced as follows:

(*i.*) The primary diffraction angle is proportional to the distance between the lattice elements of the crystal.

(*ii.*) The smaller the crystal, the larger the scatter around the primary angle and the higher the spreading of the reflection. This inherent width is called the Darwin width after the author of the first dynamical treatment of diffraction.[88] It is simply the result of uncertainty principle, [89–91]

$$\sigma_x \sigma_p \geqslant \frac{\hbar}{2}\,, \tag{4.4}$$

with the standard deviation of position σ_x, the standard deviation of momentum σ_x and the reduced Planck constant, $\hbar = h/(2\pi)$. It means that the absorption coefficient of the specimen requires that the location of the photon in a crystal be restricted to a rather small volume and thus that Δp and in turn $\Delta\lambda$, by the de Broglie relation[92]

$$\Delta p = \frac{h}{\Delta\lambda}\,, \tag{4.5}$$

must be finite, producing a finite width to the reflection. In addition to the inherent width, there are several physical sample effects which contribute to the observed profile *e.g.*, inhomogeneous strain and crystal lattice imperfections, dislocations, stacking faults, twinning, microstresses, grain boundaries, sub-boundaries, coherency strain, chemical heterogeneities, and crystallite smallness. (Some of those and other imperfections may also result in reflection shift, reflection asymmetry, anisotropic reflection broadening, or affect reflection shape.[93])

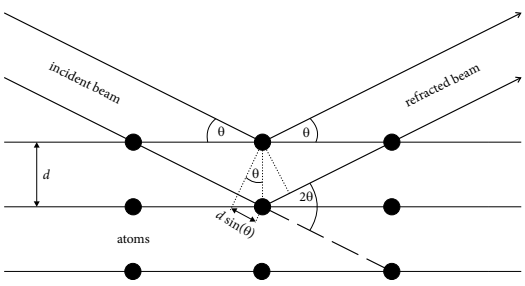

Figure 4.1: Diffraction of X-rays in a crystal. If scatterers are arranged symmetrically with a separation d, the refracted waves will be in sync (add constructively) only in directions where their path-length difference $2d \sin\theta$ equals an integer multiple (n) of the wavelength λ. In that case, part of the incoming beam is deflected by an angle 2θ, producing a reflection spot in the diffraction pattern.

(*iii.*) Amorphous material scatters the incident beam in no preferred direction and leads to a so-called *floor* in the diffraction pattern.

Typical X-ray reflections of micro- and nano-structured material are shown in Fig. 4.2.

A reflection is typically characterised by the so called *intrinsic profile*:

(*i.*) The *maximum intensity* $I_{\max}$ is reached at the diffraction angle θ_0, also known as *glancing angle*.

(*ii.*) The *floor* is the signal level distributed over the whole range of angles that cannot be assigned to any crystal lattice.

(*iii.*) The *net intensity* I_0 is the difference between maximum intensity and floor level.

(*iv.*) The difference between the left and the right border of the reflection at half net intensity ($I_0/2$) is called the *full width at half maximum* (FWHM). Real reflections have asymmetric shape and tails that contain further physical information.

For correct data analysis has furthermore to be taken into account that the spectrum of the X-ray tube is not homogeneous. This influence is characterised in the so-called *X-ray tube profile*. Further reflection-broadening factors are radiation, aperture, specimen geometry and specimen absorption profile, composite in the *instrument profile*. Thus, the measured profile is always a convolution of the intrinsic, the X-ray tube and the instrument profile.

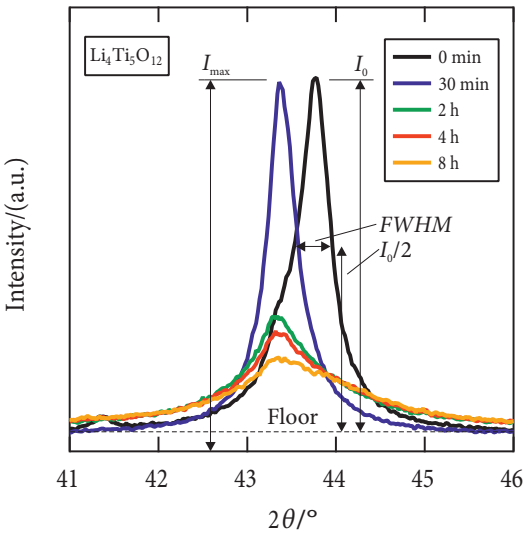

Figure 4.2: Reflections of $Li_4Ti_5O_{12}$ with different crystal sizes and different amount of amorphous material prepared by ball milling (milling times shown in the legend). The intensity of the refracted beam is shown versus the refraction angle (2θ). Characteristic parameters are highlighted: maximum intensity $I_{\max}$, net intensity I_0 and full width at half maximum FWHM. With increasing milling time the crystal diameter decreases, while the amount of amorphous material increases. This leads to a reflection broadening and an increasing signal floor.

4.3 Quantitative Phase Analysis

A phase in sense of thermodynamics is an entity of the same structure,[25] *e.g.*, chemical elements, poly-crystals or chemical compounds. These phases may be crystalline or amorphous and appear in mono- or poly-phase materials. As of now (2016), a quantitative phase analysis is still not possible fully automated. An established resource are databases of X-ray diffraction patterns and crystal structures. Each unitary symmetry is assigned to specific diffraction pattern. If two unitary symmetries are mixed, the diffraction patterns are superimposed and the reflections of both emerge in the pattern. Fig. 4.3 (a), '0 h', shows an X-ray diffraction pattern with 3 identified crystalline phases. By determination of the refraction angle and the ratio between the intensities of the reflections the stoichiometric ratio of the phases in the specimen can be calculated.

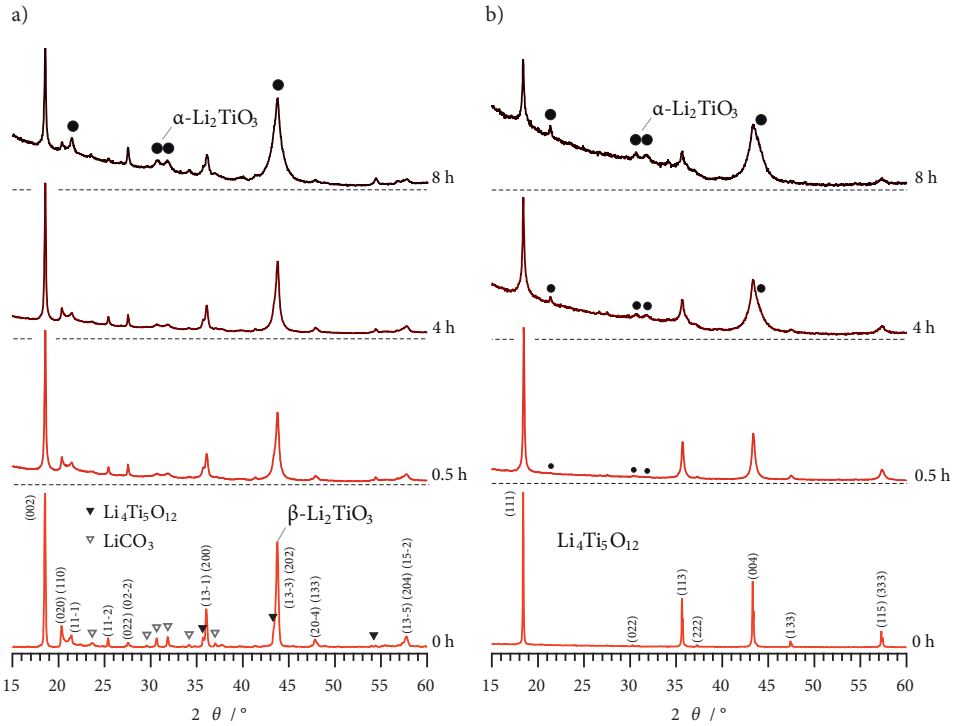

Figure 4.3: XRD powder pattern for a) β-Li_2TiO_3 and b) spinel-type $Li_4Ti_5O_{12}$. Compared to the non-treated source materials broadening of the reflections is observed that can be ascribed to grain size effects and strain generated during milling. With increasing milling time the amount of amorphous material increases; after several hours of mechanical impact reflections of the α-form of Li_2TiO_3 emerge.

A mixture of an amorphous and a crystalline phase does not change the shape of the refraction patterns significantly; if applicable, a so called *glass hill* in the signal floor of the pattern of an amorphous material may also appear in the mixture, see *e.g.*, Fig. 4.3 (a), in

the transition between '4 h' and '8 h'. In the case of synthesis of a new crystal structure, the diffraction pattern may be completely different to the source material. In Fig. 4.3 *e.g.*, after several hours of mechanical impact reflections of the α-form of Li_2TiO_3 emerge, that were not visible in the unmilled samples of the source material.

For more information about X-ray crystallography the interested reader is referenced to the works of Spiess [25] and Marshall [84].

5 Results

5.1 Introduction

Below, the results of this dissertation are presented cumulatively in the form of two papers published in peer-reviewed journals and two unpublished manuscripts. The chapter has been arranged into two sections defined by the aggregate state of the investigated electrolyte at room temperature.

The first section is about solid electrolytes, starting with an article comparing two relatively poor Li-ion conductors: Li_2TiO_3 and $Li_4Ti_5O_{12}$. The ionic conductivity is increased my mechanical treatment and the transport properties are investigated *via* electrochemical impedance spectroscopy (EIS). The first unpublished manuscript covers a more promising Li-ion conductor: Li_3PS_4 is synthesised mechanically followed by heat treatment. The conductivity of the crystalline γ-phase almost keeps up with amorphous and glass-ceramic material.

In the second section, the behaviour of liquid Li-ion conductors, half cells and full cells is investigated. In the second journal paper, two- and three-electrode Swagelok type T-fittings are used to assemble Li-ion half cells with liquid electrolyte and different anode materials. The ionic conductivity is measured *via* EIS over the lifetime and post mortem analysis is done *via* electron microscopy. In the second unpublished manuscript, Si based Li-microbatteries designed for on-chip assembly are investigated. The ionic conductivity of the liquid electrolyte is measured over a wide temperature range and the microcells are reviewed for any possible performance loss due to temperature cycling.

5.2 Solid Electrolytes

5.2.1 Li-Ion Dynamics in Nanocrystalline and Structurally Disordered Li_2TiO_3 (Paper 1)

Brandstätter H., Wohlmuth D., Bottke P., Pregartner V., and Wilkening M. *Zeitschrift für physikalische Chemie* **229**, 1363–1374 (2015).—This article is reproduced by permission of Walter de Gruyter GmbH. The original article can be found online at
http://dx.doi.org/10.1515/zpch-2014-0665.

Harald Brandstätter, Dominik Wohlmuth, Patrick Bottke, Veronika Pregartner, and Martin Wilkening*

Li Ion Dynamics in Nanocrystalline and Structurally Disordered Li_2TiO_3

DOI 10.1515/zpch-2014-0665
Received December 19, 2014; accepted March 23, 2015

Abstract: The monoclinic polymorph of Li_2TiO_3 (β-form) is known to be a relatively poor Li ion conductor. Up to now, no information is available on how the ion transport properties change when going from well-ordered crystalline Li_2TiO_3 to a structurally disordered form with the same chemical composition. Here, we used high-energy ball milling to prepare nanocrystalline, defect-rich Li_2TiO_3; ion dynamics have been studied *via* impedance spectroscopy. It turned out that ball milling offers the possibility to enhance long-range ion transport in the oxide by approximately 3 orders of magnitude. Its effect on the oxide ceramic is two-fold: besides the introduction of a large number of defects, the originally μm-sized crystallites are decreased to crystallites with a mean diameter of less than 50 nm. This process is accompanied by a mechanically induced phase transformation towards the α-form of Li_2TiO_3; besides that, a significant amount of amorphous materials is produced during milling. Structural disorder in nanocrystalline as well as amorphous Li_2TiO_3 is anticipated to play the capital role in governing Li ion dynamics of the sample finally obtained.

Keywords: Ion Conductivity, Nanocrystalline Ceramics, Impedance Spectroscopy, Ball Milling.

1 Introduction

The development of powerful electrochemical energy storage systems, which are based on Li charge carriers, is more important today than at any time before [1]. The design of thin-film all-solid-state batteries [2] may require protective layers

***Corresponding author: Martin Wilkening,** Institute of Chemistry and Technology of Materials, CD-lab for Li-Batteries, Stremayrgasse 9, 8010 Graz, Austria, e-mail: wilkening@tugraz.at
Harald Brandstätter, Dominik Wohlmuth, Patrick Bottke, Veronika Pregartner: Institute of Chemistry and Technology of Materials, Stremayrgasse 9, 8010 Graz, Austria

between the electrolyte-electrode contact that prevent the system from interfacial degradation during operation. The oxide materials foreseen should be able to prevent the formation of blocking interphases due to interdiffusion phenomena between the electrochemically active material and the Li-conducting solid electrolyte.

While ion transport in nanocrystalline, defect-rich $LiMO_3$ (M = Ta, Nb) has extensively been studied previously [3–5], little is known about Li^+ dynamics in, e.g., $LiAlO_2$ [6] or the various Li-bearing titanates such as Li_2TiO_3 [7] if these oxides are present in an amorphous or nanocrystalline form [8, 9]. Here, we used high-energy ball milling to prepare phase pure nanocrystalline Li_2TiO_3 starting from a commercially available coarse-grained material characterized by µm-sized crystallites. Ion transport has been studied by temperature-variable and frequency-dependent conductivity measurements.

In general, a compacted nanocrystalline ceramic, which has been prepared *via* a top-down approach such as ball-milling, consists of agglomerated crystallites characterized by a mean diameter in the order of 20 nm. The large volume fraction of interfacial regions and defects introduced is anticipated to govern macroscopic properties, particularly both short-range as well as long-range ion transport of the mobile cations [8–12]. In the present case, we focussed on the monoclinic modification, that is, the β-form of Li_2TiO_3 (see Figure 1). β-Li_2TiO_3, which crystallizes with the same space group as Li_2SnO_3, is one of the three polymorphs known for Li_2TiO_3 [13, 14]. Besides the β-modification an α- and a γ-form exist that show cubic symmetry [15, 16]. At approximately 1425 K the β-modification reversibly transforms into the γ-polymorph [15]. Whereas the specific Li ion conductivity is relatively poor in single crystalline and coarse grained polycrystalline β-Li_2TiO_3 (σ (573 K) = 4×10^{-6} S cm^{-1}) [7, 17], in the present contribution we will show that mechanical treatment of the titanate for about 30 min in a high-energy planetary mill leads to an increase of σ by almost 3 orders of magnitude. The results obtained for layer-structured β-Li_2TiO_3 are briefly compared with those collected for another Li titanate *viz.* spinel-type $Li_4Ti_5O_{12}$ (LTO), which is a well-known zero-strain anode material for lithium-ion batteries [18–21].

2 Experimental

Lithium titanate with a purity of ca. 99% was obtained from Alfa Aesar. The grain size of the non-treated raw material is in the µm range (see Figure 2) and reveals the typical X-ray powder diffraction pattern of the β-phase of Li_2TiO_3

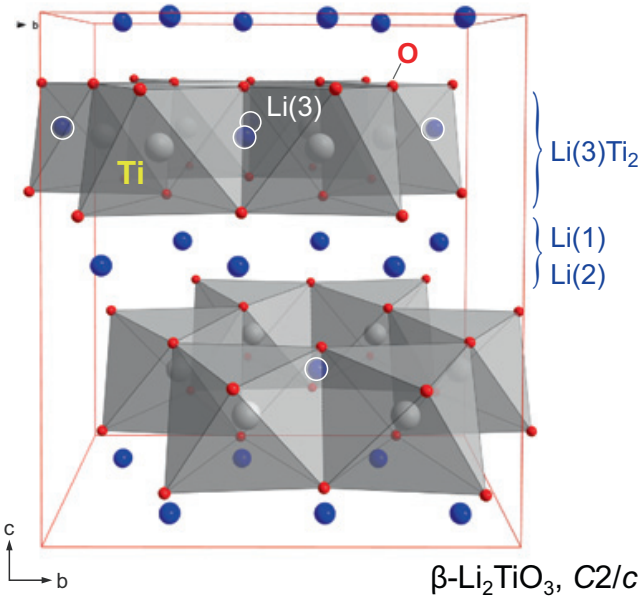

Figure 1: Crystal structure of monoclinic β-Li_2TiO_3 crystallizing with $C2/c$ symmetry. Li ions reside either in the $LiTi_2$ layers (Li(3), 4e site) or occupy octahedrally coordinated positions in between (Li(1) and Li(2), i.e., the 8f and 4d sites).

(see Figure 1). Nanocrystalline β-Li_2TiO_3 was prepared from the microcrystalline source material by ball milling using a high-energy planetary mill (Fritsch, Pulverisette 7). We used grinding beakers made of zirconium dioxide (Fritsch) that were equipped with 180 milling balls (ZrO_2, 5 mm in diameter). The air-tight beakers were filled and unfilled in inert gas atmosphere with less than 0.5 ppm water vapor content to avoid any contact of the ball-milled samples with air or moisture. To obtain different nanocrystalline samples the milling time was varied from 30 min to 8 h; the rotational speed of the mill was set to 400 rpm.

For structural characterization X-ray powder diffraction patterns were recorded on a Bruker D8 Advance diffractometer with Bragg Brentano geometry using Cu Kα radiation (10 to 100 °2θ, step size 0.02 °2θ, and step time 1 s). Rietveld refinement was carried out with an X'Pert HighScore Plus software package (PANalytical). ^{6}Li magic angle spinning (MAS) NMR spectra were recorded with a single-pulse sequence using an Avance-500 NMR spectrometer (Bruker, 73.6 MHz resonance frequency for ^{6}Li) with field drift compensation at spinning speeds of up to 30 kHz (2.5-mm MAS probe, ambient bearing gas). Spectra were recorded non-selectively using a short pulse with a length of ca. 2 µs. They were referenced to crystalline Li acetate serving as second reference; the chemical shifts presented refer to aqueous LiCl being the primary reference.

For our broadband impedance measurements the powders were cold-pressed into dense tablets by means of a 10 mm press set in combination with a P.O.-Weber

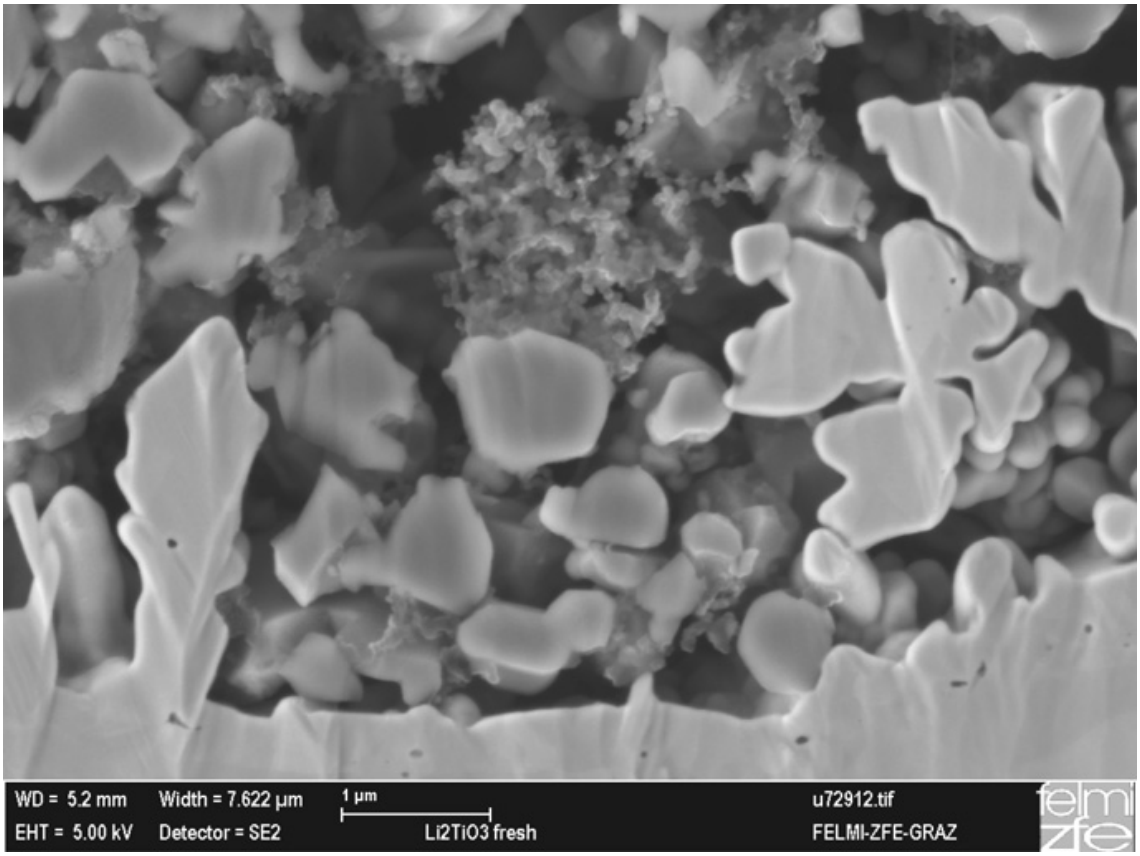

Figure 2: Slope cut SEM image of an electrode containing Li_2TiO_3 particles.

hand press that allows a uni-axial pressure of 10 kN. It is noteworthy that the heat-sensitive samples have not been sintered in order to avoid grain growth and healing of defects. Au electrodes of about 100 nm thickness were applied with a sputter coater (Leica EM SCD050). Temperature-variable 2-electrode impedance measurements were carried out with a Novocontrol Concept 80 broadband analyzer (Alpha-AN, Novocontrol) that is used in combination with a BDS 1200 cell and an active ZGS cell interface. The temperature in the sample chamber is automatically controlled with an accuracy of ±0.01 K by a QUATRO cyrosystem (Novocontrol) using a constant flow of freshly evaporated nitrogen gas that is heated up. The setup is able to record impedances and permittivities at frequencies ranging from few mHz up to 20 MHz (150 K to 570 K).

To measure the grain size of the sample *via* scanning electron microscopy (SEM) a solid-state electrode was prepared. The raw material was mixed with carbon-particulate matter, binder and resolvent (N-methyl-2-pyrrolidone). After stirring for several hours the viscous slurry was spread on a thin copper foil and dried in an oven at 333 K in vacuum. Small slices were punched out and slope cut for the SEM investigations. A representative SEM image is shown in Figure 2; the SEM settings are displayed at the bottom of the figure.

3 Results and discussion

3.1 Characterization *via* XRD and Li MAS NMR

Long-range crystal structures of the starting material as well as the presence and evolution of extra phases have been studied by X-ray powder diffraction (XRD). The XRD pattern of β-Li_2TiO_3 is shown in Figure 3; Miller indices are indicated. Triangles show minor impurities that can be identified as Li_2CO_3 and $Li_2Ti_5O_{12}$. With increasing milling time broadening of the reflections is seen that is due to shrinking the crystallites and the generation of lattice strain. Commonly, after several hours of intense ball-milling the average crystallite size is reduced from the µm range down to approximately 20 nm [9] as can be estimated *via* the well known equation introduced by Scherrer [22].

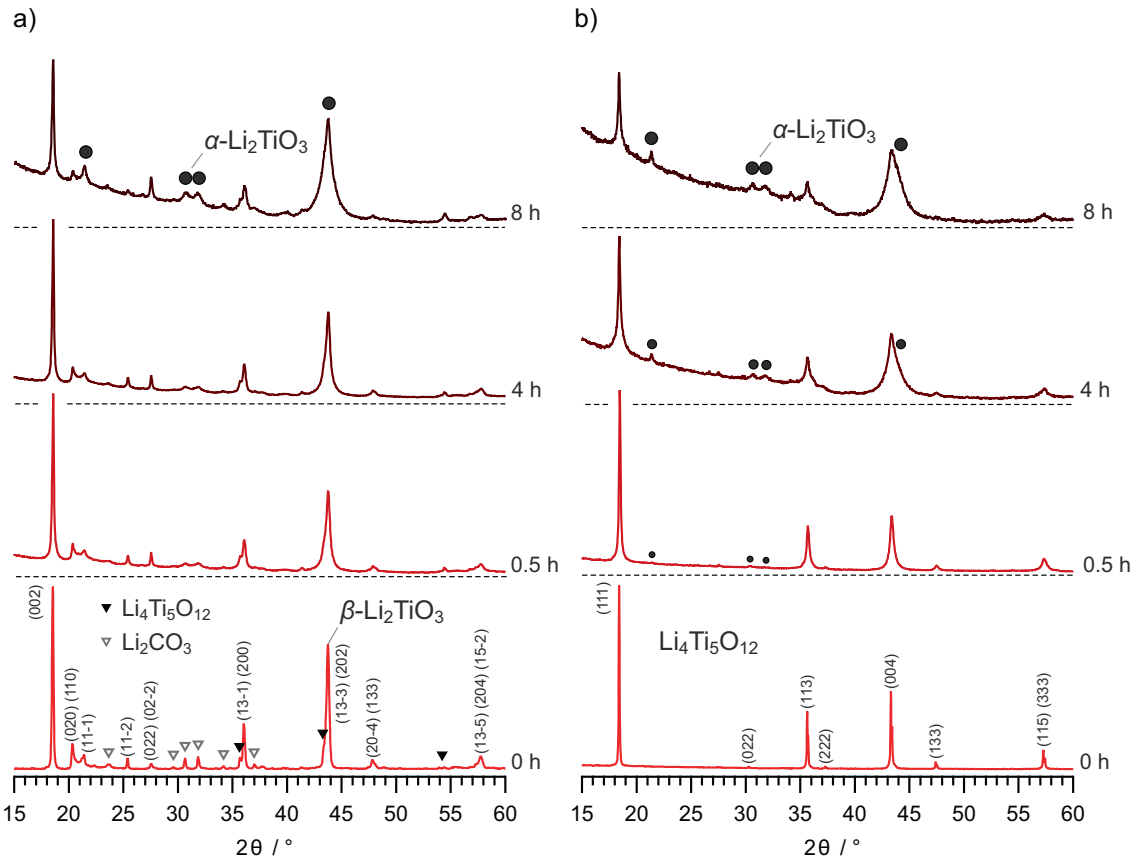

Figure 3: XRD powder pattern for a) β-Li_2TiO_3 and b) spinel-type $Li_4Ti_5O_{12}$. Compared to the non-treated source materials broadening of the reflections is observed that can be ascribed to grain size effects and strain generated during milling. With increasing milling time the amount of amorphous material increases; after several hours of mechanical impact reflections of the α-form of Li_2TiO_3 emerge.

Interestingly, with increasing milling time new reflections show up that can be assigned to the α-form or γ-polymorph of Li_2TiO_3 being high-pressure and high-temperature modifications of the titanate. Because of significant broadening of the XRD peaks we were not able to differentiate between these two phases. Besides the formation of metastable Li_2TiO_3 polymorphs the raise of the background signal points to the formation of a non-negligible amount of amorphous Li_2TiO_3 formed, which is anticipated to strongly influence the overall conductivities measured. The same is observed, but much less pronounced, for $Li_4Ti_5O_{12}$. Phase pure $Li_4Ti_5O_{12}$ partly transforms into the α-modification of Li_2TiO_3. This form is an NaCl-type thermodynamically metastable phase with cubic symmetry that undergoes re-transformation into the β-polymorph at $T > 575$ K, as mentioned above [16]. The crystal structure of cubic Li_2TiO_3 (Fm3m) shows a statistical distribution of lithium and titanium ions on the 4a position, oxygen ions occupy the 4b sites.

Similar observations have recently been reported on nanocrystalline $LiAlO_2$, which has also been prepared *via* high-energy ball milling starting with a coarse-grained source material [6]. Upon milling, $LiAlO_2$ turns into a mixture of amorphous $LiAlO_2$ with nm-sized crystallites embedded. At long milling times the δ-polymorph is formed, which is a high-pressure modification of the aluminium oxide [6].

Besides XRD we used ^{6}Li MAS NMR to enlighten local magnetic structures of the Li spins in β-Li_2TiO_3 and $Li_4Ti_5O_{12}$. The corresponding spectra are shown in Figure 4. For β-Li_2TiO_3 three signals can be resolved that may be attributed to the three magnetically different Li sites in the monoclinic structure (see above); according to the site occupation an intensity ratio of 1 : 1 : 2 is expected. This seems nicely fulfilled in our case especially when we consider a low amount of LTO present (see below). A ^{6}Li NMR spectrum of β-Li_2TiO_3 has also been reported recently [23].

Considering $Li_4Ti_5O_{12}$, Li ions reside on the 8a and 16c sites in the spinel structure yielding signals at 0.09 ppm and −0.26 ppm. This is in perfect agreement with data from the literature, see particularly the work of Irvine and coworkers [24]. The two partly overlapping lines nicely reflect the 3 : 1 ratio expected for $[Li]_{8a}[Li_{1/3}Ti_{5/3}]_{16d}[O_4]_{32e}$. The additional signal with very low intensity showing up at −0.89 ppm does, most likely, reflect X-ray invisible, i.e., amorphous, β-Li_2TiO_3. The same line is found for β-Li_2TiO_3; in the case of β-Li_2TiO_3 this NMR line, which seems to represent the Li(1) ions on the 8f position in the titanate, is the most intense signal. The same line also shows up after mechanical treatment of the sample. Note that a small amount of crystalline $Li_4Ti_5O_{12}$ is present in our β-Li_2TiO_3 sample (see Figure 3); for comparison, we have, there-

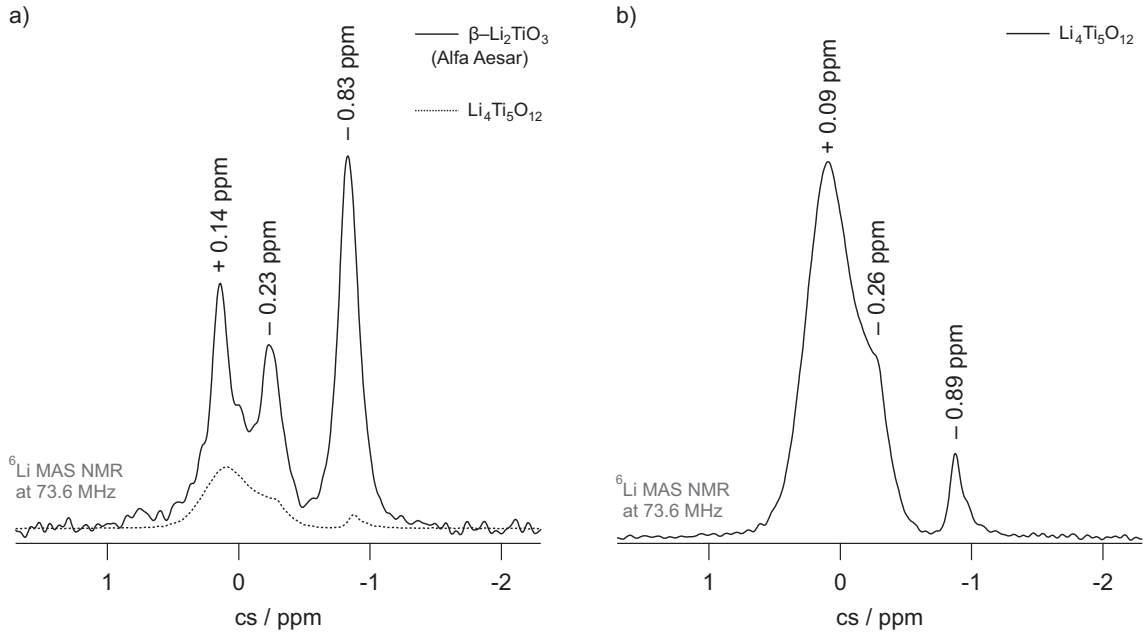

Figure 4: ^{6}Li MAS NMR spectra of the starting materials β-Li_2TiO_3 (a) and $Li_4Ti_5O_{12}$ (b); cs denotes the chemical shift in ppm. Spectra have been referenced to aqueous LiCl. The spinning speed was 28 kHz (a) and 30 kHz (b), respectively. To record the NMR spectra an interpulse delay of 180 s was used. Presumably, considering the spectrum of $Li_4Ti_5O_{12}$ this is too short to make visible minor impurities such as crystalline Li_2TiO_3 being characterized by extremely long spin-lattice relaxation times. The dotted spectrum in a) is scaled such that it is a guide to the eye.

fore, included the NMR spectrum of $Li_4Ti_5O_{12}$ in Figure 4a) that is simply scaled such that it serves to guide the eye.

3.2 Long-range ion transport in lithium titanate as probed by impedance spectroscopy

Impedance spectroscopy was used to characterize ion transport in β-Li_2TiO_3 as a function of mechanical impact. A set of conductivity isotherms is shown in Figure 5; they are composed of a low-frequency region, the so-called dc-plateau, and a dispersive regime that reflects Li ion hopping on shorter length scales. The conductivity plateau entails σ_{dc} (see the filled symbols in Figure 5a)), which is plotted in Figure 6 as $\sigma_{dc}T$ *vs* the inverse temperature.

Starting with relatively low conductivities for the non-treated starting material, σ_{dc} increases by about two orders of magnitude upon milling for 30 min. A further, but smaller increase is observed after high-energy ball milling for many hours. Simultaneously, the activation energy decreases by about 0.1 eV. The $\sigma_{dc}T$ values can be best approximated with two Arrhenius lines. While the data points

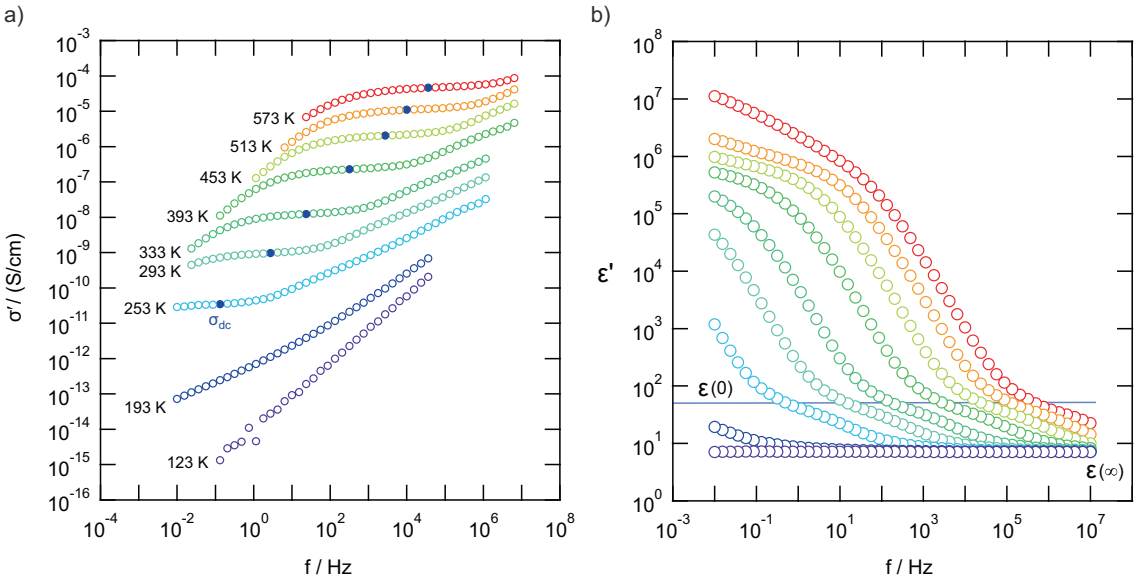

Figure 5: a) Conductivity spectra of β-Li_2TiO_3 that has been ball milled for 2 h in a high-energy planetary mill. Besides electrode blocking effects, being apparent at high temperatures and low frequencies, the spectra are typically composed of a dc-plateau region and a Jonscher-type [25] dispersive regime showing up at higher frequencies. b) Permittivity spectra indicating that mainly bulk properties are sensed *via* dielectric spectroscopy, at least for the ball-milled samples. σ' and ϵ' denote, in each case, the real part of the complex conductivity and permittivity, respectively.

follow an Arrhenius law characterized by 0.62 eV at lower temperatures, above 450 K the activation energy increases to approximately 0.72 eV. This behaviour has already been observed recently on a (highly dense) β-Li_2TiO_3 sample that was prepared from a melt [7]. The dashed line in Figure 5 reflects previous results obtained for that sample, see Ref. [7]. Most likely, the lower conductivity values of our starting material compared to the sample studied recently [7] reflect the influence of blocking grain boundary regions and extra phases formed, such as Li_2CO_3. Such phases may form a thin cover of the surfaces of the β-Li_2TiO_3 crystallites. Here, an activation energy of 0.65 eV for the starting material agrees well with the result of 0.7 eV found recently. In previous studies activation energies ranging from 0.6 to 1.1 eV were found [17, 26]; these results, most likely, depend on the exact stoichiometry and morphology of the samples studied.

Irrespective of the choice of the reference material, for non-treated β-Li_2TiO_3 an increase in $\sigma_{dc}T$ by about three orders of magnitude is found at room temperature. While at short milling times this increase is anticipated to be due to defects introduced into the β-modification of Li_2TiO_3, the additional raise at longer milling times might be attributed, at least partially, to the increasing formation of amorphous Li_2TiO_3 as well as the transformation into the α-form.

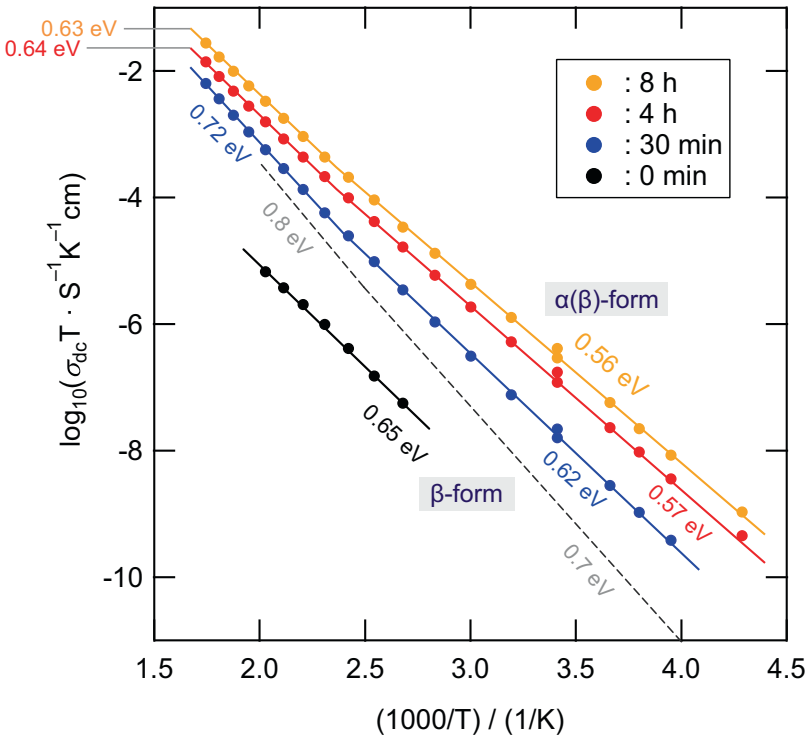

Figure 6: Arrhenius plot of $\sigma_{dc}T$ *vs* $1000/T$ of non-treated and ball-milled β-Li_2TiO_3; the dashed line indicates previous results on a microcrystalline sample that was obtained *via* quenching a Li_2TiO_3 melt [7].

Usually, the use of nanocrystalline, ball-milled powders yields more dense and less porous impedance pellets. On that score the amorphous structure of interfacial regions in samples that have been ball-milled for several orders is expected to be an additional advantage; they may serve as an aid to obtain dense pellets. Considering the permittivity spectra shown in Figure 5b) for a sample that has been treated for 2 h, $\epsilon(0)$ values being smaller than 100 correspond to capacities in the order of few pF. It turned out that $\epsilon(0)$ does not change if the milling time is increased; for the sample treated for 8 h the same value has been obtained. Hence, we assume that the electrical response mainly reflects bulk properties for all samples. Significant effects arising from ion blocking grain boundaries seem to be absent.

For comparison with the results obtained for nanocrystalline β-Li_2TiO_3, in the Arrhenius plot of Figure 7 conductivities for non-treated and ball-milled $Li_4Ti_5O_{12}$ are shown. In contrast to Li_2TiO_3 no large increase in overall conductivity is found even if we increase the milling time up to 8 h or more. We tend to explain the increase in σ_{dc} found after 8 h of milling to the formation of amorphous phases as well as the transformation into NaCl-type α-Li_2TiO_3 as is detected by XRD (see above).

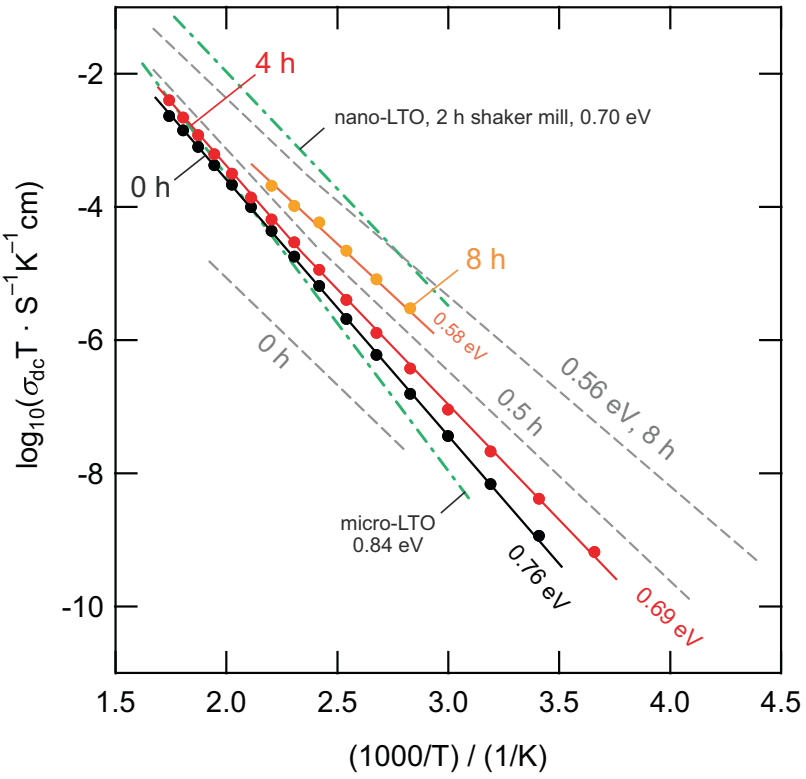

Figure 7: Arrhenius plot of $\sigma_{dc}T$ *vs* $1000/T$ of non-treated and ball-milled $Li_4Ti_5O_{12}$ (LTO). The dashed lines represent the Arrhenius lines of Figure 6 used to approximate the trend of $\sigma_{dc}T$ for β-Li_2TiO_3. The dashed-dotted lines refer to LTO (SüdChemie) that has been investigated by Iwaniak et al. [27], previously: the microcrystalline source material is characterized by 0.84 eV; after 2 h of milling in a shaker mill (SPEX) an increase of ion conductivity by about two orders of magnitude is seen when temperatures around 300 K are considered [27]. The corresponding XRD pattern of that sample does not reveal any large amounts of amorphous material; there is, however, abrasion of Al_2O_3 that may also affect Li ion transport.

Interestingly, and in contrast to our recent results, mechanical treatment of $Li_4Ti_5O_{12}$ in a shaker mill, as it was carried out by Iwaniak et al. [27], leads to a larger increase in $\sigma_{dc}T$. While the source material of Iwaniak et al. (purchased from SüdChemie, EXM1037) is comparable with our sample [27], milling the oxide for only 2 h in a shaker mill (SPEX), which is equipped with an alumina vial and a single ball of relatively large diameter (1 cm), seems to be more advantageous to enhance Li ion transport in LTO. A possible effect of abraded Al_2O_3 on Li dynamics [28–30] needs to be discussed in future studies; its influence, however, seems to be negligible here.

Compared to the present study, the corresponding XRD pattern in Ref. [27] does not reveal any large amounts of amorphous material formed. Obviously, the grinding effects known for planetary mills promotes the formation of disordered phases to a much larger extent. This might be of advantage if mechanochemical

reactions are desired to be induced but of disadvantage if nanocrystalline materials have to be prepared.

4 Summary

Ball milling is a versatile tool to change the morphology of a given material, to induce phase transformations, and to prepare nanocrystalline ceramics. Here, we focussed on poorly conducting β-Li_2TiO_3 to study the effect of mechanical treatment on overall conductivity. After a short milling period of only 30 min a significant increase in conductivity is found as was detected by impedance spectroscopy. This is ascribed to the large fraction of defects introduced during mechanical treatment.

At longer milling times amorphous phases are increasingly formed; furthermore, the oxide transforms into the α-modification which is a metastable form crystallizing with NaCl structure. The findings are comparable to a recent study on $LiAlO_2$ [6]. Comparisons with $Li_4Ti_5O_{12}$ show that the increase in conductivity is much less pronounced for LTO when treated in planetary mills. As in the case of β-Li_2TiO_3 a significant amount of amorphous material is formed, which is in contrast when LTO is treated in shaker mills yielding phase-pure nanocrystalline lithium titanate [27]. The latter finding and its relationship to Li ion dynamics might be important for battery applications with (nanostructured) LTO anodes prepared *via* high-energy ball-milling.

Acknowledgement: We thank B. Bitschnau for the XRD measurements and the subsequent analysis of the data. Financial support by the Deutsche Forschungsgemeinschaft (DFG Research Unit 1277, grant no. WI3600/2-1 and 4-2, SPP 1415) as well as by the Austrian Federal Ministry of Science Research and Economy, and the Austrian National Foundation for Research, Technology and Development is greatly appreciated.

References

1. R. V. Noorden, Nature **507** (2014) 26.
2. J. Bates, N. Dudney, B. Neudecker, A. Ueda, and C. Evans, Solid State Ionics **135** (2000) 33.
3. P. Heitjans, M. Masoud, A. Feldhoff, and M. Wilkening, Faraday Discuss. **134** (2007) 67.
4. M. Wilkening, V. Epp, A. Feldhoff, and P. Heitjans, J. Phys. Chem. C **112** (2008) 9291.
5. M. Pooley and A. Chadwick, Radiat. Eff. Defekt. S. **158** (2003) 197.

6. D. Wohlmuth, V. Epp, P. Bottke, I. Hanzu, B. Bitschnau, I. Letofsky-Papst, M. Kriechbaum, H. Amenitsch, F. Hofer, and M. Wilkening, J. Mater. Chem. A **2** (2014) 20295.
7. B. Ruprecht, M. Wilkening, R. Uecker, and P. Heitjans, Phys. Chem. Chem. Phys. **14** (2012) 11974.
8. P. Heitjans and S. Indris, J. Phys.-Condens. Mat. **15** (2003) R1257.
9. S. Indris, D. Bork, and P. Heitjans, J. Mater. Synth. Proces. **8** (2000) 245.
10. A. V. Chadwick, Diff. Fundam. **2** (2005) 44.
11. P. Heitjans, E. Tobschall, and M. Wilkening, Eur. Phys. J. – Special Topics **161** (2008) 97.
12. V. Epp, C. Brüning, M. Binnewies, P. Heitjans, and M. Wilkening, Z. Phys. Chem. **226** (2012) 513.
13. J. Dorrian and R. Newnham, Mater. Res. Bull. **4** (1969) 179.
14. J. Mikkelsen, J. Am. Ceram. Soc. **63** (1980) 331.
15. H. Kleykamp, J. Nucl. Mater. **295** (2001) 244.
16. C. Gicquel, M. Mayer, and R. Bouaziz, Compt. Rend. (Paris) Ser. C **275** (1972) 1427.
17. T. Fehr and E. Schmidbauer, Solid State Ionics **178** (2007) 35.
18. M. M. Thackeray, J. Electrochem. Soc. **142** (1995) 2558.
19. T.-F. Yi, L.-J. Jiang, J. Shu, C.-B. Yue, R.-S. Zhu, and H.-B. Qiao, J. Phys. Chem. Solids **71** (2010) 1236.
20. G.-N. Zhu, Y.-G. Wang, and Y.-Y. Xia, Energ. Environ. Sci. **5** (2012) 6652.
21. W. Schmidt, P. Bottke, M. Sternad, P. Gollob, V. Hennige, and M. Wilkening, Chem. Mater. **27** (2015) 1740.
22. P. Scherrer, Göttinger Nachrichten **2** (1918) 98.
23. M. Vijayakumar, S. Kerisit, Z. Yang, G. L. Graff, J. Liu, J. A. Sears, and S. D. Burton, J. Phys. Chem. C **113** (2009) 20108.
24. J. Kartha, D. Tunstall, and J. T. Irvine, J. Solid State Chem. **152** (2000) 397.
25. A. K. Jonscher, Nature **267** (1977) 673.
26. Ģ. Vītiņš, G. Ķizāne, A. Lūsis, and J. Tīliks, J. Solid State Electr. **6** (2002) 311.
27. W. Iwaniak, J. Fritzsche, M. Zukalová, R. Winter, M. Wilkening and P. Heitjans, Def. Diff. Forum **289-292** (2009) 565.
28. M. Wilkening, S. Indris, and P. Heitjans, Phys. Chem. Chem. Phys. **5** (2003) 2225.
29. S. Indris and P. Heitjans, J. Non-Cryst. Solids **307** (2002) 555.
30. S. Indris, P. Heitjans, M. Ulrich, and A. Bunde, Z. Phys. Chem. **219** (2005) 89.

5.2.2 Synthesis and Dynamics of Amorphous and Structurally Disordered Crystalline Li_3PS_4

Introduction

All-solid-state lithium-ion batteries based on solid electrolytes have attracted attention in recent years due to increased concerns on the safety problems of commercial lithium-ion batteries employing liquid electrolyte. [10–12] To date the most conductive solid electrolytes for lithium-ions are sulphide-based materials, which achieved 12 mS/cm conductivity at ambient temperature. [94] Fig. 5.1 shows the formation diagram of the Li-P-S system. In the binary Li_2S-P_2S_5 system, three stoichiometric compounds Li_3PS_4 [95,96], $Li_4P_2S_6$ [97], and Li_7PS_6 [98], were reported. Among all sulfide-based solid electrolytes, the stoichiometric compound of lithium thiophosphate, Li_3PS_4 is considered as the most chemically stable compound against metallic lithium. [99] Another merit of sulphide electrolytes is easy reduction of grain-boundary resistance by conventional cold-press of electrolyte powders; [100] this mechanical property of sulphides is preferable for application to all-solid-state batteries. Li_2S-P_2S_5 glass-ceramic electrolytes were used in all-solid-state batteries and the batteries exhibited excellent cycle performance. [101]

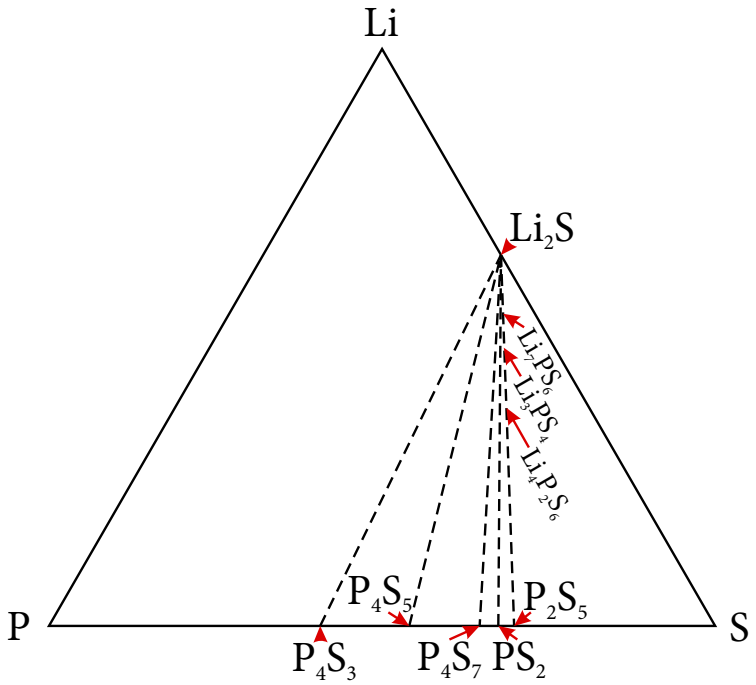

Figure 5.1: Ternary phase diagram for Li-P-S system, adopted from [102].

There are three transitions among the α, β and γ-phases of this material as a function of temperature. [103] The low-temperature γ-phase transformed to the medium-temperature β-phase at 573 K, which then transforms to the high-temperature α-phase at 746 K. The γ-phase is

iso-structural with β-Li_3PO_4 (SG: Pmn21) with an orthorhombic cell with a=7.70829(11), b=6.53521(10), and c=6.1365(7) Å at 297 K. The β-phase has an orthorhombic cell with a=12.8190(5), b=8.2195(4), and c=6.1236(2) Å at 637 K. The apexes of the PS_4 tetrahedron are ordered in the same direction in the γ-phase, while in the β-phase, they are ordered in a zig-zag arrangement.

Li_3PS_4 has been synthesised (i) through the dissolution in *Tetrahydrofuran* (THF, C_4H_8O), $Li_3PS_4 \cdot 3THF$ (β-phase), [99,104] (ii) through conventional solid state synthesis (β- and α-phase), [102–104] and (iii) mechanical synthesis through ball-milling followed by heat treatment (γ-phase). [105–107]

Experimental

Reagent-grade Li_2S and P_2S_5 with a purity of ca. 99 % was obtained from Alfa Aesar. The solid electrolyte with natural abundance of 7Li and 6Li (92.5 % : 7.5 %) glass was prepared from the micro-crystalline source material by ball-milling in a molar ratio of 3:1 using a high-energy planetary mill (Fritsch, Pulverisette 7). We used grinding beakers made of zirconium dioxide (Fritsch) that were equipped with 171 milling balls (ZrO_2, 5 mm in diameter). The air-tight beakers were filled and unfilled in inert gas atmosphere with less than 0.5 ppm water vapour content to avoid any contact of the ball-milled samples with air or moisture. To obtain different nano-crystalline samples the milling time was set to 36 h; the rotational speed of the mill was set to 380 rpm in order to reduce the formation of side products as effectively as possible. The so obtained powder was filled into glass tubes in inert gas atmosphere. The glass tubes were inserted in a temperature controlled tube oven for heat treatment between 180 and 360 °C.

For structural characterisation X-ray powder diffraction patterns were recorded on a Bruker D8 Advance diffractometer with Bragg Brentano geometry using Cu Kα radiation (10 to 100 $^\circ 2\theta$, step size 0.02 $^\circ 2\theta$, and step time 1 s). Rietveld refinement was carried out with an X'Pert HighScore Plus software package (PANalytical).

Temperature-variable and frequency-dependent ^{7}Li NMR measurements were carried out with an Advance III spectrometer (Bruker BioSpin) connected to a shimmed cryomagnet with a nominal magnetic field of 7 T; this field corresponds to a resonance frequency of $\omega_0/(2\pi)$ of 116.6 MHz. For temperatures ranging from 263 to 493 K, a commercial ceramic high-temperature probe (Bruker BioSpin) together with a Eurotherm temperature controller in connection with a type T thermocouple was employed. The accuracy of the temperature measurement was ± 2 K at the lowest T. Temperatures down to 155 K were measured with a cryoprobe cooled by liquid nitrogen. Here, the temperature was controlled by a LakeShore 331 cryogenic temperature controller using two Cernox thin film resistance cryogenic temperature sensors, one placed in the cryostat and the second in the vicinity of the sample. The output power levels of both probes allowed $\omega/2$ pulse lengths of about 3 to 5 µs, respectively. Prior to the measurements, the samples were fire-sealed in evacuated glass NMR tubes of 5 mm diameter and ca. 3 cm length.

^{7}Li NMR SLR (spin-lattice relaxation) rates $1/T_1 = R_1$ were acquired with the saturation recovery pulse sequence $10 \cdot \pi/2 - t_d - \pi/2$-acquisition (acq.). An initial pulse train, consisting

of ten $\pi/2$ pulses was used to destroy any longitudinal magnetisation M_z prior to recording its temperature and frequency dependent recovery as a function of the delay time t_d. Rotating-frame ^{7}Li NMR SLRρ rates $1/T_{1\rho} = R_{1\rho}$ were recorded with the spin-lock technique, $\pi/(2p(t_{lock}))$-acq. The corresponding (angular) locking frequency ω_1 was chosen to be as low as possible. Here, $\omega_1/(2\pi) \approx 25$ kHz was used and the duration of the locking pulse t_{lock} was varied from 22 µs to 300 ms. Note that the cycling delay for the SLRρ experiments was set to at least $5 \cdot 1/R_1$ in order to guarantee full longitudinal relaxation between each scan. Both R_1 and $R_{1\rho}$ were obtained by parametrising the magnetic transients $M_z(t_d)$ and $M_\rho(t_{lock})$, respectively, by stretched exponentials (see below): $M_z(t_d) \propto 1 - \exp[-(t/T_1)^\gamma]$ and $M_\rho(t_{lock}) \propto \exp[-(t_{lock}/T_{1\rho})^{\gamma\rho}]$, respectively.

For our broadband impedance measurements the powders were cold-pressed into dense tablets by means of a 10 mm press set in combination with a P.O.-Weber hand press that allows a uni-axial force of 10 kN. Au electrodes of about 100 nm thickness were applied by vaporisation in an inert gas atmosphere. Temperature-variable 2-electrode impedance measurements were carried out with a Novocontrol Concept 80 broadband analyser (Alpha-AN, Novocontrol) that is used in combination with a BDS 1200 cell and an active ZGS cell interface. The temperature in the sample chamber is automatically controlled with an accuracy of ± 0.01 K by a QUATRO cyrosystem (Novocontrol) using a constant flow of freshly evaporated nitrogen gas that is heated up. The set-up is able to record impedances and permittivities at frequencies ranging from few mHz up to 20 MHz (150 K to 570 K).

Cyclic voltammetry (CV) was done with a Biologic potentiostat (VMP3) at 120 °C. Au electrodes of about 100 nm thickness were applied by vaporisation in an inert gas atmosphere for symmetric CV. The so prepared air sensitive pellets were packed in a Swagelok type T-fitting.

Results and Discussion

The originally micro-structured source material was prepared in a planetary mill at constant milling time. After milling for 36 h, a sample was analysed *via* differential scanning calorimetry (DSC), see Fig. 5.2. The heating rate was fixed at 10 K/min in constant He gas flow of 50 ml/min. Several exothermic and endothermic peaks are observed in the temperature range from 35 to 550 °C. The observed endothermic heat flow at 163.7 °C, combined with the observed *glass hill* in the X-ray powder diffraction patterns seen in Fig. 5.3 is interpreted as a glass formation process. [25,105] The two exothermic peaks at 237.9 °C and 258.8 °C indicate crystal formation processes. Thus, it was decided to do the heat treatment of the amorphous powder in the range between 180 and 360 °C.

In the observed halo X-ray powder diffraction pattern (see Fig. 5.3, '20 °C') only small reflections of the raw material Li_2S can be identified, [108] indicating that this sample became largely amorphous by mechanical milling for 36 h. Heat treatment for 17 h under inert gas atmosphere at 180 °C leads to glass formation, and at temperatures of 200 °C and above to recrystallisation. The X-ray powder diffraction pattern seen in Fig. 5.3 at 180 °C shows a typical *glass hill* [25] as indicator to glass formation. From 200 to 360 °C the characteristic

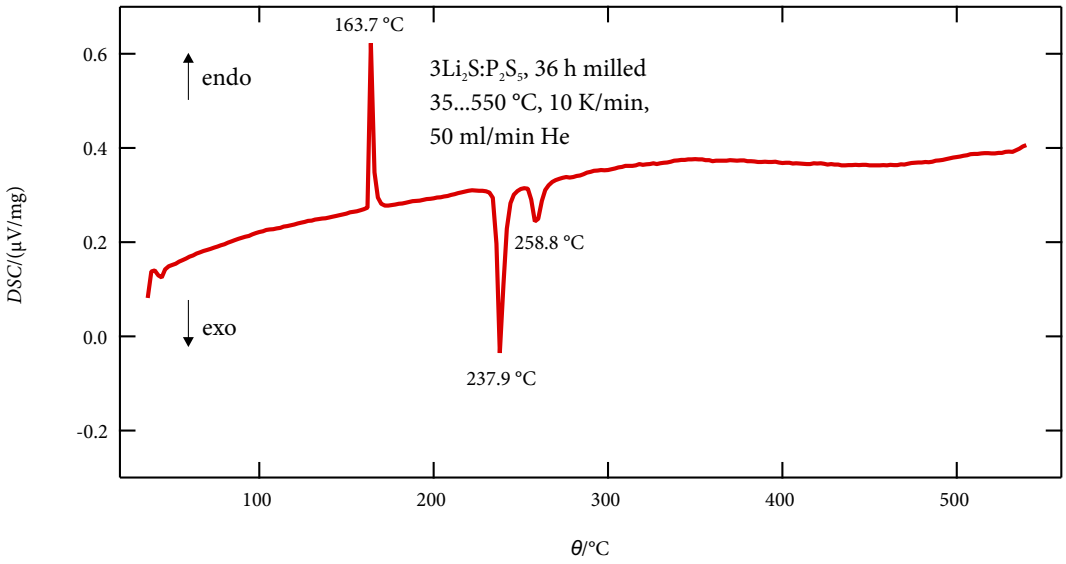

Figure 5.2: DSC pattern of 36 h milled $3Li_2S : P_2S_5$. The heating rate is fixed at 10 K/min and the atmosphere is maintained under He flow of 50 ml/min. Glass formation can be observed at 163.7 °C and crystal formation at 237.9 °C and 258.8 °C.

reflections for phase-pure γ-Li_3PS_4 emerge, as can be compared with the pattern from the database [96] (red vertical lines in Fig. 5.3).

The temperature selected for the heat treatment influences the level of recrystallisation, and so the conductivity. The corresponding conductivity isotherms are shown in Fig. 5.4 for the amorphous (a) and the crystalline (b) sample; they reveal the typical characteristics for structurally disordered materials. The frequency dependent conductivity spectra, which are composed of a direct current (DC) plateau and a Jonscher type dispersive region, can be approximated by a power law:

$$\sigma' = \sigma_{\mathrm{dc}} + A_\sigma \omega^n \,, \tag{5.1}$$

where σ_{dc} corresponds to the conductivity plateau and n is the Jonscher exponent; here n takes values of 0.84 for the amorphous $3Li_2S : P_2S_5$ and 0.50 for the crystalline γ-Li_3PS_4 sample at 293 K. This range is in good agreement with the results found in many previous studies on disordered materials and glasses; in particular, see the studies focusing on nano-crystalline $LiTaO_3$ [109] and amorphous $LiNbO_3$. [110–113] The decrease of σ' at low frequencies and sufficiently high temperatures, that is, above 450 K and at frequencies $\omega/(2\pi) < 100$ Hz, is due to polarisation effects because of the ion-blocking electrodes used.

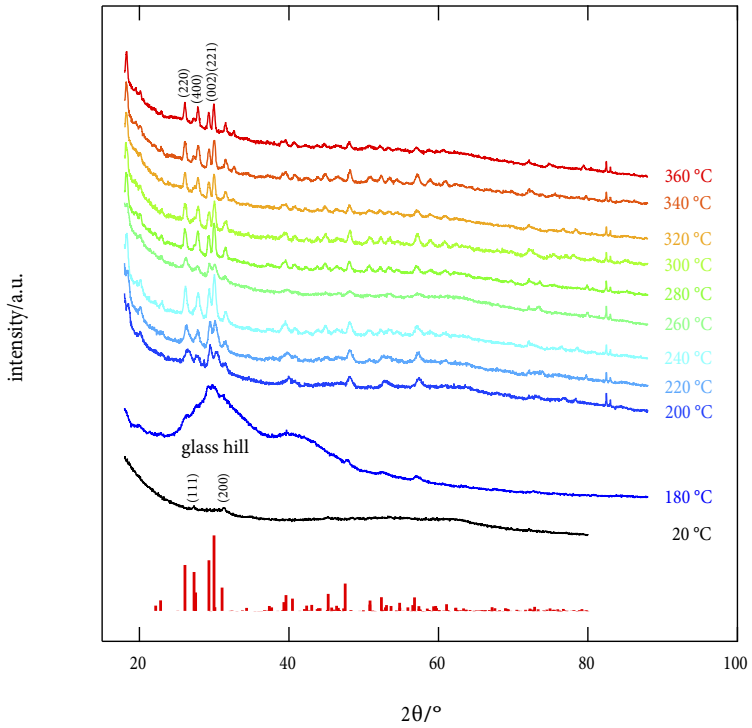

Figure 5.3: XRD patterns of the $3Li_2S : P_2S_5$ samples mechanically milled for 36 h and heat treated for 17 h. The reflections of the originally visible raw material (Li_2S) in the not annealed sample (20 °C) are covered by a *glass hill* [25] hinting to glass formation at 180 °C and vanish completely after forming phase-pure γ-Li_3PS_4 at higher temperatures. Vertical lines show reflections from database, [96] Miller indices in brackets. [96, 108]

To quantify thermal activation of the *long-range* ion transport, to which σ_{dc} is sensitive, the DC conductivity values ($\sigma_{dc}T$) have been plotted versus $1000/T$, see Fig. 5.5. Solid lines represent fits according to an Arrhenius law:

$$\sigma_{dc}T \propto \exp(-E_a/(k_B T)), \tag{5.2}$$

where k_B is Boltzmann's constant. Starting from $E_a = 0.40$ eV for the non-treated sample, the activation energy increases to 0.44 eV for the glass sample after annealing at 180 °C for 17 h. The crystalline powder annealed at 260 °C approaches almost the conductivity of the amorphous nano-structured source material. If the pellet pressed from the phase-pure γ-Li_3PS_4 is exposed again to high temperatures, the conductivity decreases again by several decades and the activation energy increases to 0.78 eV, see Fig. 5.5, '260 °C powder & pellet'. Although the DC-conductivity is similar, amorphous and crystalline material show a different

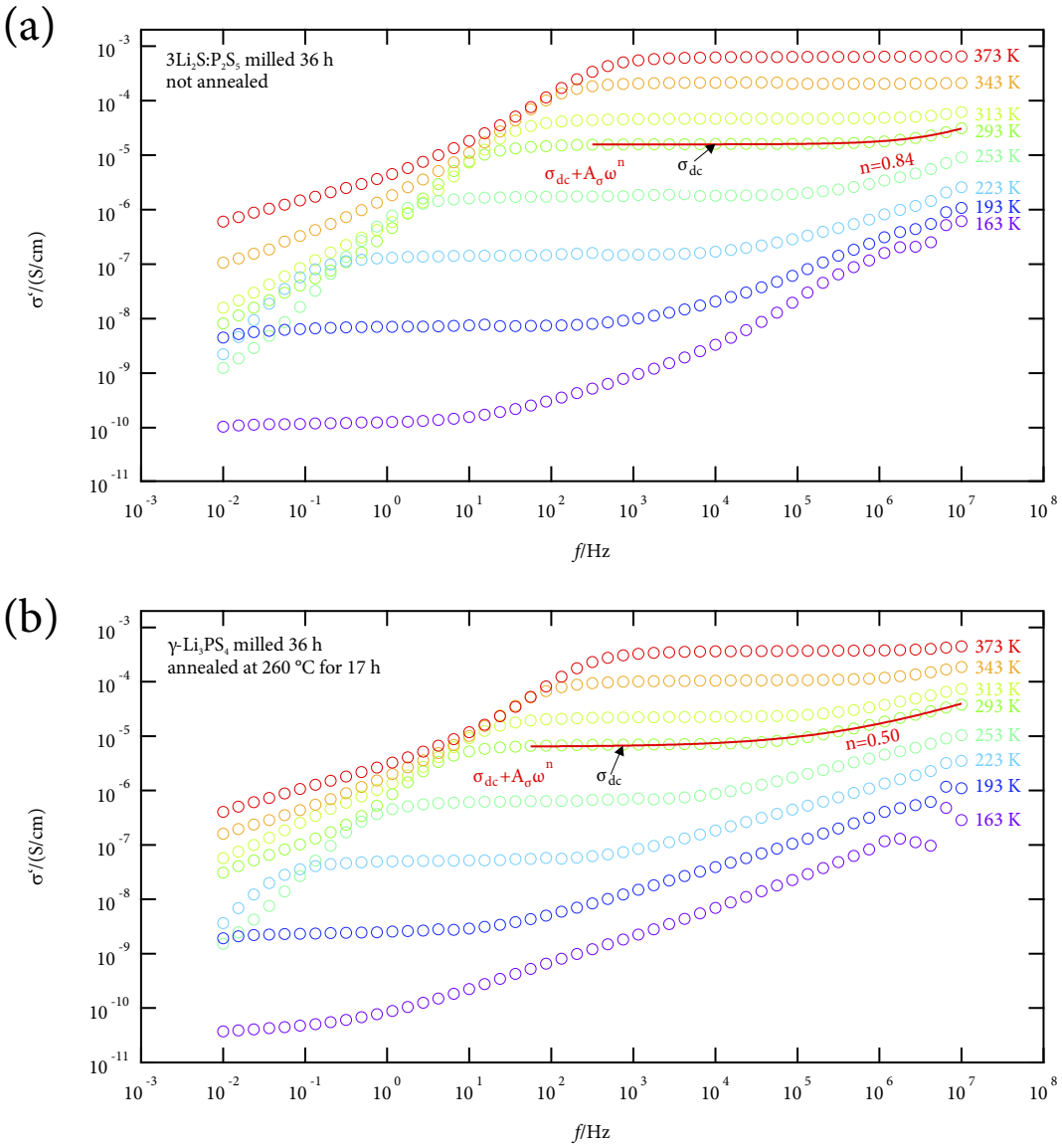

Figure 5.4: Conductivity spectra of (a) amorphous $3Li_2S : P_2S_5$ and (b) crystalline γ-Li_3PS_4 measured in an airtight sample holder loaded in Ar atmosphere. While the samples show similar DC-conductivities at lower frequencies, the dispersion at higher frequencies is different. Solid lines represent fits with an appropriate power law containing the Jonscher exponent n.

relative bulk-permittivity $\varepsilon(0)$, see Fig. 5.6, which is a further indicator for a phase transition taking place during annealing.

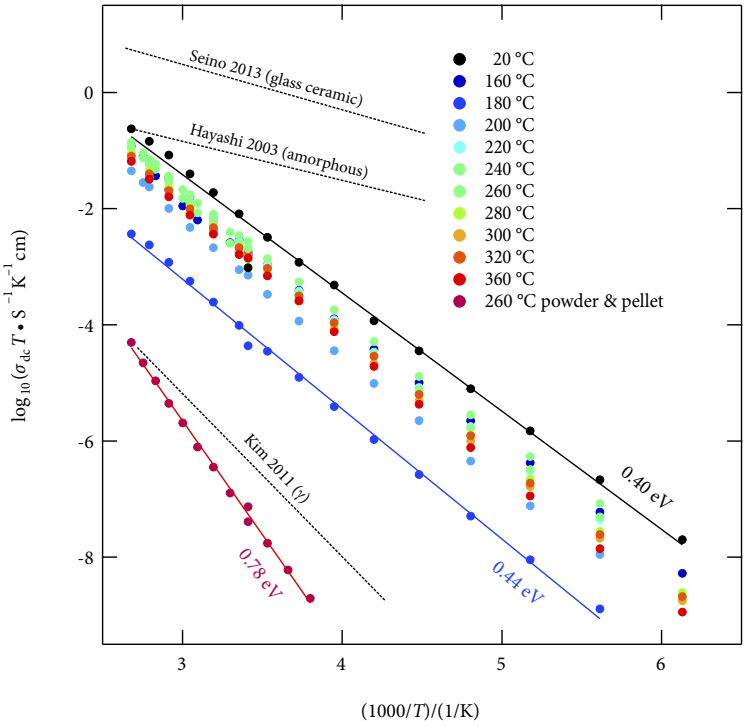

Figure 5.5: Arrhenius plot showing the temperature dependence of the conductivity of the $3Li_2S : P_2S_5$ samples. γ-Li_3PS_4 annealed at 260 °C shows the highest conductivity among the crystalline samples, but cannot keep up with the amorphous sample. Dashed lines represent literature data for γ-Li_3PS_4, [106] amorphous $4Li_2S : P_2S_5$ [105] and $7Li_2S : 3P_2S_5$ glass ceramic made by solid state synthesis at 700 °C. [107]

Fig. 5.7 shows the symmetric cyclic voltammogram (a) and the EIS spectrum (b) before and after the first CV-cycle in Nyquist representation of the crystalline γ-Li_3PS_4 cell. The potential of the working electrode E_{WE} was swept between -5 and +5 V vs. Au and the scan rate was 1 mV/s. The temperature was maintained at 120 °C. During the the first CV-cycle, a broad irreversible current domain emerges at 5 V. However, no nucleation loop is visible. It is very likely that Li metal formation takes place. The Li metal may react with the electrodes to a solid electrolyte interphase (SEI). An increase in resistance ($\Delta Z'$ in Fig. 5.7 (b)) can be observed after the first CV-cycle that might be ascribed to SEI formation. The following CV-cycles do not show significant current peaks due to the electrolyte decomposition or phase change, suggesting the samples remain electrochemically stable under the test conditions.

The NMR line shape measurements seen in Fig. 5.8 reveal motional narrowing with increasing T regime of extreme narrowing already reached at ca. 250 K, the jump rate is in the order of $10^4 ... 10^5$ s^{-1}.

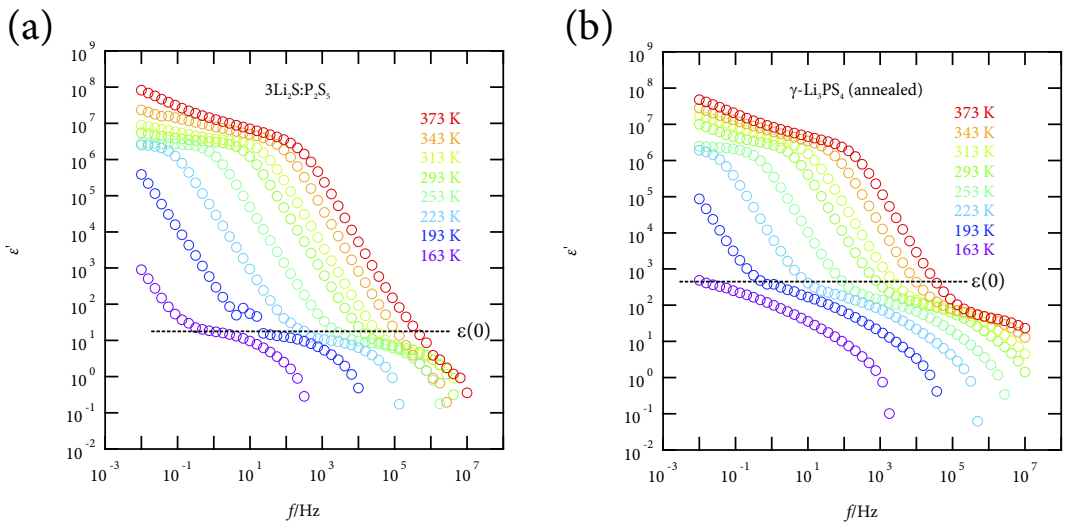

Figure 5.6: Permittivity spectra of (a) amorphous $3Li_2S : P_2S_5$ and (b) crystalline γ-Li_3PS_4.

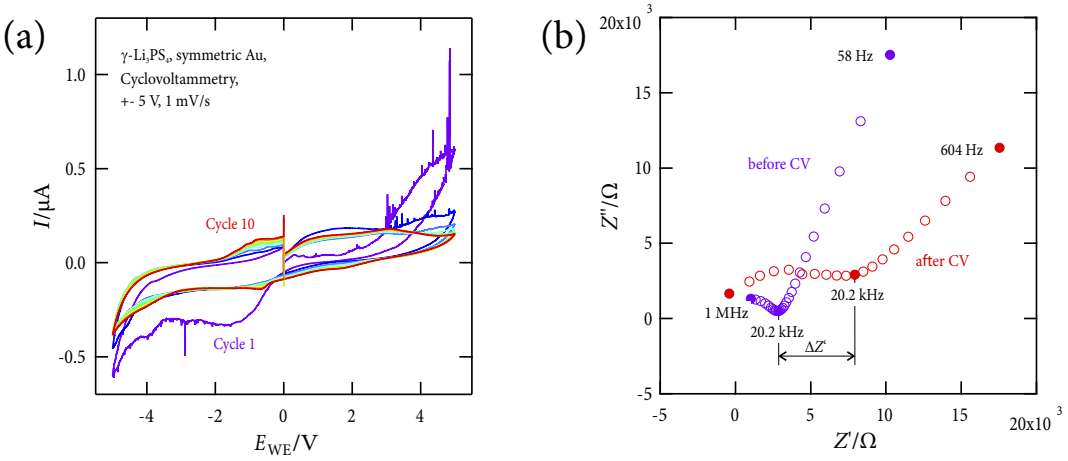

Figure 5.7: Cyclic voltammogram (a) and EIS spectrum (b) of the symmetric crystalline γ-Li_3PS_4 cell at 120 °C.

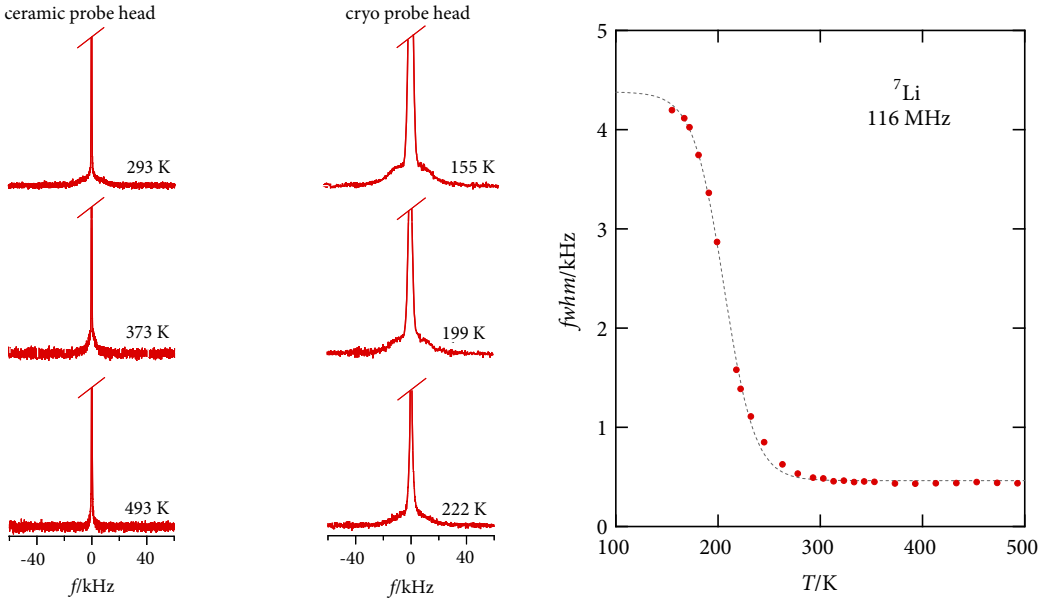

Figure 5.8: Line shape measurements: NMR lines reveal motional narrowing with increasing T regime of extreme narrowing already reached at ca. 250 K, jump rate in the order of 10^4...10^5 s^{-1}.

NMR spin-lattice relaxation (Fig. 5.9) provides insights into both *short-range* Li^+ hopping and and *long-range* Li^+ diffusion. The activation energies E_a of 0.19(3) eV and 0.08(7) eV characterise local Li-ion motions. The diffusion-induced $R_{1\rho}$ maximum can be found at T_{max} = 245 K. The Li-ion jump rate is determined with ca. $1.5 \cdot 10^5 s^{-1}$ at T_{max}. The activation energy of the long-range ion diffusion is 0.37 eV as deduced from low-T flank of $R_{1\rho}(1/T)$.

Conclusions

The present findings show that phase-pure γ-Li_3PS_4 can by synthesised mechanically from originally micro-structured $3Li_2S : P_2S_5$. Compared to data from the literature, the prepared sample pertains the highest ionic conductivity ever observed among crystalline Li_3PS_4. The results obtained *via* cyclic voltammetry show that γ-Li_3PS_4 is sufficiently electrochemically stable to be applied in solid-state Li-ion batteries. Compared to other solid state ion conductors, Li_3PS_4 is moderate. A low E_a can be derived from σ_{dc}. The NMR experiments show fast local jump movements that do not necessarily cause a high σ_{dc} and a low E_a of the ionic transport on longer time scales. A superposition of different diffusion processes is visible: a broad $T_{1\rho}$ peak with abnormal high temperature edge and at least two T_1-processes with E_a = 0.09 eV and 0.2 eV.

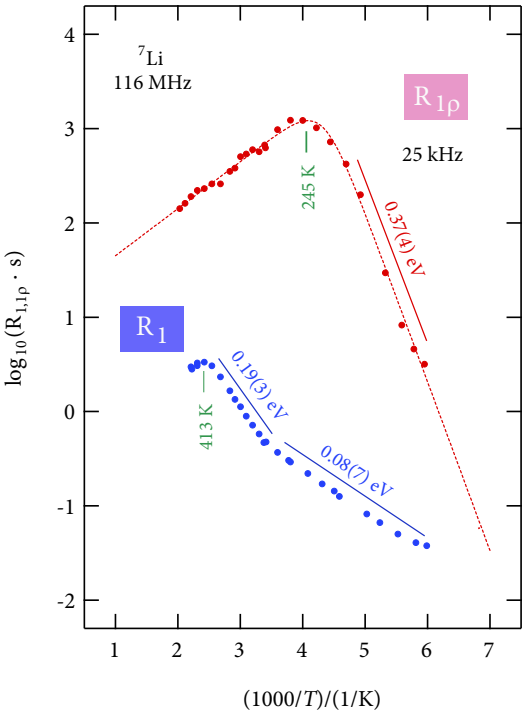

Figure 5.9: NMR spin-lattice relaxation provides insights into both short-range Li+ hopping and and long-range Li+ diffusion. E_a of 0.19(3) eV and 0.08(7) eV characterise local Li-ion motions. Diffusion-induced $R_{1\rho}$ maximum at T_{max} = 245 K. Li-ion jump rate: ca. $1.5 \cdot 10^5 s^{-1}$ at T_{max}. Long-range ion diffusion: 0.37 eV as deduced from low-T flank of $R_{1\rho}(1/T)$.

Summary

Phase-pure γ-Li_3PS_4 was synthesised mechanically through ball-milling followed by heat treatment. The so prepared powder samples were analysed *via* X-Ray crystallography and NMR techniques. The powders were cold-pressed into tablets. Au electrodes were applied by vaporisation in an inert gas atmosphere. The pellets were analysed *via* impedance spectroscopy and cyclic voltammetry. The conductivity spectra show that the mechanically synthesised γ-Li_3PS_4-sample pertains higher conductivity compared to the values known from the literature, but cannot keep up with amorphous material. The cyclic voltammogram shows that the electrolyte remains stable within a voltage range between -5 and +5 V, although there are indications that an SEI is probably forming at the interface electrode–electrolyte. Thus the solid electrolyte studied may be in fact kinetically stable rather than thermodynamically stable.

5.3 Liquid Electrolytes

5.3.1 Myth and Reality about the Origin of Inductive Loops in Impedance Spectra of Lithium-Ion Electrodes — A Critical Experimental Approach (Paper 2)

Brandstätter H., Hanzu I., and Wilkening M. *Electrochimica acta* **207**, 218–223 (2016).—This article is reproduced by permission of Elsevier B.V. The original article can be found online at http://dx.doi.org/10.1016/j.electacta.2016.03.126.

Electrochimica Acta 207 (2016) 218–223

Contents lists available at ScienceDirect

Electrochimica Acta

journal homepage: www.elsevier.com/locate/electacta

Myth and Reality about the Origin of Inductive Loops in Impedance Spectra of Lithium-Ion Electrodes — A Critical Experimental Approach

Harald Brandstätter, Ilie Hanzu, Martin Wilkening*

Graz University of Technology (NAWI Graz), Institute for Chemistry and Technology of Materials, and Christian Doppler Laboratory for Lithium Batteries, Stremayrgasse 9, A-8010 Graz, Austria

ARTICLE INFO

Article history:
Received 25 February 2016
Accepted 22 March 2016
Available online 3 May 2016

Keywords:
Impedance spectroscopy
Lithium-ion batteries
Inductive loops
Negative capacitance effect

ABSTRACT

Electrochemical Impedance Spectroscopy (EIS) is a sophisticated analyzing tool in battery research. Though, there are still phenomena subject to speculation. As an example, for a long time the formation of the so-called Solid Electrolyte Interphase (SEI) has been made responsible for inductive loop formation in impedance spectra. In our opinion, there are, however, no satisfying evidences supporting this attempt to explain the occurrence of inductive loops. The present study is, thus, aimed at answering the question whether other origins such as cell design ought to be considered to reveal the electrical sources for this phenomenon. Therefore, two commonly used anode materials for lithium-ion batteries were investigated with respect to their tendency to the formation of SEIs. Besides the influence of the SEI on the overall impedance response, also the impact of the cell design on electrical response was investigated. We identified four different sources of (i) *inductive* and (ii) *negative capacitance* loop formation: springs, reference electrodes, drift, and corrosion. In conclusion, any interrelationship between inductive loops and SEI formation could be ruled out. This finding disproves an earlier, commonly known attempt that traced the presence of inductive loops back to the formation of passivating surface layers because of electrolyte decomposition.

1. Introduction

The development of advanced electrochemical energy storage systems, which are based on Li ions as charge carriers, is more important today than at any time before [1]. Depending on the active materials chosen, the design of Li-ion batteries may require the formation of passivating films or interphases on those electrodes that operate outside a certain electrochemical potential window. These passive layers are known to be lithium-ion conductors while being electronic insulators. Because of their electronically insulating nature the growth of the film may, in favorable conditions, become a self-limiting process. This means the growth rate of the film is expected to significantly reduce during battery operation, thus, avoiding further electrolyte degradation at the electrodes.

Both positive and negative electrodes are known to form passive films, although the interphases are different in composition and relative stability. The passivating layers at the negative electrode – note that graphite is the most common negative electrode material – are better defined and more stable than those that build up at the positive electrodes. This Solid Electrolyte Interphase (SEI) has been made responsible for the appearance of significant inductive loops in Electrochemical Impedance Spectroscopy (EIS) [2]. The present paper is aimed at revisiting the question whether SEI formation is indeed responsible for inductive loop behavior as seen many times in impedance spectroscopy on lithium-ion cells. Exemplarily, inductive loops were found in EIS studies by Zhuang *et al.*; the authors investigated positive electrode materials such as layered $LiCoO_2$ (LCO) [3] and spinel-type $LiMn_2O_4$ [3].

An inductance is defined as the property of an electric circuit to cause an electromotive force as a result of a change in the current passing through the circuit itself. Gnanaraj *et al.* [4] suggested that inductive loop formation might be explained by the formation of an electromotive force superimposing the process of lithium ion extraction. In the case of layer-structured LCO spatially isolated Li-rich and Li-poor, *i.e.*, Li-deficient, regions may be formed during extraction of the Li ions. Isolation of Li-rich and Li-poor regions in the electrode may, however, also be created by the SEI film due to disequilibrium with respect to electronic continuity. Hence, a concentration cell would be established between the Li-rich domains and the Li-poor regions ($Li_{1-x}CoO_2$, $0 < x < 0.5$) separated by the SEI film. Because the SEI film is imperfect at the early stages

* Corresponding author.
E-mail address: wilkening@tugraz.at (M. Wilkening).

http://dx.doi.org/10.1016/j.electacta.2016.03.126
0013-4686/

of delithiation of LCO, a current may flow within the concentration cell. This current would generate a field in opposite direction to the field corresponding to lithium ion extraction. Considering the overall discharging and charging processes of an electrode, such a situation would, indeed, provide the requirements for the formation of an inductive loop, as it is explained by the commonly proposed theory. The question arises whether we could really trace back the inductive loop behavior to such local phenomena inside the electrodes. Alternatively, geometric effects, wiring or cell configurations, *i.e.*, macroscopic origins, may serve as much simpler explanations. To our knowledge, a systematic study envisaging these origins through EIS and different cell configurations is, however, still missing.

It has to be noticed from the beginning that electromotive forces generated in the way described above always run from a negative to a positive charge and are, therefore, *curl-free*. The existence of electric curls or a time-variant magnetic flux is the essential criterion of induction [5]. In electric fields without induction there are no closed field lines and, thus, the circulation of the electric field strength is always zero, see equation (1):

$$V_{\mathrm{ind}} = \oint_C \vec{E} \cdot d\vec{r} \stackrel{!}{=} 0, \tag{1}$$

where V_{ind} is the voltage induced, $\vec{E}$ denotes the electric field strength and $\vec{r}$ the path. Expressed in a simpler way, an inductance L necessarily implies the existence of a magnetic energy storage [6,7].

Interestingly, Hyung-Man Cho *et al.* [8] observed the emergence of an inductance in their semi-empirical equivalent circuit model developed for aged LCO cells but the origin of this feature has yet to be determined. While the influence of cell geometry has been well studied for solid electrolytes and fuel cells, little of this knowledge has been used to explain similar effects in lithium-ion batteries [9]. Swagelok-type cells are rather unreliable for EIS for several reasons. For example, the fact that several equipotential surfaces are probed at once by the reference electrode makes a reliable interpretation difficult. Moreover, unintended electrode misalignments are likely that also complicate the explanation of results from impedance data recorded on Swagelok-type cells. As a result, a strong scaling effect of the high frequency semi-circle and even a second capacitive loop superimposed on the medium frequencies may be observed. Langklotz and coworkers [10] are currently investigating the inductive loop issue by impedance spectroscopy using LCO and $LiFePO_4$ test cells. They observed an influence of cell design to the measurement result without having identified the origin yet [10]. Our present investigations with LTO and graphite cells are intended to finally shed some more light onto these, in our opinion, *hitherto* unexplained issues.

To study the origins of inductive loop formation in EIS in detail we prepared several lithium-ion half cells with different geometry, electrode configuration and two negative electrode materials that largely differ in SEI formation. While graphite is known to form extended passivation layers because of its low electrochemical stability in Li-based cells with common liquid electrolytes, lithium titanate, $Li_4Ti_5O_{12}$, on the other hand, is characterized by an operating potential well above that of metallic lithium, see., *e.g.*, ref. [11]. The high potential prevents the formation of an SEI [12–19]. The cells were prepared as follows.

2. Experimental

Lithium titanate with a purity of ca. 99 % was obtained from Sigma Aldrich. The grain size of the non-treated raw material was in the μm range and reveals the typical X-ray powder diffraction pattern of spinel-type $Li_4Ti_5O_{12}$. In order to prepare dense electrodes we used ball milling to form an active material that is easily to handle. Nanocrystalline $Li_4Ti_5O_{12}$ was prepared from the microcrystalline source material by ball milling using a high-energy planetary mill (Fritsch, Pulverisette 7). We used grinding beakers made of zirconium dioxide (Fritsch) that were equipped with 180 milling balls (ZrO_2, 5 mm in diameter). The air-tight beakers were filled and unfilled in inert gas atmosphere with less than 0.5 ppm water vapor content to avoid any contact of the samples with air or moisture. To prepare the nano-samples the material was milled for 2 h; the rotational speed of the mill was set to 400 rpm in order to reduce the formation of side products as effectively as possible.

For the preparation of the LTO-based electrode, nano-$Li_4Ti_5O_{12}$ was mixed with conductive carbon particulate matter (Super C 65), binder (Kynar 761); N-methyl-2-pyrrolidone served as solvent. After stirring for several hours the viscous slurry was cast (Dr. Blade method, 100 μm casting gap) onto a thin copper foil and dried in an oven. Electrode disks, 10 mm in diameter, were punched out and, when necessary, further cut for cross-section SEM observations. For the graphite electrodes the raw material was directly mixed in the slurry without the ball-milling step carried out in advance.

The so prepared electrodes were used to assemble 2-electrode and 3-electrode lithium-ion half cells. A glass fiber separator was soaked with $LiPF_6$ (1M) in EC:DMC (1:1 molar ratio); it served as ion-conductor between the working electrodes and the counter electrode (Li metal). For the 3-electrode cells an additional Li-reference electrode was installed. Galvanostatic cycling with potential limitation combined with EIS was carried out with a Biologic potentiostat (VMP3) at room temperature; frequencies ranged from 1 mHz to 1 MHz. The 3-electrode Li-ion half cells were placed in a 1/2-inch T-tube fitting from Swagelok. The 2-electrode half cells were packed in a specially designed low-inductance electrochemical cell, which consists of an electrically insulating plastic without metallic springs and screws.

3. Results

To investigate the influence of the SEI to the electrical impedance response of a lithium ion half cell, two different anode materials were selected: graphite and $Li_4Ti_5O_{12}$ (LTO). While graphite is well known for its SEI growing properties during battery aging LTO is famous to be a long-life intercalation material [12–19]. In contrast to graphite, no, or at least negligible, SEI films are formed at LTO surfaces as it shows a relatively high operating potential (1.55 V) against Li metal [11].

For the aging measurement 3-electrode cells with working electrodes of graphite and $Li_4Ti_5O_{12}$ were assembled as described in section 2. During the cycling process several impedance spectra (shown in Fig. 1 using the complex plane plot, that is, the Nyquist representation) were recorded at different states of aging. In a Nyquist plot the imaginary part ($-Z''$) of the complex impedance $\underset{\sim}{Z}$ is plotted vs the real part (Z').

While the fresh graphite cell features a high initial capacity than the one made with LTO, its reversible capacity plunges within a low number of charge-discharge cycles. On the other hand, the LTO structure, although starting at a lower reversible capacity level, seems to remain stable over more than 1000 cycles and hardly loses any capacity. This is usually related to the formation of significant passivation films on graphite that continue to grow and evolve in time. In contrast, LTO, which unlike graphite is a zero-strain material, forms virtually no SEI. Although some passivating films were reported on LTO, they were ascribed mostly to oxidation products diffusing from the positive electrodes [20].

Fig. 1 shows the impedance spectra recorded for the charged and discharged electrodes during cycle aging. In both cases inductive loops appear – independent of the anode material used and the aging status of the cell. To have final certainty about the influence

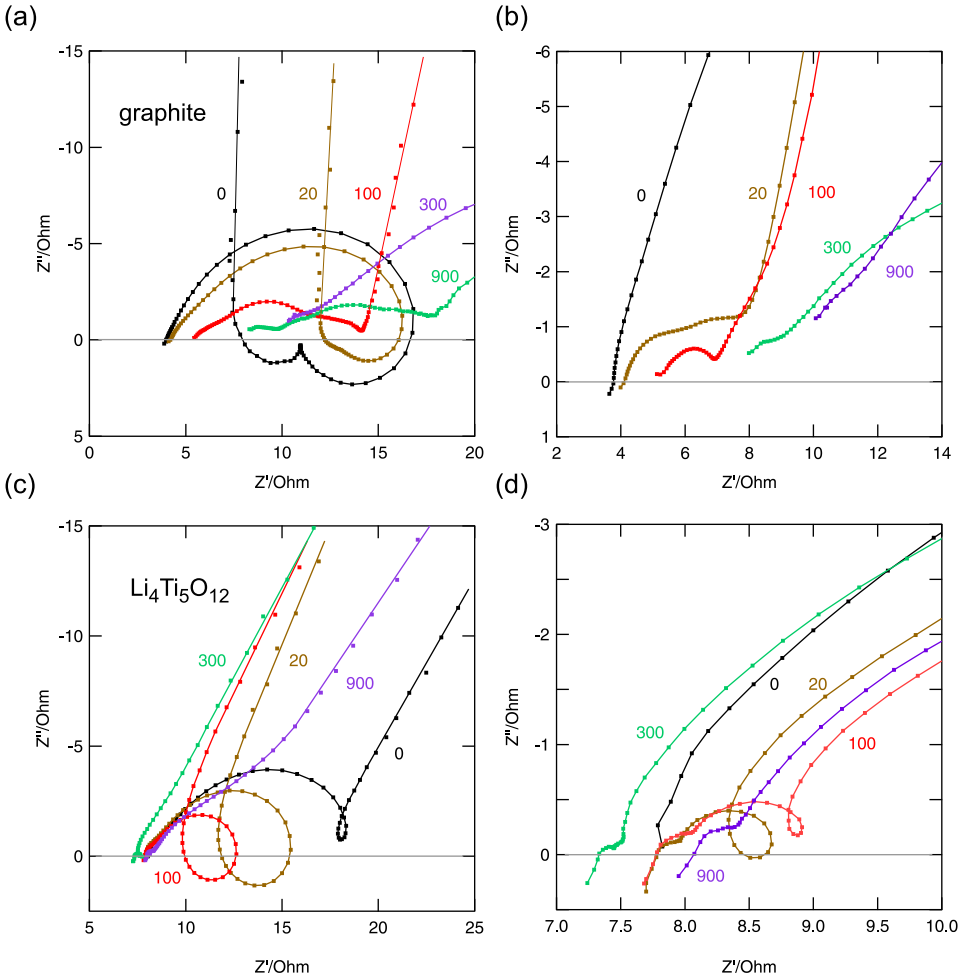

Fig. 1. Nyquist plots of impedance data ($-Z''$ vs Z') recorded on lithium-ion half cells with either graphite [(a) charged and (b) discharged state] or LTO [(c) charged and (d) discharged state] serving as anode materials; the numbers indicate the charge-discharge cycles after which the spectra were recorded. The lines drawn are guides to the eye. See text for further explanation.

of SEI formation on inductive loop formation, after the cycling procedure we disassembled the cells and recorded scanning electron microscopy (SEM) images to study cross sections of the electrodes. Fig. 2 (a) and (b) show the cross sections of the LTO electrodes

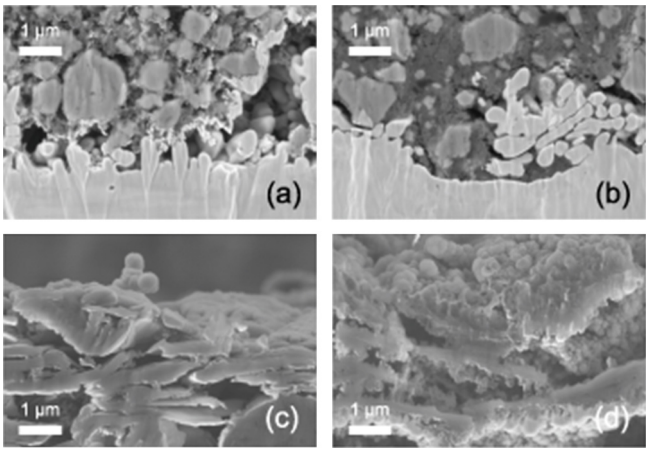

Fig. 2. SEM images of slope cuts of the fresh and aged LTO [(a) and (b)] as well as graphite electrodes [(b) and (c)]. In the case of graphite significant SEI formation is seen due to electrolyte decomposition. This behavior was assumed to be responsible for the emergence of inductive loops in impedance spectra of lithium-ion cells.

before and after cycling. Neither the fresh nor the aged electrode shows any visible alteration, *i.e.*, passivation layers formed on the surface. On the surface of the graphite-based electrodes, however, a thick SEI layer has formed after the cell was charged and discharged for 1300 times, see the deposits visible in Fig. 2 (d) owing to electrolyte decomposition. Degradation occurs as the graphite electrode works outside the electrochemical stability window of the liquid electrolyte.

In order to narrow down our search for the origins of the inductive loops observed, we repeated the experiment with graphite electrodes with the specially designed half cell that is described in section 2. Most importantly, this cell does not contain any spring or reference electrode. As can be clearly seen from Fig. 3, which displays the corresponding Nyquist curves recorded, no inductive loops show up. The experiment was carried out with graphite deliberately to ensure a significant SEI formation. Although heavy SEI formation takes place, the Nyquist diagrams recorded with the 2-electrode cells look like textbook examples [6]. The SEI formation on graphite manifests as an increasing ohmic series resistor rather than as an inductive loop formation. Both the charge-transfer resistance as well as that related to the passivating SEI significantly depend on cycling; the results are entirely consistent with those presented in literature [21]. Such data can be used to develop an electrochemistry-based impedance model to predict battery performance and aging as has been shown by, *e.g.*, Li *et al.* recently [21].

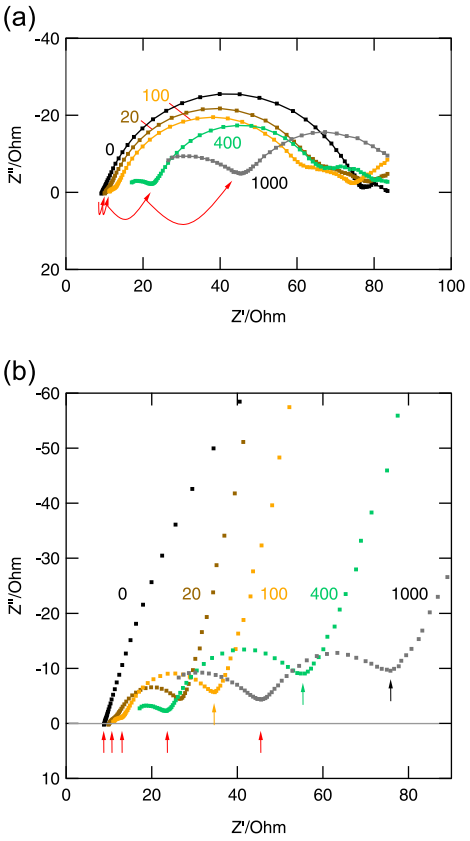

Fig. 3. Nyquist diagrams (imaginary part ($-Z''$) of complex impedance vs the real part (Z')) of charged (a) and discharged (b) lithium-ion 2-electrode half cells with graphite as anode material. The numbers indicate the charge-discharge cycles. Resistances, corresponding to interfacial charge-transfer (combined with double-layer capacitances) and SEI film, steadily increase with cycle number, *i.e.*, with SEI formation and progressing aging. The lines in (a) are to guide the eye.

The fact that inductive loops are completely absent in the case with the 2-electrode setup already hints at the assumption that configurational aspects such as wiring, springs and reference electrodes might be responsible for inductive effects. In order to proof this guess, we investigated the electrical response of Swagelok cells without the spring usually inserted. It is used to press the counter electrode against the working electrode.

As shown in Fig. 4, during the first 20 cycles the inductive part of the complex impedance is much lower than compared to the results in Fig. 1. To scrutinize the effect of any springs, usually several of them are used in Swagelok-type cells, an empty cell with a spring, connected to the unit under test in series, was examined. The impedance spectra recorded after 100 cycles show a significant increase in inductance on the high-frequency semi-circle. Finally, the spring was removed again and the reference electrode was unused, thus reverting to a 2-electrode configuration. This procedure resulted in an increase of ohmic resistance; most importantly, the inductive part vanished completely as can be seen if we consider the impedance spectra recorded after 200 and 300 cycles, respectively.

Interestingly, the spectra presented in Figs. 1 and 4 show two other loop formations. There is a small loop in the medium frequency range that does not reach the inductive complex plane (Fig. 4 (c), see magnification shown on the right). It vanishes after a few cycles and can be addressed to drift because of a cell being electrochemically still unstable. In our opinion, it cannot be explained via a second concentration cell as assumed by Zhuang *et al.* [2] for a $Li/LiMn_2O_4$ cell system. The other loop appears in the low-frequency semi-circle of a fresh, *i.e.*, uncycled, charged Swagelok cell with graphite electrode, see Figs. 1 (a) and 4 (c), respectively. We suspect pitting corrosion [6,22] to be the source of this loop. At first glance, the loop appears to be *inductive* in nature; its frequency dependence is, however, contrariwise to an inductor.

To examine the behavior of this low frequency arc in more detail, another Swagelok cell with graphite electrodes was assembled. It was charged immediately after assembling, *i.e.*, without any relaxing step prior to cycling. Fig. 5 shows the resulting impedance response of this cell. The Nyquist diagram is quite similar to the one in Fig. 4 (c). After giving the cell a rest for three days another impedance spectrum was recorded. Now it perfectly fits to the pitting corrosion loops known from literature [6,22]. One data point of the low-frequency loop was picked out and its impedance response was watched in time domain using a digital storage scope connected to the voltage and current monitor outputs of the potentiostat. After filtering out the background noise in the high resolution mode, the data recorded in time domain reveals the true shape of the current response. The phase shift between voltage and current at zero-crossing is zero, but the non-linear distortion of the current response might lead to a positive phase shift. It is very likely that we observed the so-called *negative capacitance effect* that is discussed in the next section.

On the search for the corroding part of the Swagelok cell, we finally disconnected the reference electrode before recording another impedance spectra. The low frequency semi-circle with a positive imaginary behavior vanished again as can be seen in Fig. 5.

4. Discussion

SEI film growth is a major source of battery degradation. The film growth increases internal resistance and reduces lithium-ion transport, which leads to both capacity fading and capability degradation. This aging effect represents an irreversible process, especially at the anode side [23,24]. In general, the growth in film resistance can be a measure to predict capacity fade and power capability loss of lithium-ion batteries [21].

In contrast to previous studies, see, *e.g.*, refs. [2,4], our experiments revealed that SEI formation cannot be considered as the origin of inductive loop formation in lithium-ion cells. When using 3-electrode Swagelok cells inductive loops appear in impedance spectra regardless if an SEI-forming material is investigated or an SEI-free one. LTO and graphite electrodes have been cycled for more than 1000 times to ensure a significant cycling age and electron microscope images give evidence of a consistent SEI-formation.

The origin of the inductive loops in the high-frequency range seems to be rather a constructive issue than an electrochemical phenomenon. The widely used Swagelok T-cells contain several metal parts, including helicoidal compression springs and cylindrical stainless-steel contacts. These contacting parts are effectively forming coils with steel cores. The inductance L of a long and slim coil can be estimated by

$$L = \frac{\mu_0 \mu_r N^2 A}{l}, \tag{2}$$

with the permeability of the vacuum μ_0, the relative magnetic permeability μ_r of the core material, the number of turns N, the cross section area A and the length l. Typical values for coils used are $l = 0.01$ m, $A = 4 \cdot 10^{-5}$ m^2, $\mu_r = 5000$, $N = 7$. Inserting this coil as a spring leads to an inductance in the mH range. The corresponding reactance X_L of such a coil is given by

$$X_L = j\omega L, \tag{3}$$

with the imaginary unit j and the angular frequency ω. Inserting typical values of L leads to X_Ls of several Ω at 100 Hz. 1 to 3 springs are typically used in one cell. Langklotz and coworkers [10] already

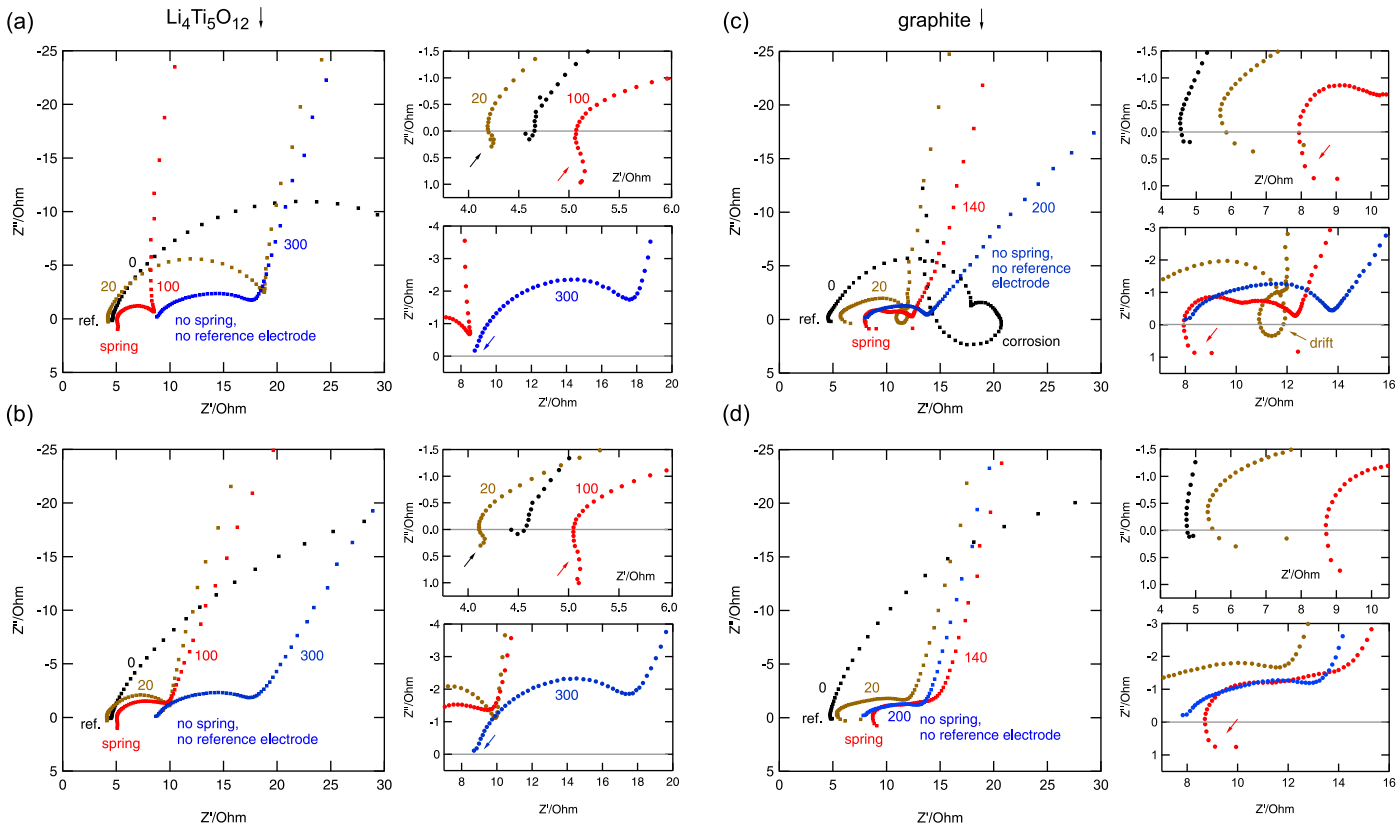

Fig. 4. Nyquist diagrams of a series of discharged and charged lithium-ion half cells with either LTO [(a) and (b)] and graphite [(a) and (b)] anodes. Numbers indicate the charge-discharge cycles carried out. Inductive loops can be switched on and off by adding and removing the spring and the reference electrode. The small figures to the right of each larger figure represent magnifications to highlight any positive Z'' values. See text for further details.

observed a difference in inductive behavior between 2-electrodes and 3-electrodes cells, without recognizing the different number of coils used. Another contribution in the high-frequency range originates from the reference electrode, as shown in section 3. This effect might be reduced by optimizing cell design and wiring.

Gnanaraj *et al.* [4] observed loop formation on the positive imaginary plane in the *low frequency* (mHz) range in his impedance measurements with *coin cells*. These results are, however, mistakenly addressed to SEI formation, more likely, the observation is related to *pitting corrosion* as proposed by Barsoukov [6] and experimentally

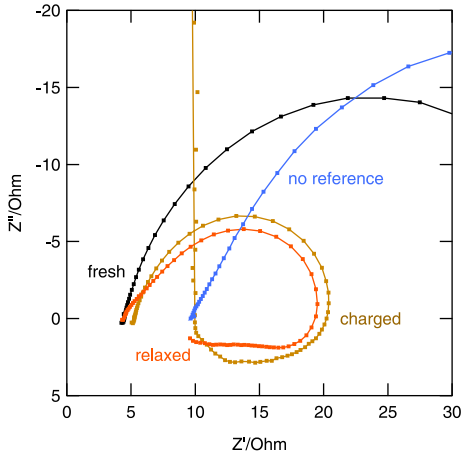

Fig. 5. Nyquist diagrams of an electrochemically still not fully stable lithium-ion half cell with a graphite anode. Pitting corrosion observed on the reference electrode manifests itself as a loop in the low-frequency regime of positive imaginary impedances. The lines are to guide the eye. See text for further discussion.

proven by Arrabal [22]. Furthermore, in both publications these low frequency loops are wrongly named as *inductive*. In our opinion they observed the so-called *negative capacitance effect*. The underlying theory for this phenomenon was established as early as 1986 by Jonscher [7]; it frequently emerges in semiconductors, corroding electrodes and batteries. In 1998, Ershov [25] formed the mathematical framework for the negative capacitance effect in semiconductor devices and in 2014 the same effect was experimentally proven for ferroelectric materials [26]. Elkin *et al.* addressed this effect to iron corrosion and provides a mathematical derivation [27]. For alternating currents with sine-shape, as they are used in impedance spectroscopy, the capacitive reactance X_C is given by

$$X_C = \frac{-j}{\omega C}, \tag{4}$$

with the electrical capacitance C and the angular frequency ω. The negative capacitance effect leads to an impedance measurement result X_C^- with an inverse phase behavior

$$X_C^- = \frac{j}{\omega C}. \tag{5}$$

The phase shift between voltage and current is the same as for the inductive reactance X_L

$$X_L = j\omega L, \tag{6}$$

with the electrical inductance L, but the frequency-dependance is contrariwise.

Because the effect of *non-equilibrium transient injection* [25] or unbalanced desorption and adsorption rates [27] can be considered as the the origins of the phase shift between voltage and current, we are no longer dealing with pure sine currents. The current response is *non-linear*, hence, higher harmonics emerge

in frequency domain. Although higher harmonic responses were studied at the very beginning of the development of impedance spectroscopy [28], they were largely forgotten until they have recently been 'rediscovered' in fuel cell research [29]. As classical impedance spectroscopy is defined only at linear working points [6], the impedance spectrometer filters out all higher harmonics and simplifies the current response to a single-frequency current signal. The phase shift between exciting voltage and current response is then interpreted as being capacitive or inductive in nature. If a positive phase shift emerges between a sine voltage and current, the impedance value will always be saved in the positive complex plane by the data recorder.

5. Summary and Conclusions

The present study was aimed at understanding the origin of inductive loop formation in complex plane data of lithium-ion batteries. For this purpose model-type lithium-ion half cells with anodes either using graphite or $Li_4Ti_5O_{12}$ were assembled taking advantage of different cell configurations. The impedance responses of two different electrochemical cells were studied: lithium-ion cells built in commercially available Swagelok T-fittings as well as in low-inductive electrochemical cells developed in-house. The cells were cycled extensively and impedance measurements were recorded. After cycling, the electrodes were investigated by scanning electron microscopy. From the data obtained conclusions were drawn about cell aging, solid electrolyte interphase (SEI) formation, and battery design issues.

We identified four different sources of inductive and negative capacitance loop formation: springs, reference electrodes, drift and corrosion. Inductive loop formation in the high-frequency and medium-frequency regime of impedance data in complex plane plots of Li-ion batteries has been explained to be caused by SEI formation for a long time. This explanation, however, lacks theoretical background: the experiments carried out in the present work together with the estimations of impedances presented clearly disprove the interrelationship between inductive loops and SEI formation.

Instead, the present findings show that inductances have their origin in experimental setup rather than in electrochemical phenomena. Wiring and cell design are highly influencing the impedance behavior. With the in-house developed cell container and an optimized Swagelok cell the inductive loop issue can easily be eliminated completely. The evolution of passivating layers on electrode surfaces because of electrochemical instabilities leads to capacity loss and an increase of the overall internal cell resistance. This finding supports the validity of traditional battery models taking into account the SEI formation as additional resistances that increases with cycle life.

Finally, in many cases the loops emerging in the low-frequency range are wrongly called inductive. In our opinion, they are caused by drift and corrosion and can be explained by the so-called *negative capacitance effect*.

Acknowledgement

Financial support by the Austrian Federal Ministry of Science, Research and Economy and the National Foundation for Research, Technology and Development is gratefully acknowledged. We thank the Deutsche Forschungsgemeinschaft for additional financial support in the frame of the Research Unit 1277 *molife* (grant no.: WI 3600 2-1).

References

[1] R.V. Noorden, Nature 507 (2014) 26.
[2] Q.-C. Zhuang, X.-Y. Qiu, S.-D. Xu, Y.-H. Qiang, S.-G. Sun, Diagnosis of Electrochemical Impedance Spectroscopy in Lithium-Ion Batteries, InTech, 2012.
[3] Q.C. Zhuang, T. Wei, G.Z. Wei, Acta Chim. Sinica 67 (2009) 2184–2192.
[4] J.S. Gnanaraj, R.W. Thompson, S.N. Iaconatti, J.F. Di Carlo, K.M. Abraham, Electrochem. Solid State Lett. 8 (2005) A128–A132.
[5] M. Faraday, Phil. Trans. Royal Soc. London: Experimental Researches in Electricity (1832) 154.
[6] E. Barsoukov, J.R. Macdonald, Impedance Spectroscopy Theory, Experiment, and Applications, John Wiley & Sons, Inc., Hoboken, New Jersey, 2005.
[7] A.K. Jonscher, J. Chem. Soc. Faraday Trans. 2 82 (1986) 75–81.
[8] H.-M. Cho, Y.J. Park, H.-C. Shina, J. Electrochem. Soc. 157 (2010) A8–A18.
[9] S. Klink, E. Madej, E. Ventosa, A. Lindner, W. Schuhmann, F.L. Mantia, Electrochem. Commun. 22 (2012) 120–123.
[10] U. Langklotz, S. Wennig, S. Dobrowolny, L. Wagner, Einfluss des Zelldesign auf die elektrochemische Impedanzspektroskopie (EIS), in: Symposium Elektrochemie, Dresden, 2014.
[11] Y.-B. He, M. Liu, Z.-D. Huang, B. Zhang, Y. Yu, B. Li, F. Kang, J.-K. Kim, J. Power Sources 239 (2013) 269–276.
[12] K. Colbow, J. Dahn, R. Haering, J. Power Sources 26 (1989) 397–402.
[13] E. Ferg, R.J. Gummow, A. de Kock, M.M. Thackeray, J. Electrochem. Soc. 141 (1994) L147–L149.
[14] T. Ohzuku, A. Ueda, N. Yamamoto, J. Electrochem. Soc. 142 (1995) 1431–1435.
[15] J. Haetge, P. Hartmann, K. Brezesinski, J. Janek, T. Brezesinski, Chem. Mater. 23 (2011) 4384–4393.
[16] G.-N. Zhu, Y.-G. Wang, Y.-Y. Xia, Energy Environ. Sci. 5 (2012) 6652–6667.
[17] T.-F. Yi, L.-J. Jiang, J. Shu, C.-B. Yue, R.-S. Zhu, H.-B. Qiao, J. Phys. Chem. Solids 71 (2010) 1236–1242.
[18] H. Xia, Z. Luo, J. Nanotechnol. Rev. 3 (2014) 161–175.
[19] S. Chen, Y. Xin, Y. Zhou, Y. Ma, H. Zhou, L. Qi, Energy Environ. Sci. 7 (2014) 1924–1930.
[20] R. Dedryvère, D. Foix, S. Franger, S. Patoux, L. Daniel, D. Gonbeau, J. Phys. Chem. C 114 (2010) 10999–11008.
[21] S.E. Li, B. Wang, H. Peng, X. Hu, J. Power Sources 258 (2014) 9–18.
[22] R. Arrabal, A. Pardo, M. Merino, M. Mohedano, P. Casajús, K. Paucar, G. Garcés, J. Corr. Sci. 55 (2012) 301–312.
[23] J. Vetter, P. Novák, M. Wagner, C. Veit, K. Möller, J. Besenhard, M. Winter, M. Wohlfahrt-Mehrens, C. Vogler, A. Hammouche, J. Power Sources 147 (2005) 269–281.
[24] Y. Dai, L. Cai, R. White, J. Electrochem. Soc. 160 (2013) A182–A190.
[25] M. Ershov, H.C. Liu, L. Li, M. Buchanan, Z.R. Wasilewski, A.K. Jonscher, IEEE Trans. Elec. Dev. (1998).
[26] A.I. Khan, K. Chatterjee, B. Wang, S. Drapcho, L. You, C. Serrao, S.R. Bakaul, R. Ramesh, S. Salahuddin, Nat. Mater. 14.
[27] V.V. Elkin, A.I. Marshakov, A.A. Rybkina, M.A. Maleeva, Russian J. Electrochem. 47 (2011) 136–146.
[28] A. Lasia, Electrochemical Impedance Spectroscopy and its Applications, Springer, 2014.
[29] E. Ramschak, N. Fouquet, H. Brandstätter, V. Hacker, J. Autom. Safety Ener. 2 (2011) 45–52.

5.3.2 Li-Ion Dynamics in Li-Ion Full Cells With Si as Negative Electrode

Introduction

The lithium-ion battery concept is a promising energy storage system, both for larger automotive systems and smaller mobile devices. The smallest of these, the *microbatteries*, are desirably based on the all-solid-state concept consisting of thin layers of electroactive materials separated by a solid-state electrolyte.[114] Recent advances in micro- and nano-electromechanical systems (MEMS/NEMS) technology have led to a niche industry of diverse small-scale devices that include microsensors, micromachines, drug delivery systems, etc. For these devices, there is an urgent need to develop *micro lithium-ion batteries* (MLIBS) with dimensions on the scale 1...10 mm^3 enabling on-board power delivery.[115]

Reducing the size of a common lithium-ion battery requires significant refinement of the traditional manufacturing method of building electrodes and also a careful evaluation of alternative electrolytes compared to conventionally employed liquid ones, to avoid leakage risks and other safety issues.[116] In this regard, both thin-film and thick film all-solid-state microbatteries have been in the focus of extensive exploration.[117]

Si-based negative-electrode materials could significantly increase the energy density of commercial lithium-ion batteries. Compared to conventional Li-ion battery materials, Si has the largest theoretical gravimetric capacity ($15Li + 4Si \rightarrow Li_{15}Si_4$; 3579 mAh/g),[118] a relatively low average voltage (the average delithiation voltage of Si is ≈ 0.4 V), and a large theoretical volumetric capacity (2200 mAh/cm^3). Unfortunately, Si-based electrodes typically suffer from poor capacity retention. In an attempt to overcome the limitations of Si, significant attention has been devoted to nano-engineering Si. A technical breakthrough was made by confining active Si at the nanoscale, which advantageously and effectively minimises the mechanical strains induced by the volume change of Si. [119–122] For example, Si nanowires directly grown on Cu substrates demonstrated promising behaviour as an anode material for lithium ion batteries.[119] In the nanowire form, the pulverisation of Si can be effectively avoided by providing facile strain relaxation during cycling.

The aim of this work is to investigate the performance of silicon microbatteries. Automotive and aerospace industry require an operating range between -50 to +50 °C. Not only should it be possible to charge the microcell within the whole temperature range; also the whole charge should be conserved after driving a heating and cooling cycle. Furthermore, the discharge voltage drop caused by the internal resistance should be as low as possible. The silicon microcells were developed in-house[123] as follows.

Experimental

The sophisticated production technology of Si-based semiconductor industry offers several routes to design the Si anode material. Using deep reactive-ion etching a boron-doped 8-inch silicon-wafer was surface-structured to yield towers with a square base area of 50 µm · 50 µm and a height of 32 µm; the distance between the towers was 17.5 µm (see Fig. 5.11). To provide

best possible electric contact to the printed circuit board, the backside of the silicon wafer was sputter-coated with a 1 µm thick copper layer.

The Si electrodes were prepared by deep reactive-ion etching using a highly boron-doped 8-inch silicon-wafer (monocrystalline, 200 µm in thickness, <100> orientation). The details of the anisotropic plasma etching of the wafer to yield laterally defined recess structures by means of an etching mask is described elsewhere [124]. The specific resistivity of the wafer-grade Si was 8 m$\Omega \cdot$ cm. The Si side of the electrodes was treated for 5 min with 5 % (v/v) hydrofluoric acid and rinsed with deionised water to increase the electrochemical activity of Si by removing any SiO_2 layers. To eliminate any effects of moisture, electrodes were dried following a two-step procedure: at first, they were dried at 60 °C for 12 h, then in a second they were dried in high vacuum ($< 10^{-4}$ mbar) for another 12 h.

Cycling combined with EIS was done with a Biologic potentiostat (VMP3) in a temperature range from -50 to +50 °C and within a frequency range from 1 Hz to 1 MHz. The applied electric voltage was a sine with 10 mV_{rms}. The cell temperature was controlled with a Julabo thermostat filled with silicone oil between -50 and +50 °C.

Results

The microcell was exposed to different ambient temperatures and impedance spectra were recorded as described in section 5.3.2. Starting at 20 °C, figure 5.12 shows the Nyquist diagrams at different states of charge. The fully charged microcell has the highest internal resistance which drops to its lowest value while discharging to 80 %, before it increases again at further discharge until 20 %.

The Bode diagrams at different temperatures are shown in figure 5.13. The absolute value of the battery's impedance $|Z|$ (apparent impedance) is plotted depending on the frequency. It shows typical high-pass behaviour with the first corner frequency at about 1 kHz.

The battery's conductivity increases with temperature. In Fig. 5.12 (50 °C) the Nyquist diagram at 50°C is shown, which is the upper end of the recorded temperature range. The diameter of both semicircles decreases which means an increase of anodic and cathodic conductivity.

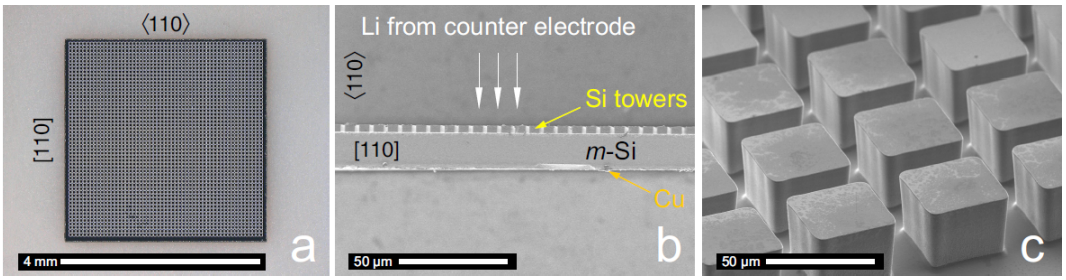

Figure 5.11: The micro-Si electrode. (a) top view (4 mm · 4 mm), (b) cross section and (c) the 3D patterned surface in detail [123], with permission.

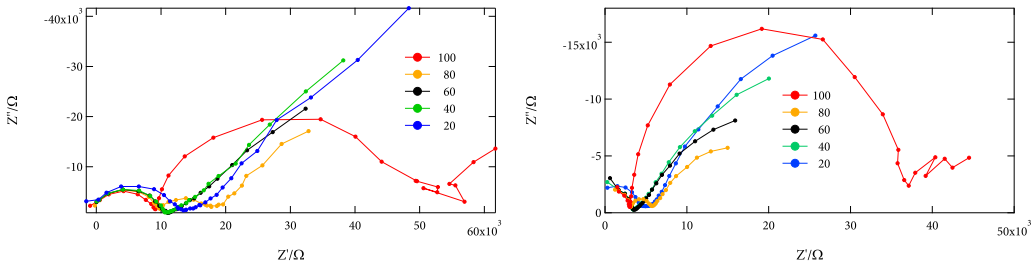

(a) -50 °C **(b)** -40 °C

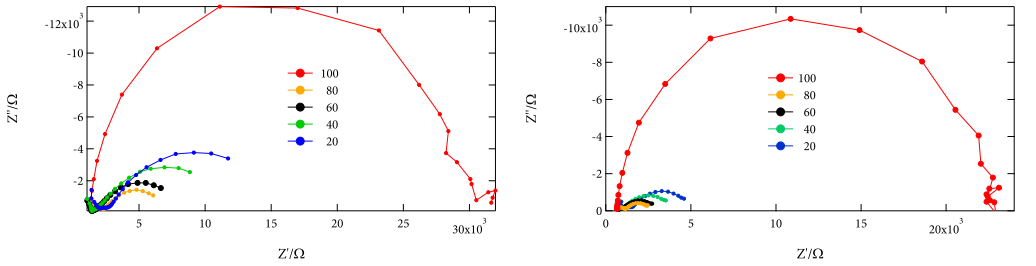

(c) -30 °C **(d)** -20 °C

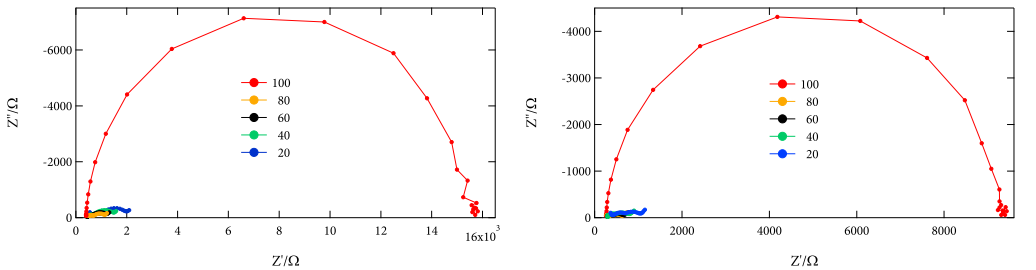

(e) -10 °C **(f)** 0 °C

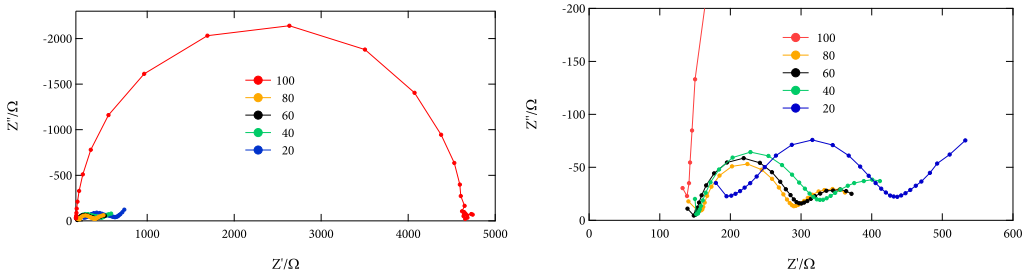

(g) 10 °C **(h)** 20 °C

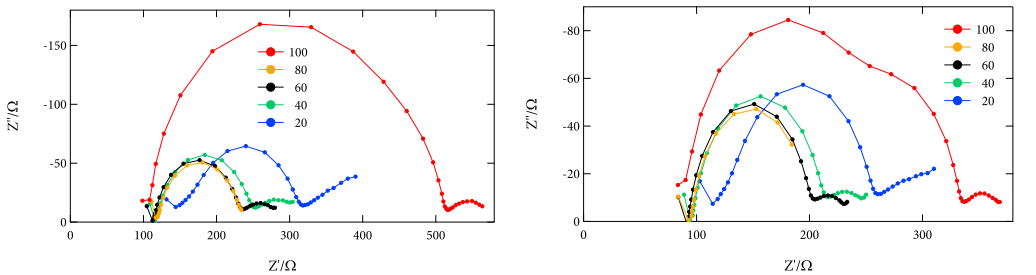

(i) 30 °C **(j)** 40 °C

Figure 5.12: Nyquist diagrams of impedance spectra recorded with microcell sorted by temperature, numbers indicating state of charge (SOC) in %.

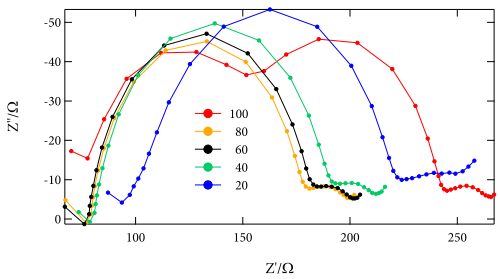

(k) 50 °C

Figure 5.12: Nyquist diagrams of impedance spectra recorded with microcell sorted by temperature (continued).

On the other hand, at temperatures below the freezing point of water, ionic conductivity almost vanishes, as can be seen in Fig. 5.12 (-50°C).

In Fig. 5.14 the Nyquist diagrams are sorted by state of charge (SOC).

Cell Ageing During Experiment

After taking impedance measurements at different ambient temperatures, another spectrum is recorded at the starting point of 20 °C. As can be seen in Fig. 5.15 (c), the battery's conductivity does not suffer from the experiments. No ageing effects are observed due to the heating and cooling cycle.

Also the cell's open circuit voltage fully recovers to its starting value after re-establishing the ambient temperature of 20 °C, as can be seen in Fig. 5.15 (a) and (b). The temperature dependence of the cell voltage is linear and fits the Nernst equation for full cells:

$$V_{\text{cell}} = V_{\text{cell}}^{\ominus} - \frac{RT}{zF} \ln Q_{\text{r}}\,, \tag{5.3}$$

where V_{cell} is the cell voltage at the temperature of interest, $V_{\text{cell}}^{\ominus}$ is the standard cell potential, R is the universal gas constant: $R = 8.314472(15)\ \text{J K}^{-1}\ \text{mol}^{-1}$, T is the thermodynamic temperature in K, F is the Faraday constant, the number of coulombs per mole of electrons: $F = 9.64853399(24) \cdot 10^4\ \text{C mol}^{-1}$, z is the number of moles of electrons transferred in the cell reaction, Q_{r} is the reaction quotient. Assuming Q_{r} to be constant, R/zF is the slope of the voltage-temperature-line in Fig. 5.15 (a) and (b). Inserting the known constants, the number of moles of electrons transferred in the cell reaction can be calculated.

DC-Behaviour

Impedance spectroscopy is not the method of choice to investigate a battery's DC-behaviour. To measure the microcell's internal resistance at 0 Hz it was connected to an ohmic resistor of

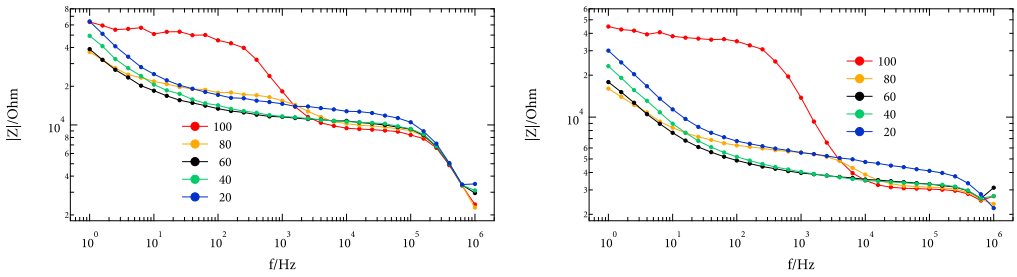

(a) -50 °C **(b)** -40 °C

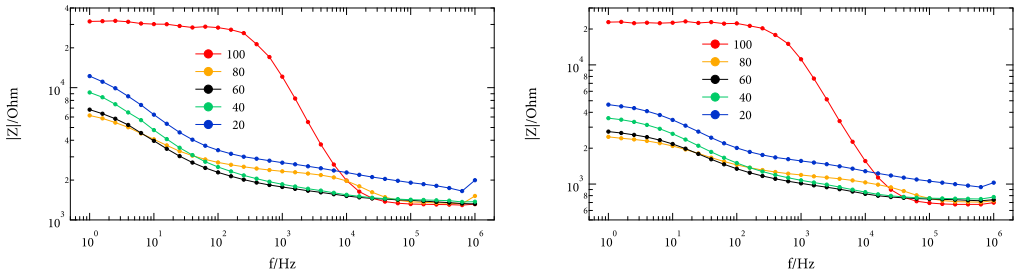

(c) -30 °C **(d)** -20 °C

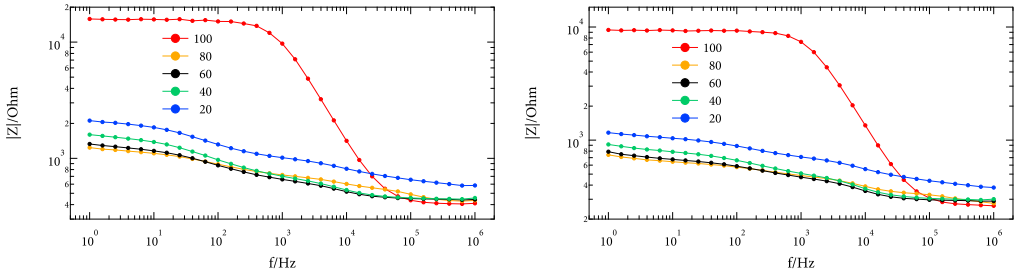

(e) -10 °C **(f)** 0 °C

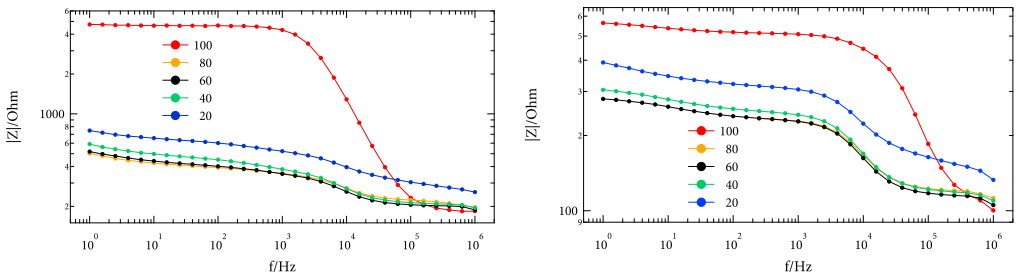

(g) 10 °C **(h)** 30 °C

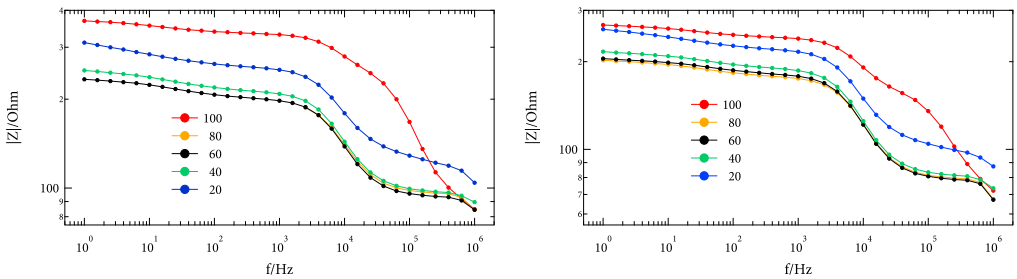

(i) 40 °C **(j)** 50 °C

Figure 5.13: Bode diagrams of impedance spectra recorded with microcell sorted by temperature, numbers indicating SOC in %.

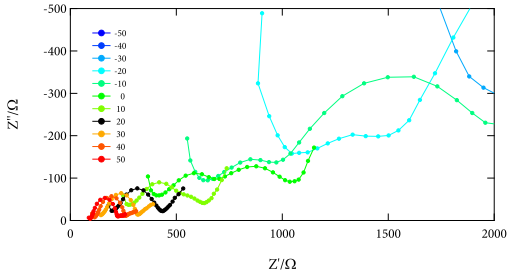

(a) 20 %

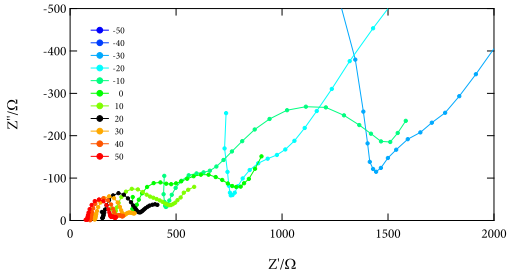

(b) 40 %

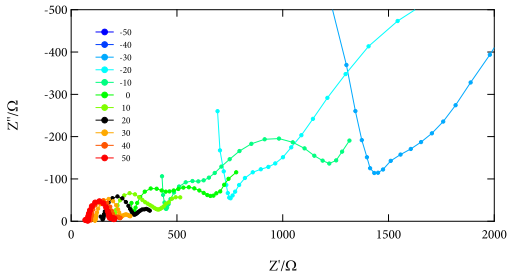

(c) 60 %

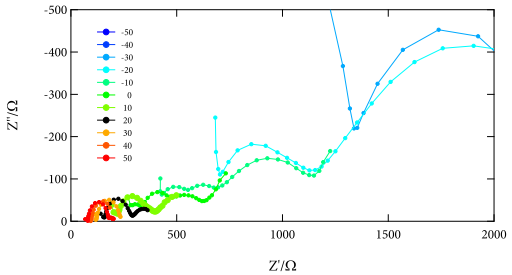

(d) 80 %

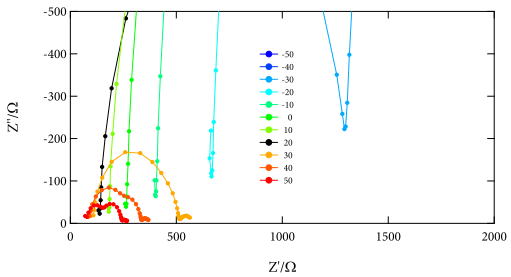

(e) 100 %

Figure 5.14: Nyquist diagrams of impedance spectra recorded with microcell sorted by state of charge, numbers indicating temperature in °C.

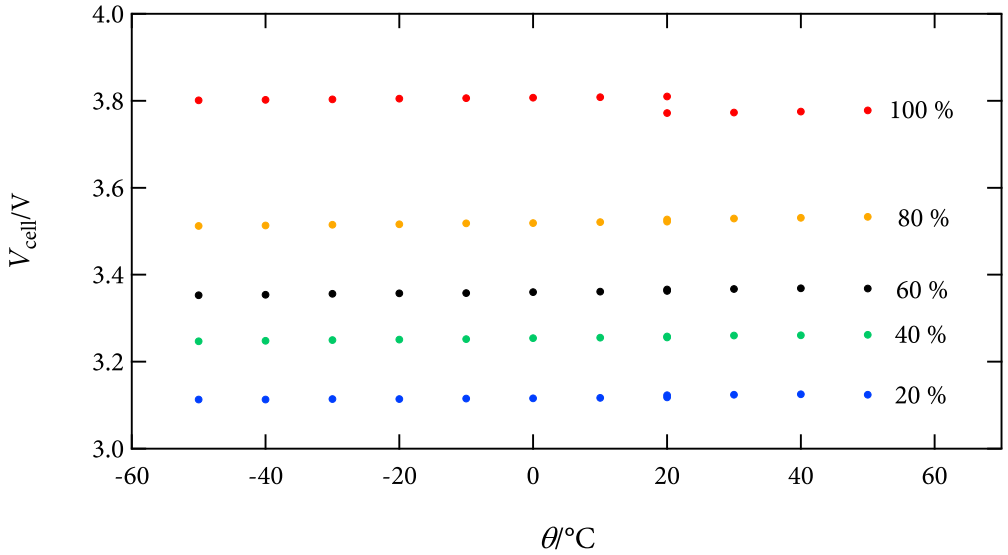

(a)

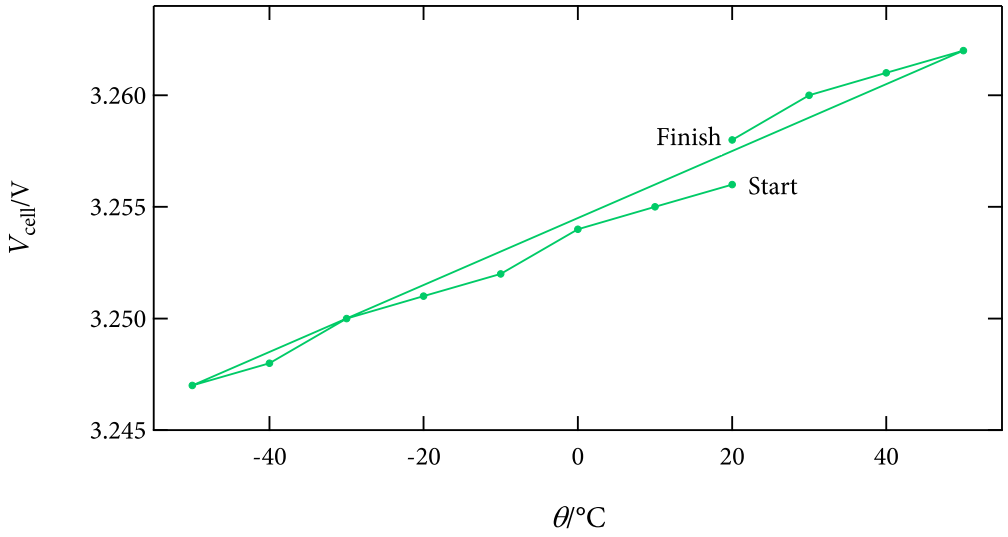

(b)

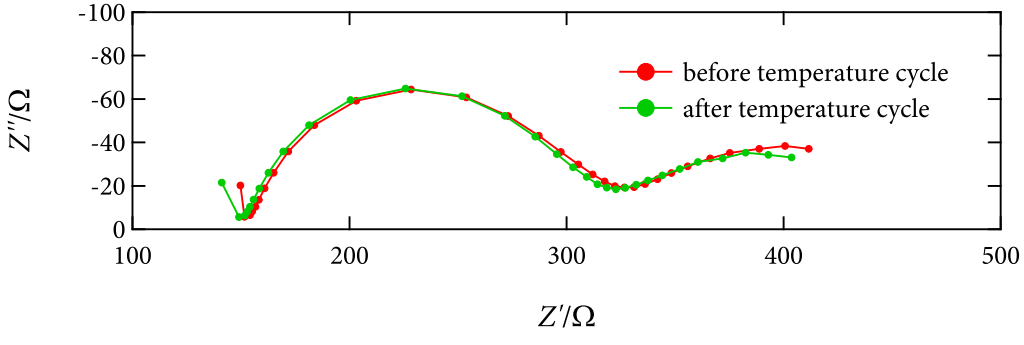

(c)

Figure 5.15: Cell voltage during temperature cycle at different states of charge (a), magnified for SOC = 40 % (b) and Nyquist plot of microcell at SOC = 40 % before and after temperature cycle (c).

50 Ω. The time dependence of the cell's voltage after closing the electric circuit is shown in Fig. 5.16. By Ohm's law, an internal resistance of about 5 kΩ can be estimated.

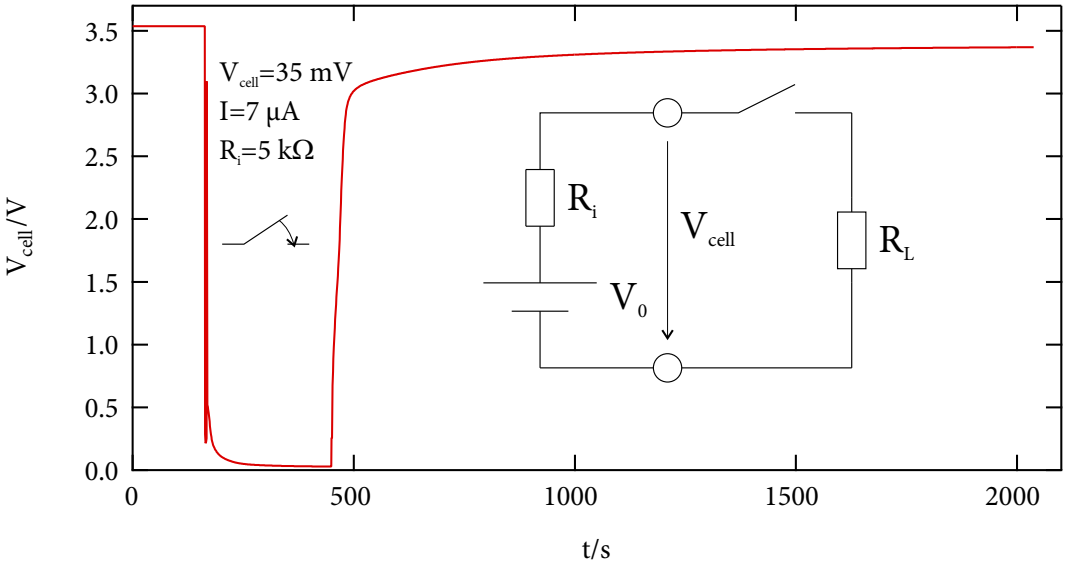

Figure 5.16: Battery voltage with respect to time while discharging over an electric load R_L of 50 Ω. The voltage drop down to about 30 mV is caused by an internal resistance R_i of about 5 kΩ.

Equivalent Circuit Model

With the impedance data from section 5.3.2 a small-signal equivalent circuit model can be built. A schematic containing 3 resistors and 2 capacitors is elected to enable easy system integration, see Fig. 5.17.

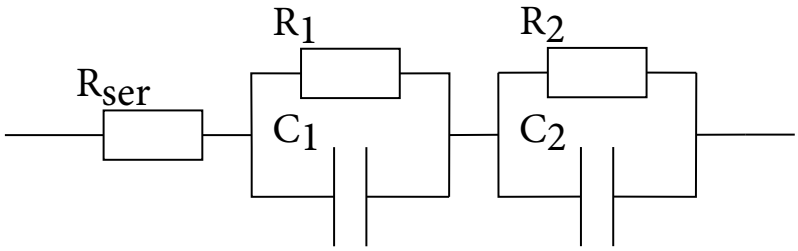

Figure 5.17: Schematic of the equivalent circuit model.

The model parameters are estimated by non-linear least squares fitting. The results for SOC = 80 % and θ = 20 °C can be seen in Tab. 5.1.

In Fig. 5.18 the model is compared to experimental results.

R_{ser}	=	158.711	Ω
R_1	=	126.591	Ω
C_1	=	184.204	nF
R_2	=	70.1744	Ω
C_2	=	294.333	µF

Table 5.1: Fitted parameters of the equivalent circuit model in Fig. 5.17 for a Si microbattery with an electrode surface area of 16 mm^2 at SOC = 80 % and θ = 20 °C.

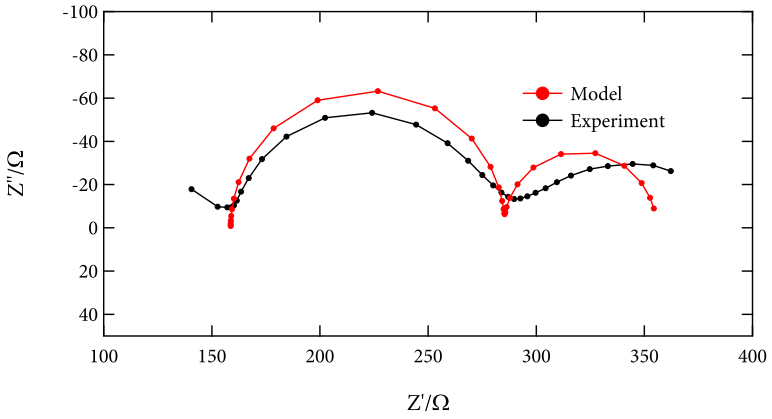

Figure 5.18: Nyquist diagram comparing experiment and model for SOC = 80 % and θ = 20 °C.

Discussion

The present findings show that the ionic conductivity in the investigated silicon microcell is strongly temperature-depending in the small-signal current range. The cell's internal resistance at temperatures below 0 °C is too high to enable charging and discharging. However, the cell does not suffer significantly from heating and cooling. The impedance measurement results show that the cell's properties are not altered by heating and cooling cycles. Furthermore, the open circuit voltage remains stable over the whole temperature range. This is an indicator against dendrite growth, damage by volume expansion and internal short circuits.

Summary and Outlook

Silicon based lithium-ion full cells were assembled in-house for on-chip use in industrial, automotive and aerospace applications. A sample cell was investigated by electrochemical impedance spectroscopy at different temperatures and states of charge. The results were plotted in the Nyquist and Bode representation. A simple equivalent circuit model for a silicon microcell was simulated as an example for system integration. The findings show that the ionic mobility is very restricted at low temperatures which leads to a very high internal

resistance of the microcell. The issue of internal cell damage due to volume expansion was eliminated completely.

Silicon based lithium-ion microcells show high energy density, high robustness with respect to temperature variations and easy integration in silicon based semiconductors. However, to fulfil automotive and aerospace requirements, the ionic mobility of silicon microcells has to be further increased. In the present state, charging and discharging is not possible at temperatures below 0 °C.

6 Conclusions and Outlook

The findings from the investigations on Ti-based lithium-oxides show that the ionic conductivity can be increased by ball-milling. After a short milling period of only 30 min a significant increase in conductivity was found as was detected by impedance spectroscopy. This was ascribed to the large fraction of defects introduced during mechanical treatment. At longer milling times amorphous phases were increasingly formed; furthermore, the oxide transformed into the α-modification which is a metastable form crystallising with NaCl structure. Comparisons with $Li_4Ti_5O_{12}$ show that the increase in conductivity is much less pronounced for LTO when treated in planetary mills. In the case of β-Li_2TiO_3 a significant amount of amorphous material was formed. In contrast when LTO is treated in shaker mills, phase-pure nanocrystalline lithium titanate is formed. The latter finding and its relationship to Li-ion dynamics are important for battery applications with (nanostructured) LTO anodes prepared *via* high-energy ball-milling. The so-prepared LTO anodes virtually do not form any SEI and remain stable for more than 1000 cycles in liquid-electrolyte based Li-ion batteries.

The investigations on S-based lithium phosphates show that phase-pure γ-Li_3PS_4 can by synthesised mechanically from originally micro-structured $3Li_2S : P_2S_5$. Compared to data from the literature, the prepared sample pertains the highest ionic conductivity ever observed among crystalline Li_3PS_4. Cyclic voltammetry shows that γ-Li_3PS_4 is sufficiently electrochemically stable to be applied in solid-state Li-ion batteries, although this is very likely due to passive films forming at the interface. A low activation energy E_a can be derived from the direct current conductivity σ_{dc}. The NMR experiments show fast local jump movements that do not necessarily cause a high σ_{dc} and a low E_a of the ion transport on longer time scales. A superposition of different diffusion processes is visible: a broad $T_{1\rho}$ peak with abnormal high temperature edge and at least two T1-processes with E_a = 0.09 eV and 0.2 eV.

The experiments made with Li-ion half cells identified four different sources of inductive and negative capacitance loop formation: springs, reference electrodes, drift and corrosion. Inductive loop formation in the high-frequency and medium-frequency regime of impedance data in complex plane plots of Li-ion batteries has been explained to be caused by SEI formation for a long time. This explanation, however, lacks theoretical background: the experiments carried out in the present work together with the estimations of impedances presented clearly disprove the interrelationship between inductive loops and SEI formation.

Instead, the present findings show that inductances have their origin in experimental set-up rather than in electrochemical phenomena. Wiring and cell design are highly influencing the impedance behaviour. With the in-house developed cell container and an optimised Swagelok

cell the inductive loop issue can easily be eliminated completely. The evolution of passivating layers on electrode surfaces because of electrochemical instabilities leads to capacity loss and an increase of the overall internal battery resistance. This finding supports the validity of traditional battery models taking into account the SEI formation as additional resistances that increases with cycle life.

Finally, in many cases the loops emerging in the low-frequency range are wrongly called inductive. In our opinion, they are caused by drift and corrosion and can be explained by the so-called *negative capacitance effect*.

Silicon based lithium-ion microcells show high energy density, high robustness against temperature variations and easy integration in silicon based semiconductors. However, to fulfil automotive and aerospace requirements, the ionic mobility of silicon microcells has to be further increased. In the present state, charging and discharging is not possible at temperatures below 0 °C.

7 Summary

The aim of the present work was to investigate solid electrolytes, liquid electrolytes and electrode materials for safe and high-performing batteries. The materials investigated were the solid ion conductors $Li_4Ti_5O_{12}$ and Li_3PS_4. Liquid electrolytes based on lithiumhexafluorophosphate ($LiPF_6$) were used with the solid intercalation materials mentioned, graphite and metal Si-electrodes. The results obtained in the course of this dissertation were presented cumulatively in the form of published (and peer-reviewed) papers and unpublished manuscripts.

In the first peer-reviewed paper, Ti-based oxides like Li_2TiO_3 and $Li_4Ti_5O_{12}$ were investigated with regard to their ionic conductivity. Ball milling proved to be a versatile tool to change the morphology of given materials, to induce phase transformations, and to prepare nano-crystalline ceramics. Here, work was focussed on poorly conducting β-Li_2TiO_3 to study the effect of mechanical treatment on overall conductivity. β-Li_2TiO_3 might emerge as a coating material for active materials.

In the first unpublished manuscript, phase-pure γ-Li_3PS_4 was synthesised mechanically through ball-milling followed by heat treatment. The so prepared powder samples were analysed *via* X-Ray crystallography and NMR techniques. The powders were cold-pressed into dense tablets. Au electrodes were applied by vaporisation in an inert gas atmosphere. The pellets were analysed *via* impedance spectroscopy and cyclic voltammetry. The conductivity spectra show that the mechanically synthesised γ-Li_3PS_4-sample pertains higher conductivity compared to the values known from the literature, but cannot keep up with amorphous material. The cyclic voltammogram shows that the electrolyte remains kinetically stable.

The second peer-reviewed paper was aimed at understanding the origin of inductive loop formation in complex plane data of lithium-ion batteries. For this purpose model-type lithium-ion half cells with anodes either using graphite or $Li_4Ti_5O_{12}$ were assembled taking advantage of different cell configurations. The impedance responses of two different electrochemical cells were studied: lithium-ion batteries built in commercially available Swagelok T-fittings as well as in low-inductive electrochemical cells developed in-house. The cells were cycled extensively and impedance measurements were recorded. After cycling, the electrodes were investigated *via* scanning electron microscopy. From the data obtained conclusions were drawn about cell ageing, solid electrolyte interphase (SEI) formation, and battery design issues.

For the second unpublished manuscript, silicon based lithium-ion full cells were assembled in-house for on-chip use in industrial, automotive and aerospace applications. A sample cell

was investigated *via* electrochemical impedance spectroscopy at different temperatures and states of charge. A simple equivalent circuit model for a silicon microcell was simulated as an example for system integration. The findings show that the ionic mobility is very restricted at low temperatures which leads to a very high internal resistance of the microcell. The issue of internal cell damage due to volume expansion was alleviated by microstructuration of the Si anode by lithographic methods.

A Experimental

A.1 Apparatus

For structural characterisation X-ray powder diffraction patterns were recorded on a Bruker D8 Advance diffractometer with Bragg Brentano geometry using Cu Kα radiation (10 to 100 $^{\circ}2\theta$, step size 0.02 $^{\circ}2\theta$, and step time 1 s), see Fig.A.1. Rietveld refinement was carried out with an X'Pert HighScore Plus software package (PANalytical).

Figure A.1: Bruker D8 Advance diffractometer with Bragg Brentano geometry.

^{6}Li magic angle spinning (MAS) NMR spectra were recorded with a single-pulse sequence using an Avance-500 NMR spectrometer (Bruker, 73.6 MHz resonance frequency for ^{6}Li) with field drift compensation at spinning speeds of up to 30 kHz (2.5-mm MAS probe, ambient bearing gas), see Fig. A.2. Spectra were recorded non-selectively using a short pulse with a length of ca. 2 µs. They were referenced to crystalline Li acetate serving as second reference; the chemical shifts presented refer to aqueous LiCl being the primary reference.

Figure A.2: Photograph of the solid-state NMR spectrometer workstation Bruker Avance III 500.

For our broadband impedance measurements the powders were cold-pressed into dense tablets by means of a 10 mm press set in combination with a P.O.-Weber hand press that allows a uni-axial force of 10 kN. Au electrodes of about 100 nm thickness were applied by vaporisation in an inert gas atmosphere. Temperature-variable 2-electrode impedance measurements were carried out with a Novocontrol Concept 80 broadband analyser (Alpha-AN, Novocontrol) that is used in combination with a BDS 1200 cell and an active ZGS cell interface, see Fig. A.3. The temperature in the sample chamber is automatically controlled with an accuracy of ± 0.01 K by a QUATRO cyrosystem (Novocontrol) using a constant flow of freshly evaporated

nitrogen gas that is heated up. The setup is able to record impedances and permittivities at frequencies ranging from few mHz up to 20 MHz (150 K to 570 K).

Figure A.3: Photograph of the impedance spectroscopy workstation Concept 80 (Novocontrol).

Cyclic voltammetry (CV) and EIS was done with a BioLogic potentiostat (VMP3) (see Fig. A.4) at room temperature within a frequency range from 1 mHz to 1 MHz. Au electrodes of about 100 nm thickness were applied by vaporisation in an inert gas atmosphere for symmetric and asymmetric CV and a Li metal electrode was applied mechanically for asymmetric CV only. The so prepared air sensitive pellets were packed in a specially designed air-tight, low-inductance electrochemical cell, made of an electrically insulating plastic without metallic springs and screws.

Figure A.4: Photograph of the potentiostate BioLogic VMP3.

A.2 Software

Listed below is the software used in the acquisition, processing and analysis of data presented in this work.

TopSpin 3.1 (Bruker BioSpin GmbH): Execution of NMR experiments on the Avance III spectrometers; calculation and phase correction of NMR spectra using the built-in Fourier transformation routine.

Dmfit Program:[125,126] Conversion of the native Bruker file format into ASCII files.

WSolids1:[127] Simulation of quadrupolar solid-state NMR spectra.

WinDETA 5.73 (NOVOCONTROL Technologies GmbH & Co. KG): Execution of all impedance spectroscopy experiments on the Concept 80 system and export of data.

EC-Lab 10.40: Controlling the potentiostat BioLogic VMP3

X'Pert HighScore Plus 3.0.0 (PANalytical): Rietveld refinement

IGOR Pro 6.3.2.3: Processing, analysis, and presentation of all data acquired.

CorelDRAW X7: Graphical post-processing of figures meant for publication.

MEISP 3.0 (Korea Kumho Petrochemical Co., Ltd. (KUMHO)): Multiple Electrochemical Impedance Spectra Parametrisation

TeX Live 2015: TEX typesetting distribution.

B List of Publications

B.1 Journal Articles

Myth and Reality about the Origin of Inductive Loops in Impedance Spectra of Lithium-Ion Electrodes — A Critical Experimental Approach
Brandstätter H., Hanzu I., and Wilkening M. *Electrochimica acta* **207**, 218–223 (2016).

Li ion dynamics in nanocrystalline and structurally disordered Li2TiO3
Brandstätter H., Wohlmuth D., Bottke P., Pregartner V., and Wilkening M. *Zeitschrift für physikalische Chemie* **229**, 1363–1374 (2015).

B.2 Poster Presentations

Sulfide Electrolytes: Study of Local Li-Ion Dynamics in Li3PS4 using 7Li NMR Relaxometry
Prutsch D., Brandstätter H., Pregartner V., Wohlmuth D., Epp V., and Wilkening M. — *18th International Meeting on Lithium Batteries*, Chicago (USA), June 19th–24th, 2016.

Li ion dynamics in nanocrystalline and structurally disordered Li2TiO3
Brandstätter H., Wohlmuth D., Bottke P., Pregartner V., and Wilkening M. — *8th International Conference on Advanced Lithium Batteries for Automobile Applications*, Bilbao (ES), September 30th–October 02nd, 2015.

Li ion dynamics in nanocrystalline and structurally disordered Li2TiO3
Brandstätter H., Wohlmuth D., Bottke P., Pregartner V., and Wilkening M. — *15th European Conference On Solid State Chemistry*, Vienna (AT), August 24th–26th, 2015.

Bibliography

[1] Sapunkov, O., Pande, V., Khetan, A., Choomwattana, C., and Viswanathan, V. *Translational Materials Research* **2**, 045002 (2015).

[2] Scrosati, B., Garche, J., and Tillmetz, W. *Advances in Battery Technologies for Electric Vehicles*. Elsevier Science & Technology, UK (2015).

[3] Noorden, R. V. *Nature* **507**, 26 (2014).

[4] Doughty, D. and Roth, E. P. *Interface* **21**, 37–44 (2012).

[5] Roth, E. P. and Orendorff, C. J. *Interface* **21**, 45–50 (2012).

[6] Golubkov, A. W., Fuchs, D., Wagner, J., Wiltsche, H., Stangl, C., Fauler, G., Voitic, G., Thaler, A., and Hacker, V. *RSC Adv.* **4**, 3633–3642 (2014).

[7] Ferg, E., Gummow, R. J., de Kock, A., and Thackeray, M. M. *J. Electrochem. Soc.* **141**, L147–L149 (1994).

[8] Deschanvres, A., Raveau, B., and Sekkal, Z. *Mater. Res. Bull.* **6**, 699 (1971).

[9] Ronci, F., Reale, P., Scrosati, B., Panero, P., Albertini, V. R., Perfetti, P., di Michiel, M., and Merino, J. M. *J. Phys. Chem. B* **106**, 3082 (2002).

[10] Tarascon, J. and Armand, M. *Nature* **414**, 359 (2001).

[11] Hayashi, A., Hama, S., Mizuno, F., Tadanaga, K., Minami, T., and Tatsumisago, M. *Solid State Ionics* **175**, 683 (2004).

[12] Hashimoto, Y., Machida, N., and Shigematsu, T. *Solid State Ionics* **175**, 177 (2004).

[13] Maier, J. *Nat. Mater.* **4**, 805–815 (2005).

[14] Heitjans, P., Indris, S., and Wilkening, M. In *Nanocomposites,* Knauth, P. and Schoonman, J., editors, volume 10 of *Electronic Materials: Science and Technology*, 227–246. Springer, New York (2007).

[15] Wilkening, M., Epp, V., Feldhoff, A., and Heitjans, P. *J. Phys. Chem. C* **112**, 9291–9300 (2008).

[16] Heitjans, P. and Wilkening, M. *MRS Bull.* **34**, 915–922 (2009).

[17] Farrington, G. C. and Briant, J. L. *Science* **204**, 1371–1379 (1979).

[18] Brinkmann, D., Mali, M., Roos, J., Messer, R., and Birli, H. *Phys. Rev. B* **26**, 4810–4825 (1982).

[19] Bader, B., Heitjans, P., Stockmann, H. J., Ackermann, H., Buttler, W., Freilander, P., Kiese, G., van der Marel, C., and Schirmer, A. *J. Phys.: Condens. Matter* **4**, 4779–4800 (1992).

[20] Julien, C. and Nazri, G. A. *Solid State Ionics* **68**, 111–116 (1994).

[21] Van der Ven, A., Ceder, G., Asta, M., and Tepesch, P. D. *Phys. Rev. B* **64**, 184307 (2001).

[22] Wilkening, M. and Heitjans, P. *Phys. Rev. B* **77**, 24311 (2008).

[23] Brezesinski, T., Wang, J., Tolbert, S. H., and Dunn, B. *Nat. Mater.* **9**, 146–151 (2010).

[24] Barsoukov, E. and Macdonald, J. R. *Impedance Spectroscopy Theory, Experiment, and Applications*. John Wiley & Sons, Inc., Hoboken, New Jersey (2005).

[25] Spieß, L., Teichert, G., Schwarzer, R., Behnken, H., and Genzel, C. *Moderne Röntgenbeugung*. Vieweg+Teubner, Wiesbaden (2009).

[26] Tobias, C. W., Eisenberg, M., and Wilke, C. R. *Electrochemistry of Ionic Chrystals* **99**, 359–365 (1952).

[27] Linden, D. and Reddy, T. B. *Handbook of Batteries*. McGraw-Hill, USA (2002).

[28] Suthersan, S. S. *Remediation engineering: design concepts*. CRC Press, USA (1996).

[29] Nernst, W. *Z. Phys. Chem.* **2**, 613–637 (1888).

[30] Nernst, W. *Z. Phys. Chem.* **4**, 129–181 (1889).

[31] Planck, M. *Ann. Phys. Chem.* **39**, 161 (1890).

[32] Fick, A. *Ann. Phys.* **170**, 59–86 (1855).

[33] Nyman, A. *An Experimental and Theoretical Study of the Mass Transport in Lithium-Ion Battery Electrolytes*. Dissertation, Kungliga Tekniska Högskolan (2011).

[34] Rehfeldt, S. and Stichlmair, J. **256**, 99–104 (2007).

[35] Maxwell, J. C. *The Scientific Papers of J. C. Maxwell* **2**, 26–78 (1965).

[36] Stefan, J. *Sitzungsberichte der Kaiserlichen Akademie der Wissenschaften Wien, 2te Abteilung a* **63**, 63–124 (1871).

[37] Bird, R., Stewart, W., and Lightfoot, E. *Transport Phenomena (2 ed.)*. Wiley, USA (2007).

[38] Mehrer, H. *Diffusion in Solids: Fundamentals, Methods, Materials, Diffusion-Controlled Processes*. Springer, Berlin, New York (2007).

[39] Murch, G. E. In *Phase Transformations in Materials,* Kostorz, G., editor, 171–238. Wiley-VCH Verlag GmbH, Weinheim (2001).

[40] Crank, J. *The Mathematics of Diffusion*. Clarendon Press, Oxford (1975).

[41] Greeuw, G. and Hoenders, B. J. *Appl. Phys.* **55**, 3371 (1984).

[42] Einstein, A. *Ann. Phys. (Ser. 4)* **19**, 371 (1905).

[43] Smart, L. and Moore, E. *Solid State Chemistry*. Chapman and Hall, London (1992).

[44] Schmalzried, H. *Chemical Kinetics of Solids*. VCH, Weinheim, New York, Basel, Cambridge, Tokyo (1995).

[45] Kleber, W., Bautsch, H.-J., Bohm, J., and Klimm, D. *Einführung in die Kristallographie*. Oldenbourg Wissenschaftsverlag GmbH, München, 19th edition (2010).

[46] Wert, C. *Phys. Rev.* **79**, 601 (1950).

[47] Vineyard, G. *J. Phys. Chem. Sol.* **3**, 121 (1957).

[48] van't Hoff, J. H. *Études de dynamique chimique*. Frederik Muller & Co., Amsterdam (1884).

[49] Arrhenius, S. *Z. Phys. Chem.* **4**, 226–248 (1889).

[50] Nowick, A. and Burton, J. *Diffusion in Solids - Recent Developments*. Academic Press, Inc., USA (1975).

[51] Flynn, C. and Stoneham, A. *Phys. Rev.* **B1**, 3966 (1970).

[52] Ohm, G. S. *Annalen der Physik und Chemie* **80**, 79–88 (1825).

[53] Faraday, M. *Phil. Trans. Royal Soc. London: Experimental Researches in Electricity* , 154 (1832).

[54] Fourier, J. B. J. *Théorie analytique de la chaleur*. Chez Firmin Didot, pére et fils, Paris (1822).

[55] Paul, R. *Elektrotechnik*. Springer, Berlin (1985).

[56] Qian, X., Gu, N., Cheng, Z., Yang, X., Wang, E., and Dong, S. *Materials Chemistry and Physics* **74**, 98–103 (2002).

[57] Randles, J. E. B. *Disc. Faraday Soc.* **1**, 11–19 (1947).

[58] Aurbach, D., Markovsky, B., Rodkin, E., Levi, Y. S., Cohen, H.-J., Kim, D. H., , and Schmidt, M. *Electrochim. Acta* **47**, 4291–4306 (2002).

[59] Thevenin, J. *Journal of Power Sources* **14**, 45–52 (1985).

[60] Uchida, I., Ishikawa, H., Mohamedi, M., and Umeda, M. *Journal of Power Sources* **119–121**, 821–825 (2003).

[61] de Levie, R. *Electrochim. Acta* **8**, 751 (1963).

[62] Yoon, C., Barsukov, Y., and Kim, J. H. *Method of and Apparatus for Measuring Battery Capacity by Impedance Spectrum Analysis*. (2001). US Patent 6,208,147.

[63] Funke, K., Cramer, C., and Wilmer, D. In *Diffusion in Condensed Matter,* Heitjans, P. and Kärger, J., editors, 857–893. Springer, Berlin (2005).

[64] Kimball, J. C. and Adams, L. W. *Phys. Rev. B* **18**, 5851–5858 (1978).

[65] Jonscher, A. K. *Nature* **267**, 673–679 (1977).

[66] Lee, W. K., Liu, J. F., and Nowick, A. S. *Phys. Rev. Lett.* **67**, 1559–1561 (1991).

[67] Lim, B. S., Vaysleyb, A. V., and Nowick, A. S. *Appl. Phys. A* **56**, 8–14 (1993).

[68] Sidebottom, D. L., Green, P. F., and Brow, R. K. *Phys. Rev. Lett.* **74**, 5068–5071 (1995).

[69] Nowick, A. S., Vaysleyb, A. V., and Kuskovsky, I. *Phys. Rev. B* **58**, 8398–8406 (1998).

[70] Nowick, A. S., Vaysleyb, A. V., and Liu, W. *Solid State Ionics* **105**, 121–128 (1998).

[71] Rizos, A. K., Alifragis, J., Ngai, K. L., and Heitjans, P. *J. Chem. Phys.* **114**, 931–934 (2001).

[72] Kanert, O., Küchler, R., Soares, P. C., and Jain, H. *J. Non-Cryst. Solids* **307**, 1031–1038 (2002).

[73] Funke, K., Banhatti, R. D., Laughman, D., Badr, L., Mutke, M., Šantić, A., Wrobel, W., Fellberg, E. M., and Biermann, C. *Z. Phys. Chem.* **224**, 1891–1950 (2010).

[74] Ngai, K. L., Capaccioli, S., Shinyashiki, N., and Thayyil, M. S. *J. Non-Cryst. Solids* **356**, 535–541 (2010).

[75] Ruprecht, B. *Langsamer Li-Transport in Lithiumübergangsmetalloxiden untersucht mit NMR- und impedanzspektroskopischen Methoden*. Dissertation, Leibniz Universität Hannover (2012).

[76] Strom, U., Hendrickson, J. R., Wagner, R. J., and Taylor, P. C. *Solid State Commun.* **15**, 1871–1875 (1974).

[77] Röntgen, W. C. *Sonderabbdruck aus den Sitzungsberichten der Würzburger Physik.-medic. Gesellschaft* (1895).

[78] Dendy, P. P. and Heaton, B. *Physics for Diagnostic Radiology*. CRC Press, USA (1999).

[79] Feynman, R., Leighton, R., and Sands, M. *The Feynman Lectures on Physics, Vol.1*. Addison-Wesley, USA (1963).

[80] L'Annunziata, M. and Abrade, M. *Handbook of Radioactivity Analysis*. Academic Press, USA (2003).

[81] Grupen, C., Cowan, G., Eidelman, S. D., and Stroh, T. *Astroparticle Physics*. Springer, Berlin (2005).

[82] Bushberg, J. T., Seibert, J. A., Leidholdt, E. M., and Boone, J. M. *The essential physics of medical imaging*. Lippincott Williams & Wilkins, USA (2002).

[83] Compton, A. H. *Physical Review* **21**, 483–502 (1923).

[84] Marshall, A. G. *Biophysical Chemistry: Principles, Techniques, and Applications*. John Wiley & Sons, Inc., USA (1978).

[85] Strutt, J. *Philosophical Magazine* **41**, 107–120, 274–279 (1871).

[86] Thomson, J. J. *Conduction of Electricity through Gases*. Cambridge Univ. Press, UK (1906).

[87] Bragg, W. and Bragg, W. *Proc R. Soc. Lond. A* **88**, 428–438 (1913).

[88] Lifshin, E. *X-Ray Characterization of Materials*. Wiley, USA (1999).

[89] Heisenberg, W. *Zeitschrift für Physik* **43**, 172–198 (1927).

[90] Kennard, E. H. *Zeitschrift für Physik* **44**, 326 (1927).

[91] Weyl, H. *Gruppentheorie und Quantenmechanik*. Hirzel, Leipzig (1928).

[92] Feynman, R. *QED the Strange Theory of Light and matter*. Penguin, USA (1990).

[93] Singh, A. *Advanced X-ray Techniques in Research And Industries*. Ios Pr Inc (2005).

[94] Kamaya, N., Homma, K., Yamakawa, Y., Hirayama, M., Kanno, R., Yonemura, M., Kamiyama, T., Kato, Y., Hama, S., Kawamoto, K., and Mitsui, A. *Nature Materials* **10**, 682–686 (2011).

[95] Tachez, M., Malugani, J.-P., Mercier, R., and Robert, G. *Solid State Ionics* **14**, 181 (1984).

[96] Mercier, R., Malugani, J.-P., Fahys, B., Robert, G., and Douglade, J. *Acta Cryst.* **B38**, 1887–1890 (1982).

[97] Mercier, R., Malugani, J.-P., Fahys, B., Douglade, J., and Robert, G. *J. Solid State Chem.* **43**, 151 (1982).

[98] Brice, J. and Seances, C. R. *Acad. Sci., Ser. C.* **283**, 581 (1974).

[99] Liu, Z., Fu, W., Payzant, E. A., Yu, X., Wu, Z., Dudney, N. J., Kiggans, J., Hong, K., Rondinone, A. J., and Liang, C. *Journal of the American Chemical Society* **135**, 975–978 (2013).

[100] Hayashi, A., Noi, K., Sakuda, A., and Tatsumisago, M. *Nat. Commun.* **3**, 856 (2012).

[101] Tatsumisago, M., Nagao, M., and Hayashi, A. *Journal of Asian Ceramic Societies* **1**, 17–25 (2013).

[102] Murayama, M., Sonoyama, N., Yamada, A., and Kanno, R. *Solid State Ionics* **170**, 173–180 (2004).

[103] Homma, K., Yonemura, M., Kobayashi, T., Nagao, M., Hirayama, M., and Kanno, R. *Solid State Ionics* **182**, 53–58 (2011).

[104] Gobet, M., Greenbaum, S., Sahu, G., and Liang, C. *Chemistry of Materials* **26**, 3558–3564 (2014).

[105] Hayashi, A., Hama, S., Minami, T., and Tatsumisago, M. *Electrochemistry Communications* **5**, 111–114 (2003).

[106] Kim, J., Yoon, Y., Lee, J., and Shin, D. *Journal of Power Sources* **196**, 6920–6923 (2011).

[107] Seino, Y., Ota, T., Takada, K., Hayashi, A., and Tatsumisago, M. *Energy Environ. Sci.* **7**, 627 (2014).

[108] Kubel, F., Bertheville, B., and Bill, H. *Zeitschrift fuer Kristallographie - New Crystal Structures* **214**, 302–302 (1999).

[109] Wilkening, M., Epp, V., Feldhoff, A., and Heitjans, P. *J. Phys. Chem. C* **112**, 9291 (2008).

[110] Heitjans, P., Masoud, M., Feldhoff, A., and Wilkening, M. *Faraday Discuss.* **134**, 67 (2007).

[111] Rahn, J., Hüger, E., Dörrer, L., Ruprecht, B., Heitjans, P., and Schmidt, H. *Defect Diffus. Forum* **323**, 76–74 (2012).

[112] Rahn, J., Hüger, E., Dörrer, L., Ruprecht, B., Heitjans, P., and Schmidt, H. *Z. Physiol. Chem.* **226**, 439 (2012).

[113] Wilkening, M., Bork, D., Indris, S., and Heitjans, P. *Phys. Chem. Chem. Phys.* **4**, 3246 (2002).

[114] Nilsen, O., Miikkulainen, V., Gandrud, K. B., Østreng, E., Ruud, A., and Fjellvåg, H. *Phys. Status Solidi A* **211**, 357–367 (2014).

[115] Ferrari, S., Loveridge, M., Beattie, S. D., Jahn, M., Dashwood, R. J., and Bhagat, R. *Journal of Power Sources* **286**, 25–46 (2015).

[116] Oudenhoven, J., Baggetto, L., and Notten, P. *Adv. Energy Mater.* **1**, 10 (2011).

[117] Ho, C., Evans, J., and Wright, P. *Energy Harvesting of Autonomous Systems*. Artech House, USA (2010).

[118] Obrovac, M. N. and Christensen, L. *Electrochem. Solid-State Lett.* **7**, A93 (2004).

[119] Chan, C. K., Peng, H., Liu, G., McIlwrath, K., Zhang, X. F., Huggins, R. A., and Cui, Y. *Nat. Nanotechnol.* **3**, 31–35 (2008).

[120] Magasinski, A., Dixon, P., Hertzberg, B., Kvit, A., Ayala, J., and Yushin, G. *Nat. Mater.* **9**, 353–358 (2010).

[121] Liu, X. H., Zhong, L., Huang, S., Mao, S. X., Zhu, T., , and Huang, J. Y. *ACS Nano* **6**, 1522–1531 (2012).

[122] Wu, H., Chan, G., Choi, J. W., Ryu, I., Yao, Y., McDowell, M. T., Lee, S. W., Jackson, A., Yang, Y., Hu, L., and Cui, Y. *Nat. Nanotechnol.* **7**, 310–315 (2012).

[123] Sternad, M., Forster, M., and Wilkening, M. under review, (2016).

[124] Laermer, F. and Schilp, A. *Method of Anisotropically Etching Silicon*. (1996). US Patent 5,501,893.

[125] Massiot, D., Fayon, F., Capron, M., King, I., Le Calvé, S., Alonso, B., Durand, J.-O., Bujoli, B., Gan, Z., and Hoatson, G. *Magn. Reson. Chem.* **40**, 70–76 (2002).

[126] Massiot, D. *Dmfit Program*. NMR Spectrum Fitting Software, ver. 20090330, CRMHT - CNRS (2009) ☛ http://nmr.cemhti.cnrs-orleans.fr/Dmfit/Default.aspx.

[127] Eichele, K. *WSolids1*. Solid-State NMR Spectrum Simulation, ver. 1.19.11, Universität Tübingen (2009) ☛ http://anorganik.uni-tuebingen.de/klaus/soft/index.php?p=wsolids1/wsolids1.

Acknowledgements

My warmest thanks go to my adviser, Martin Wilkening, for giving me the unique chance of joining his team, for encouraging self-reliant research and for allowing me to present my results abroad. Not only am I thankful for his support and supervision in my scientific endeavours but also for his friendly attitude, encouraging words and patience when they were needed.

I also thank Otto Glatter for his kind willingness to assume the role of the second reviewer of the present work.

I am grateful to my co-adviser, Ilie Hanzu, for encouraging me in my scientific enterprises and in expanding my scope of research with his knowledge in electrochemistry. Without his patience, tenacity and vision many achievements would not have been possible.

Many thanks go to my colleagues – present and former. During the last three years I learned something new from them almost every day:

Veronika Pregartner taught me how to work in a chemical laboratory (it is not obvious for a physicist), how to use the glove-box, the ball-mill and how to metallise samples by sputtering, Marlena Uitz supervised me in assembling Swagelok cells, Walter Schmidt introduced me in the field of electrode preparation and programming the potentiostat, Denise Prutsch taught me how to assemble pouch cells; I would also like to thank her for proof-reading my manuscript, Dominik Wohlmuth and Viktor Epp showed me how to use the impedance analyser, Andreas Dunst introduced me in interpreting solid state impedance data, Lukas Schafzahl taught me how to metallise samples by vaporisation (not without sacrifices), Florian Preishuber-Pflügl supervised me in correctly cleaning the ball-mill beakers.

Furthermore, I would like to thank Tobias Müller for cooking delicious dishes for the whole work-group and joining me in forklift driving and programming in FORTRAN 77.

Finally, I would like to thank our mechanic, Johann Schlegl. Without his knowledge and skills there would be no experimental research at our institute.

Not only did all of the colleagues mentioned, and those who I might have forgotten to mention, provide many fruitful discussions and helpful points, they were also responsible for a very relaxed working atmosphere and generally good times. I consider myself very lucky to have met every single one of them. Thank you.